and during the discharging mode, it can be given as

$$E_C^{ref-d}(t) = k_p \int_{k\delta}^{t} sat_2(P)d\xi + E_{ck} \tag{36}$$

with $E_C^{ref-c}(t)$, $E_C^{ref-d}(t)$ and $0 < k_p < 1$ as the charge reference, discharge reference, and a constant representing the lost energy during transformation, respectively. sat_1 represent a saturation function in the range of $(-\infty, 0)$ and sat_2 the same function in the range of $(0, \infty)$. The energy reference for the supercapacitor is estimated as the sum result of both references.

$$E_C^{ref} = E_C^{ref-c} + E_C^{ref-d} \tag{37}$$

Then, the buck–boost voltage reference can be obtained using the last supercapacitor energy equation resolved for the voltage

$$V_{cr} = \sqrt{\frac{2E_C}{C}} \tag{38}$$

where V_{cr} is the reference voltage in the supercapacitor, E_c is the energy stored, and C is the capacitance.

To track the buck–boost voltage, the NIOC scheme was applied. Using (27), the voltage error at $k+1$, evc_{k+1} was calculated as follows

$$\begin{aligned} e_{Vcr,k+1} &= \omega_{1,1}(k)S(x_1) + \omega_{1,2}(k)S(x_2) \\ &+ w_{1,3}S(x_1)S(x_2) + \varpi_1 x_2 - V_{cr} \end{aligned} \tag{39}$$

Then, the NIOC was applied to determine the buck–boost current reference for the supercapacitor as follows

$$i_{cr} = \frac{1}{2}\left(R + \frac{1}{2}B(x_{1,k})^T PB(x_{1,k})\right)^{-1} B(x_{1,k})^T Pe_{Vcr,k+1} \tag{40}$$

The control scheme for the regenerative braking system using NIOC and the current reference generator is illustrated in Figure 17.

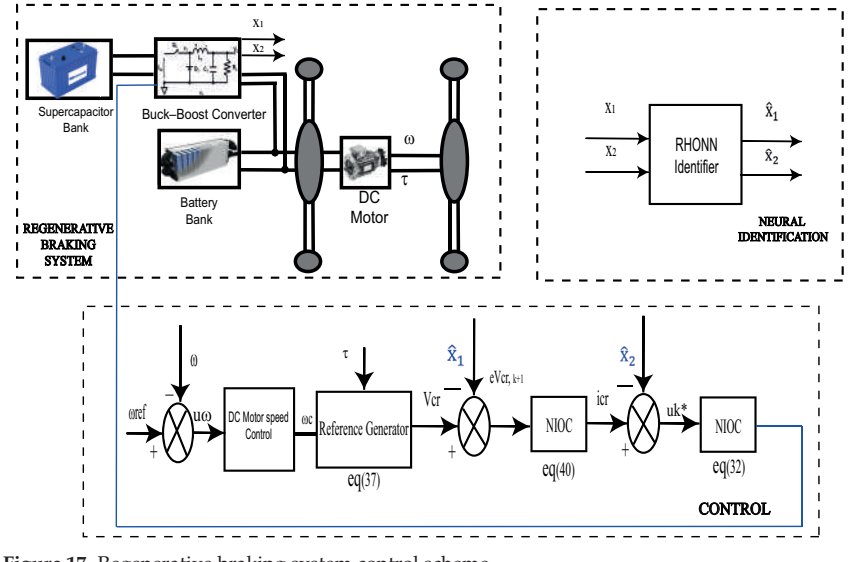

Figure 17. Regenerative braking system control scheme.

The DC motor speed was controlled using a PI controller to track a desired reference

$$u_{\omega} = k_{\omega_l p}(\omega_{l,ref} - \omega_l) + k_{\omega_l i}\int_0^t (\omega_{l,ref} - \omega_l) \tag{41}$$

where $\omega_{l,ref}$ is the motor reference speed and $k_{\omega_l p}$ and $k_{\omega_l i}$ are proportional and integral controller gains, respectively.

7. Simulation Results

The proposed control scheme as well as the respective MES and AES were implemented and evaluated using the SimPower System toolbox of Matlab (Matlab, Simulink. de 1994–2022, ©The Math Works, Inc.). The parameters of the AES and MES are listed in Table 1.

Table 1. Parameters of the AES and MES.

Description	Unit
Converter resistance R.	50 Ω
Converter inductance L	13×10^{-3} H
Converter capacitance C_1	2×10^{-3} F
Converter capacitance C_2	1×10^{-6} F
Supercapacitor voltage V_{sc}	350 V
Battery bank voltage V_c	500 V
Initial SOC	80%
Sampling time (t_s)	1×10^{-5} s

7.1. Neural Identification

The realized RHONN identification allowed us to obtain a satisfactory estimation of the system states, which were, in this case, the voltage x_1, k and the current x_2, k during different operation modes. Figure 1 demonstrates the neural identification of the voltage (x_1, k) and its respective neural weights' changes during the operation of the time-varying signals.

Figure 2 presents the neural identification of the current (x_2, k) and its respective neural weights' dynamics that adjust over the operation with the time-varying trajectories.

From the obtained results, it is clear that the proposed RHONN identifiers successfully approximated the voltage and the current dynamics of the AES, even though time-varying trajectories were applied. In addition, all neural weights were bounded. This allowed a correct operation for the recognition of the dynamics of the buck–boost converter because the capability of identifying these variables over time-varying signals let the system operate in different conditions. Furthermore, the implementation of the neural controller did not represent a problem, with the neural identifier working correctly.

7.2. Buck–Boost Trajectories Tracking

In this test, the objective was to demonstrate the trajectories tracking of the AES voltage and current to validate the correct operation of the proposed NIOC scheme. A trajectory was proposed to show the dynamics regulation without connecting the whole regenerative braking system.

The proposed trajectory to be tracked was a time-varying signal, whose amplitude was changed between 340 V and 360 V. Figure 3 presents the obtained results for the voltage (x_1, k) at the output of the buck–boost converter used in the AES system controlled by the proposed NIOC scheme. As is shown, the tracking made by the controller operated correctly and followed the variations of the signal.

Figure 4 demonstrates the behavior of the current (x_2, k), as measured at the inductance of the buck–boost converter. As a result of the good performance of the neural controller for the voltage (x_1, k), the regulation and tracking of the current dynamics worked correctly.

Figure 5a–c display the current, voltage, and state of charge (SOC) of the AES, respectively. Different voltage values were applied to verify the charging and discharging operations of the AES. The voltage had an initial value of 380 V where the buck mode was activated and the supercapacitor was charging. Then, at 25 s, the voltage value was modified to 340 V resulting in the boost mode turning on and the supercapacitor discharging. The conclusion obtained with the voltage values was that the supercapacitor had the capacity to work over charging and discharging operations, which helped extend the life cycle and SOC of the battery when the whole system was connected.

From the obtained results, it is clear that the proposed control scheme (NIOC) ensured the tracking of the proposed trajectories for both the voltage and current of the AES. In addition, the charging and discharging operation modes of the AES were achieved.

7.3. Regenerative Braking System Trajectories Tracking

The objective of this section was to test the complete system functionality including the AES, MES, and the DC motor installed on the EV. The trajectories to be tracked were calculated using the reference generative block (38) where the motor speed was the input and the voltage reference (V_{cr}) was the output. This voltage output was used in the control loop of the AES where a cascade-controller-based NIOC scheme was used to regulate the voltage and the current of the buck–boost converter, respectively, with the objective to ensure the charge and discharge of the AES supercapacitor. The speed of the DC motor was controlled by a PI controller where a time-varying trajectory was tracked as presented in Figure 6.

Figure 7 presents the voltage's desired trajectory tracking, obtained from the reference generator block (38), using NIOC when the EV was fully operated. During acceleration, the voltage value decreased toward 340 V, the boost mode was activated, and the supercapacitor was discharging, allowing the AES's participation in the total EV's needed energy; as a result, the MES's charge duration was enhanced. However, during deceleration the voltage value increased to reach 350 V, the buck mode was turned on, and the supercapacitor was charging, which helped to recuperate the EV energy waste.

Figure 8 illustrates the current trajectory tracking using the proposed NIOC during the regenerative braking, where the reference trajectory was obtained from the NIOC voltage controller.

Figure 10 displays the SOC behavior of the MES battery bank without (blue) and with (red) the AES during the operation of the regenerative braking system. This demonstrated the enhancement of the battery operation using the regenerative braking system. The results obtained showed that the battery SOC decreased slowly with the AES in comparison to when the AES was not implemented.

The SOC of the AES as well the supercapacitor voltage and current are presented in Figure 9, where the supercapacitor is discharging when the EV is in an acceleration state and charging otherwise.

As results of this experiment, the proposed control scheme ensured the trajectory tracking of the AES voltage obtained from the reference regenerative block. The voltage value was automatically changed according to the acceleration or deceleration of the motor EV. In addition, the proposed controller achieved an adequate trajectory tracking of the AES current. On the other hand, the SOC of the MES was largely improved by using the proposed AES control methodology, which helped to recuperate the energy during deceleration and enhance the MES's charge duration. This demonstrated that the regenerative braking system had a good performance and operation when implementing the complete scheme as illustrated in Figure 17. However, it is necessary to add another test to prove even further the good operation of the EV architecture proposed in this article.

7.4. Robustness Test

In this test, the AES parameters were changed to examine the robustness of the proposed NIOC. In addition, a comparison with the classical PI controller was done to

illustrate the potential of the proposed neural control scheme. The obtained results of the AES when varying the parameters are presented in Figures 11–13.

The goal of this test was to vary the nominal values of the components that integrate the AES parameters described before in Table 1 and demonstrate the capability of the neural controller to operate over changes in their conditions, which could be considered as parasitic signals that were not part of an ideal electric vehicle's system. Figure 11 illustrates the voltage and current trajectories tracking of the AES when resistor R was changed by 200% of its nominal value.

Figure 12 demonstrates the voltage and current trajectories tracking of the AES when inductance L was changed by 100% of its nominal value.

Figure 13 demonstrates the voltage and current trajectories tracking of the AES when resistor C was changed by 70% of its nominal value.

From the simulation results, we can observe that parameter variations had an important impact on the AES voltage and current controlled by the PI controller, with a high coupling between the control axes and a sluggish response time. However, the proposed controller (NIOC) ensured an adequate performance in the presence of parameter variations, the decoupling was ensured, and the response time was improved compared with that of the PI controller. From this test, we can consider that the proposed controller had better performance and was robust to AES parameter variations and these results were supported by the mean squared error calculated to validate the statement made with these results. Table 2 illustrates the results for the voltage control robustness test while Table 3 describes the mean squared error for the current dynamics. One of the disadvantages of the PID controller was its capacity to reach the trajectory desired, which meant the squared error was farther from zero in comparison with that of the NIOC.

Table 2. Mean squared error in x_1.

Mean Squared Error of Tracking Trajectories in x_1	
Controller	**Mean Value**
PID	16.026×10^{-11}
NIOC	4.8822×10^{-11}

Table 3. Mean squared error in x_2.

Mean Squared Error of Tracking Trajectories in x_2	
Controller	**Mean Value**
PID	140.290×10^{-9}
NIOC	2.2314×10^{-9}

8. Conclusions

This article presented a regenerative braking system for electrical vehicles controlled by a neural inverse optimal controller. The control scheme was used to regulate the dynamics of the AES composed of a buck–boost converter and a supercapacitor, with the objective to enhance the energy recovery during braking and to participate in the delivered MES's energy during acceleration. The proposed controller was developed using a recurrent high-order neural network identifier, and online training by the extended Kalman filter based algorithm, which allowed us to approximate the AES's behavior during the different operation modes. The validation of the correct identification of the dynamics with the RHONN was illustrated correctly with the results obtained in the simulation. This responded to one of the statements mentioned about the implementation and correct operation of recurrent high-order neural networks in nonlinear systems.

The neural controller test with the proposed time-varying trajectories helped to achieve the correct implementation and operation of the dynamics before the complete system was connected. This was considered because working with the complete regenerative braking system before the tuning of the controllers may present some issues that could easily be solved by analyzing the controller separately first. The controller was used to track the desired trajectories of the AES voltage and current, where a reference generator block was utilized to define the voltage's desired value considering the electrical vehicle operation modes. This reference generator block was very important because this helped to achieve the necessary current value for the correct operation of the regenerative braking system. It is important to note the effects that the DC motor had on the EV system and the good performance obtained by the neural controller. Additionally, the proposed controller was compared with the PI controller, regarding reference tracking and robustness against parameter variations. The obtained results illustrated the effectiveness of the proposed control scheme for the AES trajectory tracking even in the presence of time-varying references and disturbances. The mean squared error helped to get a better idea of the improvement that the neural controller presented over a PI controller in this case. The measure of the error showed by far the effectiveness of NIOC even in the presence of disturbances or undesired signals. In addition, the charging and discharging of the AES supercapacitor during acceleration and deceleration was ensured, which helped to recover the wasted energy during braking and to participate in the MES's power budget during acceleration; moreover, it increases the lifetime of the battery bank. As a result, the charge duration of the MES battery bank was largely enhanced, and the electric vehicle's efficiency and operation were improved. Finally, it is necessary to mention that a real-time implementation is very important to consider; thus, the validation of the proposed controller will let us know its real effectiveness in terms of real driving performance. Moreover, new approaches for the inverse optimal and another neural controller such as the neural sliding mode control could be the simulation of a fully electric vehicle model system, where more important variables such as temperature conditions are considered, and the controllers are validated during typical driving conditions.

Author Contributions: Conceptualization, L.D.; methodology, J.A.R.-H. and L.D.; validation, E.N.S. and M.B.; formal analysis, M.A.R.C. and L.D.; investigation, J.A.R.-H., M.A.R.C. and L.D.; software, M.A.R.C. and L.D.; writing—original draft preparation, M.A.R.C. and L.D.; writing—review and editing, M.A.R.C., J.R, L.D., E.N.S. and M.B.; funding acquisition, M.A.R.C. All authors have read and agreed to the published version of the manuscript.

Funding: This research was funded by Consejo Nacional de Ciencia y Tecnología (México) (1085717).

Data Availability Statement: Not applicable.

Conflicts of Interest: The authors declare no conflict of interest.

References

1. Pavlović, T.; Mirjanić, D.; Mitića, I.; Stanković, A. The Impact of Electric Cars Use on the Environment. In *New Technologies, Development and Application II. NT 2019*; Karabegović, I., Ed.; Lecture Notes in Networks and Systems; Springer: Sarajevo, Bosnia and Herzegovina, 2019; Volume 76, pp. 541–548. [CrossRef]
2. Yoong, M.K.; Gan, Y.; Gan, G.; Leong, C.; Phuan, Z.; Cheah, B.; Chew, K. Studies of regenerative braking in electric vehicle. In Proceedings of the 2010 IEEE Conference on Sustainable Utilization and Development in Engineering and Technology, Petaling Jaya, Malaysia, 20–21 November 2010; pp. 40–45.
3. Tran, M.-K.; Bhatti, A.; Vrolik, R.; Wong, D.; Panchal., S.; Flowler, M.; Fraser, R. A Review of Range Extenders in Battery Electric. *World Electr. Veh. J.* **2021**, *12*, 54. [CrossRef]
4. Tie, S.F.; Tan, C.W. A review of energy sources and energy management system in electric vehicles. *Renew. Sustain. Energy Rev.* **2013**, *20*, 82–102. [CrossRef]
5. Villalobos, J.G.; Zamora, I.; Martín, J.S.; Asensio, F.; Aperribay, V. Plug-in electric vehicles in electric distribution networks: A review of smart charging approaches. *Renew. Sustain. Energy Rev.* **2014**, *38*, 717–731. [CrossRef]
6. Hannan, M.A.; Azidin, F.; Mohamed, A. Hybrid electric vehicles and their challenges: A review. *Renew. Sustain. Energy Rev.* **2014**, *29*, 135–150. [CrossRef]

7. Ortuzar, M.; Moreno, J.; Dixon, J. Ultracapacitor-Based Auxiliary Energy System for an Electric Vehicle: Implementation and Evaluation. *IEEE Trans. Ind. Electron.* **2007**, *54*, 2147–2156. [CrossRef]
8. Husain, I.; Ozpineci, B.; Sariful, M.I.; Gurpinar, E.; Su, G.; Yu, W.; Chowdhury, S.; Xue, L.; Rahman, D.; Sahu, R. Electric drive technology trends, challenges, and opportunities for future electric vehicles. *Proc. IEEE* **2021**, *109*, 1039–1059. [CrossRef]
9. Zhang, L.; Cai, X. Control strategy of regenerative braking system in electric vehicles. *Energy Procedia* **2018**, *152*, 496–501. [CrossRef]
10. Xie, J.; Cao, B.; Zhang, H.; Xu, D. Switched robust control of regenerative braking of electric vehicles. In Proceedings of the the 2010 IEEE International Conference on Information and Automation, Harbin, China, 20–23 June 2010; pp. 1609–1612. [CrossRef]
11. Xu, W.; Chen, H.; Zhao, H.; Ren, B. Torque optimization control for electric vehicles with four in-wheel motors equipped with regenerative braking system. *Mechatronics* **2019**, *57*, 95–108. [CrossRef]
12. Kiddee, K.; Keyoonwong, W.; Khan-Ngern, W. An HSC/battery energy storage system-based regenerative braking system control mechanism for battery electric vehicles. *IEEJ Trans. Electr. Electron. Eng.* **2019**, *14*, 457–466. [CrossRef]
13. Indragandhi, V.; Selvamathi, R.; Gunapriya, D.; Balagurunathan, B.; Suresh, G.; Chitra, A. An Efficient Regenerative Braking System Based on Battery-Ultracapacitor for Electric Vehicles. In Proceedings of the 2021 Innovations in Power and Advanced Computing Technologies (i-PACT), Kuala Lumpur, Malaysia, 27–29 November 2021.
14. Manríquez, E.Q.; Sanchez, E.N.; Toledo, M.E.A.; Muñoz, F. Neural control of an induction motor with regenerative braking as electric vehicle architecture. *Eng. Appl. Artif. Intell.* **2021**, *104*, 104275. [CrossRef]
15. Guo, J.; Xiaoping, J.; Guangyu, L. Performance Evaluation of an Anti-Lock Braking System for Electric Vehicles with a Fuzzy Sliding Mode Controller. *Energies* **2014**, *7*, 6459–6476. [CrossRef]
16. Li, X.; Xu, L.; Hua, J.; Li, J.; Ouyang, M. Regenerative braking control strategy for fuel cell hybrid vehicles using fuzzy logic. In Proceedings of the 2008 International Conference on Electrical Machines and Systems, Wuhan, China, 17–20 October 2008; pp. 2712–2716.
17. Rajendran, S.; Spurgeon, S.; Tsampardoukas, G.; Hampson, R. Intelligent Sliding Mode Scheme for Regenerative Braking Control. *IFAC-PapersOnLine* **2018**, *51*, 334–339. [CrossRef]
18. Wu, J.; Lu, Y. Decoupling and optimal control of multilevel buck DC-DC converters with inverse system theory. *IEEE Trans. Ind. Electron.* **2019**, *67*, 7861–7870. [CrossRef]
19. Manriquez, E.Q.; Sanchez, E.N.; Harley, R.G.; Li, S.; Felix, R.A. Neural inverse optimal control implementation for induction motors via rapid control prototyping. *IEEE Trans. Power Electron.* **2018**, *34*, 5981–5992. [CrossRef]
20. Cao, F.; Yang, T.; Li, Y.; Tong, S. Adaptive Neural Inverse Optimal Control for a Class of Strict Feedback Stochastic Nonlinear Systems. In Proceedings of the 2019 IEEE 8th Data Driven Control and Learning Systems Conference (DDCLS), Dali, China, 24–27 May 2019; pp. 432–436. [CrossRef]
21. Sanchez, E.N.; Alanis, A.Y.; Loukianov, A.G. *Discrete-Time High Order Neural Control: Trained with Kalman Filtering*; Springer Science & Business Media: Cham, Switzerland, 2008. [CrossRef]
22. Rios, Y.Y.; Garcia-Rodriguez, J.A.; Sanchez, E.N.; Alanis, A.Y.; Velázquez, E.R. Rapid Prototyping of Neuro-Fuzzy Inverse Optimal Control as Applied to T1DM Patients. In Proceedings of the 2018 IEEE Latin American Conference on Computational Intelligence (LA-CCI), Gudalajara, Mexico, 7–9 November 2018; pp. 1–5. [CrossRef]
23. Djilali, L.; Vega, C.J.; Sanchez, E.N.; Hernandez, J.A.R. Distributed Cooperative Neural Inverse Optimal Control of Microgrids for Island and Grid-Connected Operations. *IEEE Trans. Smart Grid* **2022**, *13*, 928–940. [CrossRef]
24. Franco, M.L.; Sanchez, E.N.; Alanis, A.Y.; Franco, C.L.; Daniel, N.A. Decentralized control for stabilization of nonlinear multi-agent systems using neural inverse optimal control. *Neurocomputing* **2015**, *168*, 81–91. [CrossRef]
25. Cao, J.; Cao, B.; Xu, P.; Bai, Z. Regenerative-Braking Sliding Mode Control of Electric Vehicle Based on Neural Network Identification. In Proceedings of the 2008 IEEE/ASME International Conference on Advanced Intelligent Mechatronics, Xi'an, China, 2–5 July 2008; pp. 1219–1224. [CrossRef]
26. Djilali, L.; Sanchez, E.N.; Ornelas-Tellez, F.; Avalos, A.; Belkheiri, M. Improving Microgrid Low-Voltage Ride-Through Capacity Using Neural Control. *IEEE Syst. J.* **2020**, *14*, 2825–2836. [CrossRef]
27. Alanis, A.Y.; Sanchez, E.N.; Loukianov, A.G. Discrete-time adaptive backstepping nonlinear control via high-order neural networks. *IEEE Trans. Neural Netw.* **2007**, *18*, 1185–1195. [CrossRef] [PubMed]
28. Sanchez, E.; Ornelas, F. *Discrete-Time Inverse Optimal Control for Nonlinear Systems*, 1st ed.; CRC Press: Boca Raton, FL, USA, 2013. [CrossRef]
29. Freeman, R.; Kokotovic, P.V. *Robust Nonlinear Control Design: State-Space and Lyapunov Techniques*; Springer Science & Business Media: Cham, Switzerland, 2008. [CrossRef]
30. Ruiz-Cruz, R.; Sanchez, E.; Loukianov, A.; Ruz-Hernandez, J. Real-time neural inverse optimal control for a wind generator. *IEEE Trans. Sustain. Energy* **2018**, *10*, 1172–1183. [CrossRef]
31. Rovithakis, G.A.; Chistodoulou, M.A. *Adaptive Control with Recurrent High-Order Neural Networks: Theory and Industrial Applications*; Springer Science & Business Media: Cham, Switzerland, 2012. [CrossRef]
32. Utkin, V.; Guldner, J.; Shi, J. *Sliding Mode Control in Electro-Mechanical Systems*; CRC Press: Boca Raton, FL, USA, 2017. [CrossRef]
33. Zohuri, B. *Scalar Wave Driven Energy Applications*; Springer: Cham, Switzerland, 2019. [CrossRef]

energies

MDPI

Article

A New Bearing Fault Detection Strategy Based on Combined Modes Ensemble Empirical Mode Decomposition, KMAD, and an Enhanced Deconvolution Process

Yasser Damine [1], Noureddine Bessous [2], Remus Pusca [3], Ahmed Chaouki Megherbi [1], Raphaël Romary [3,*] and Salim Sbaa [4]

[1] Laboratory of Identification, Command, Control and Communication (LI3C), Department of Electrical Engineering, University of Mohamed khider, Biskra 07000, Algeria
[2] Laboratoire de Genie Electrique et des Energies Renouvelables (LGEERE), Department of Electrical Engineering, Faculty of Technology, University of El Oued, El Oued 39000, Algeria
[3] Univ. Artois, UR 4025, Laboratoire Systèmes Electrotechniques et Environnement (LSEE), F-62400 Béthune, France
[4] Department of Electrical Engineering, Faculty of Technology, University of Mohamed Khider, Biskra 07000, Algeria
* Correspondence: raphael.romary@univ-artois.fr

Abstract: In bearing fault diagnosis, ensemble empirical mode decomposition (EEMD) is a reliable technique for treating rolling bearing vibration signals by dividing them into intrinsic mode functions (IMFs). Traditional methods used in EEMD consist of identifying IMFs containing the fault information and reconstructing them. However, an incorrect selection can result in the loss of useful IMFs or the addition of unnecessary ones. To overcome this drawback, this paper presents a novel method called combined modes ensemble empirical mode decomposition (CMEEMD) to directly obtain a combination of useful IMFs containing fault information. This is without needing to pass through the processes of IMF selection and reconstruction, as well as guaranteeing that no defect information is lost. Owing to the small signal-to-noise ratio, this makes it difficult to determine the fault information of a rolling bearing at the early stage. Therefore, improving noise reduction is an essential procedure for detecting defects. The paper introduces a robust process for extracting rolling bearings defect information based on CMEEMD and an enhanced deconvolution technique. Firstly, the proposed CMEEMD extracts all combined modes (CMs) from adjoining IMFs decomposed from the raw fault signal by EEMD. Then, a selection indicator known as kurtosis median absolute deviation (KMAD) is created in this research to identify the combination of the appropriate IMFs. Finally, the enhanced deconvolution process minimizes noise and improves defect identification in the identified CM. Analyzing real and simulated bearing signals demonstrates that the developed method shows excellent performance in extracting defect information. Compared results between selecting the sensitive IMF using kurtosis and selecting the sensitive CM using the proposed KMAD show that the identified CM contains rich fault information in many cases. Furthermore, our comparisons revealed that the enhanced deconvolution approach proposed here outperformed the minimum entropy deconvolution (MED) approach for improving fault pulses and the wavelet de-noising method for noise suppression.

Keywords: combined modes ensemble empirical mode decomposition; KMAD indicator; three-sigma rule; enhanced minimum entropy deconvolution; rolling element bearing faults; fault detection

Citation: Damine, Y.; Bessous, N.; Pusca, R.; Megherbi, A.C.; Romary, R.; Sbaa, S. A New Bearing Fault Detection Strategy Based on Combined Modes Ensemble Empirical Mode Decomposition, KMAD, and an Enhanced Deconvolution Process. *Energies* **2023**, *16*, 2604. https://doi.org/10.3390/en16062604

Academic Editors: Moussa Boukhnifer and Larbi Djilali

Received: 6 February 2023
Revised: 2 March 2023
Accepted: 4 March 2023
Published: 9 March 2023

1. Introduction

The large-scale use of induction machines accounts for 90% of the industry's total energy consumption. Several defects often lead to unexpected failures. These defects can lead to severe damage to the machine if they are overlooked initially. According to previous

studies, the high percentage of failures in induction machines is caused by bearing faults. As a result, it is highly recommended to monitor small and medium voltage machines continuously for bearing faults [1,2]. Bearing health condition is commonly monitored by vibration monitoring. The vibration signals provide a wealth of information regarding machine health conditions [3]. Many approaches aim to pick up the characteristic defect information from the rolling bearing's non-stationary and nonlinear vibration signal by employing appropriate signal processing techniques. Huang et al. [4] created a time-frequency analysis approach known as empirical mode decomposition (EMD). EMD differs from short-time Fourier transform and wavelet transform as it is not dependent on the basis function. It is based on adaptive decomposition characteristics and decomposes signals into intrinsic mode functions (IMFs). EMD is suitable for non-stationary and non-linear vibration signals analysis [5], such as bearing faults, and has been widely used for this purpose. However, a significant problem with EMD is the mixing of modes. As a solution to this challenge, an improved version of EMD called ensemble empirical mode decomposition (EEMD) is proposed in [6]. An IMF in the EEMD consists of the average of a set of trials. The results of the EMD decomposition are used for each trial and a finite-amplitude white noise [7]. Compared to the EMD, IMFs produced by the EEMD can better highlight the signal's significant features. The focus of researchers has always been on how to identify EEMD's important IMFs and how to improve the level of noise minimization. These two main issues will be briefly discussed below.

Considering that the decomposed bearing vibration signal contains some IMFs representing defect features, as well as other IMFs containing unused information, researchers have focused on identifying suitable IMFs. Wang et al. [8] suggested the use of the highest value of kurtosis to pick the relevant IMF. Yang et al. [9] selected the effective IMF using mutual information. Li J et al. [10] calculated each IMF's similarity to the input signal based on Spearman's rho to identify the required IMF. A merit index for determining the relevant IMF has been proposed in [11]. However, if only the most suitable IMF is considered, fault information contained in other IMFs may be lost. In contrast, Li Z et al. [12] developed a weighted kurtosis index difference spectrum (WKIDS) to choose the important IMFs. Ma et al. [13] used the correlation coefficient to select the effective IMFs. Luo et al. [14] identified the effective IMFs by using high kurtosis values. However, Damine et al. [15] demonstrated that choosing the most suitable IMF can result in the loss of other important IMFs, and that selecting multiple IMFs can result in the inclusion of unnecessary ones. To address the abovementioned issues, this paper offers a novel approach called combined modes ensemble empirical mode decomposition (CMEEMD). This method is based on the extraction of combined modes (CMs) from the measured vibration signal. After that, a selection indicator is created to identify the combination of suitable IMFs. The purpose of this step is to obtain the most information about the defect directly from the input signal, without having to pass through the IMFs selection and reconstruction processes. It also ensures that no information about the defect is wasted or irrelevant data are included.

Owing to the effect of surrounding noise, extracting bearing fault information at the early stage of damage is challenging. Therefore, it is essential to reveal the defect pulses in the vibration signal. The most commonly used deconvolution process is the minimum entropy deconvolution (MED). The MED is designed to retrieve the bearing defect pulses in the input signal. Pennacchi et al. [16] examined the efficiency of the MED on experimental signals and found that it can detect bearing defects. However, when the original signal contains noise, the efficiency of MED is reduced. In addition, the output of MED will also be affected by noise interference. Therefore, researchers were concentrated on increasing the efficiency of the MED. Chatterton et al. [17] combined EMD with MED to improve bearing defect detection. Ding et al. [18] introduced a deconvolution process using autoregressive MED for extracting bearing features.

In view of the above considerations, this paper presents an enhanced deconvolution approach, which focuses on eliminating the noise interference in the MED output by introducing a de-noising method derived from the three-sigma rule [19]. A new procedure

for extracting bearing defect features based on CMEEMD and an enhanced deconvolution process is discussed in this research work. The following describes the originality of these procedures. Firstly, the proposed CMEEMD decomposes the original signal into CMs. An indicator is created to identify the appropriate combination that combines the effective IMFs instead of selecting and reconstructing them. Secondly, an enhanced deconvolution process based on MED and a noise suppression technique using the three-sigma rule is performed on the selected CM. Finally, the envelope spectrum is applied, and the characteristic fault frequency is extracted to diagnose the bearing fault.

The remaining sections of this paper are organised as following: Section 2 is dedicated to the basic theories of EEMD, MED, and the rule of three-sigma de-noising method. Section 3 details the proposed methods of this research. Section 3.1 gives the steps of the CMEEMD. In Section 3.2, the process of selecting an appropriate combination is introduced. In Section 3.3, the enhanced deconvolution strategy is presented. Section 3.4 describes the new bearing fault diagnosis procedure. Section 4 presents the results of applying the proposed method to the simulated signal. In Section 5, the suggested process is performed on the experimental data, and the results are verified. In Section 6, the conclusion of this paper is presented.

2. Theoretical Analysis

2.1. EEMD Method

By comparing EEMD and EMD, it has been concluded that EEMD may be more effective at revealing the characteristic fault information of rolling element bearings [20]. EEMD solves the problem of mode mixing in EMD by adding Gaussian white noise to the original signal. Thus, we can better highlight the signal's intrinsic characteristics. The algorithm of EEMD [7] is given below, and Figure 1 shows the process flow diagram.

(1) Add a random white Gaussian noise $\beta\ w_i(t)$ to the existing signal:

$$x_i(t) = x\ (t) + \beta\ w_i(t) \tag{1}$$

where $\beta\ w_i(t)$ is the i-th added white noise series, and $x_i(t)$ represents the noise-added signal (i = 1, 2, . . . , i).

(2) Divide by EMD the novel signal and obtain N sets of IMFs:

$$x_i(t) = \sum_{j=1}^{N} c_{ij}(t) + r_i \tag{2}$$

where $c_{ij}(t)$ is the IMFs and r_i. is the residue.

(3) Using the formula below, determine the ensemble means $c_j(t)$ of the I trials:

$$c_j(t) = \sum_{i=1}^{I} c_{ij}(t) \tag{3}$$

where $c_j(t)$ (c_1, c_2,..., c_N) is the IMFs divided by EEMD.

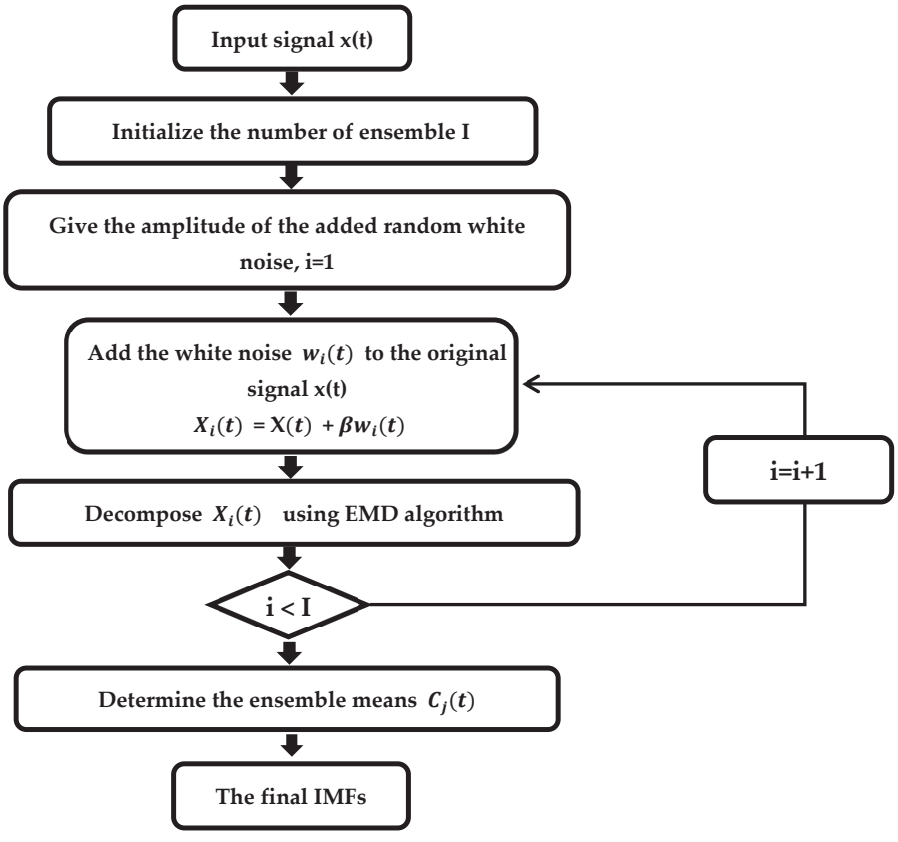

Figure 1. Flow chart of the ensemble empirical mode decomposition (EEMD) algorithm to obtain the intrinsic mode functions (IMFs).

2.2. Minimum Entropy Deconvolution Technique

MED was originally introduced by Ralph [21]. The MED highlights the transient components of the signal with a finite impulse response (FIR) filter. It decreases a signal's randomness by minimizing its entropy. Two terms can represent a general signal x(n):

$$x(n) = z(n) * w(n) + \eta(n) \tag{4}$$

There is a convolution between the defect impulse z and its excitation w, which is the first term in the equation. The second term takes a random noise into account. FIR filter h(n) can be used in minimum entropy deconvolution (MED) to process the original signal. From [22,23], it is possible to obtain:

$$u(n) = x(n) * h(n) = \sum_{i=0}^{M-1} h(i)x(n-i) \tag{5}$$

where $n = 0, 1, \ldots,$ N, N= T + M − 2. The deconvolution filter length is M, and the input sequence $x(n)$ length is T. In MED, a signal's entropy is minimized by maximizing the Varimax function. The Varimax function for $u(n)$ is:

$$V(u) = \frac{\sum_{n=0}^{N} u^4(n)}{(\sum_{n=0}^{N} u^2(n))^2} \tag{6}$$

The filtering parameters that maximize $V(u)$ are such that:

$$\frac{\partial V(u)}{\partial h(n)} = 0 \tag{7}$$

As a result of substituting Equations (6) in (7) and solving the derivative, we obtain:

$$\sum_{i=0}^{M-1} h(i) \sum_{n=0}^{N} x(n-i)x(n-k) = \sum_{n=0}^{N} \frac{u^3(n)x(n-k)}{V(\mathbf{u}) \parallel \mathbf{u} \parallel^2} \tag{8}$$

where $k = 0, 1, \ldots, M-1$.

Equation (8) can be written as:

$$R_{XX}h \; = \; b \tag{9}$$

where R_{XX} corresponds to a matrix of autocorrelation, h is the filter coefficients vector, and b includes the input of the filter x(n) cross-correlated with the cube of its output u(n). The following steps summarize the optimal inverse filter solution:

- Assume that h(0) is a set of initial filter coefficients;
- Calculate u(0) and V(u);
- Calculate R_{xx}
- Determine b(1) and h(1);
- Repeat the procedure until an optimal filter is obtained.

2.3. The Three-Sigma Rule for Noise Minimization

In probability and statistics, the three-sigma rule states that approximately 99.73% of data following a normal distribution are located inside a range of three standard deviations from the mean [24].

$$P\{\mu - 3\sigma < Y < \mu + 3\sigma\} \approx 99.73\% \tag{10}$$

The mean and standard deviation are represented by μ and σ, respectively. The normal distribution appears with:

$$E(Y) = \mu \; = \; 0 \tag{11}$$

$$D(Y) = E\left(Y^2\right) - [E(Y)]^2 = \; E\left(Y^2\right) = \sigma^2 \tag{12}$$

The variance and the expectation are represented by $D(Y)$ and $E(Y)$, respectively.

Based on Equation (12), the root mean square (RMS) value of Y is:

$$Yrms \; = \; \sqrt{\frac{1}{n}\sum_{i=1}^{n}[X_i, -, E(Y)]^2} = \sqrt{\frac{1}{n}\sum_{i=1}^{n} {y_i}^2} = \sqrt{E(Y)} = \sigma \tag{13}$$

where y_i stands for the sample data of Y and n for the number of samples.

Using Equations (11) and (13), Equation (10) can be written as:

$$P\{-3\sigma < Y < 3\sigma\} = P\{-3Y_{rms} < Y < 3Y_{rms}\} \approx 99.73\% \tag{14}$$

Based on the assumption that a fault-free rolling bearing follows the normal distribution [25], Equation (14) shows that nearly all the noise in the bearing vibration signal Y is distributed within $\pm 3Y_{rms}$. Due to this, it is necessary to remove the components within $\pm 3Y_{rms}$. The steps of the de-noising process are as follows [26]:

1. y (t) is normalized by using zero-mean normalization:

$$Z(t) = \frac{y - \mu}{\sigma} \tag{15}$$

where Z(t) is the normalized signal.

2. Determine Z_{rms} of Z(t);
3. Replace the sampling data z_i of Z(t) falling between $\pm 3Z_{rms}$ with zero while leaving z_i outside of $\pm 3Z_{rms}$ unchanged.

$$w(t) = \begin{cases} 0, & \text{if } |z_i| \leqslant 3Z_{rms} \\ z_i(t), & \text{otherwise} \end{cases} \tag{16}$$

where w(t) represents y(t) after removing the unnecessary components.

3. Proposed Methods

3.1. Combined Modes Ensemble Empirical Mode Decomposition (CMEEMD)

The proposed CMEEMD aims to extract all the CMs from the adjoining IMFs decomposed from the bearing fault vibration signal using EEMD. This process is described in detail below with a flowchart shown in Figure 2. In this paper, adjoining IMFs are combined using the following expression:

$$CM_{i \to j} = IMF_i + \ldots + IMF_j \tag{17}$$

where $CM_{i \to j}$ is the combined modes of adjoining IMFs from the i-th mode to the j-th mode, IMF_i is the IMF that starts the combination, and IMF_j is the IMF that finishes it. Extraction of CMs is done as follows:

- Divide these CMs into groups. The first group consists of CMs starting with IMF_1. By using Equation (17), we obtain:

$$CM_{1 \to j} = IMF_1 + \ldots + IMF_j \quad 2 \leq j \leq N \tag{18}$$

where $CM_{1 \to j}$ is the combination of adjoining IMFs from IMF_1 to the j-th IMF for j = 2, ... N, N is the number of IMFs.

- Using Equation (18), extract all CMs starting with IMF_1:

$$\begin{aligned} CM_{1 \to 2} &= IMF_1 + IMF_2 \\ CM_{1 \to 3} &= IMF_1 + IMF_2 + IMF_3 \\ &\vdots \\ CM_{1 \to N} &= IMF_1 + IMF_2 + IMF_3 + \ldots + IMF_N \end{aligned} \tag{19}$$

- The second group is constituted by CMs starting with the second mode. In this case, Equation (17) can be expressed as:

$$CM_{2 \to j} = IMF_2 + \ldots + IMF_j \quad 3 \leq j \leq N \tag{20}$$

where $CM_{2 \to j}$ is the combination of adjoining IMFs from IMF_2 to the j-th IMF for j = 3, ... N.

- Using Equation (20), extract all CMs starting with IMF_2:

$$\begin{aligned} CM_{2 \to 3} &= IMF_2 + IMF_3 \\ CM_{2 \to 4} &= IMF_2 + IMF_3 + IMF_4 \\ &\vdots \\ CM_{2 \to N} &= IMF_2 + IMF_3 + IMF_4 + \ldots + IMF_N \end{aligned} \tag{21}$$

- The process continues until we reach the $N-1$ group. In this case, the last combination can be represented by the following equation:

$$CM_{N-1\rightarrow N} = IMF_{N-1} + IMF_N \quad (22)$$

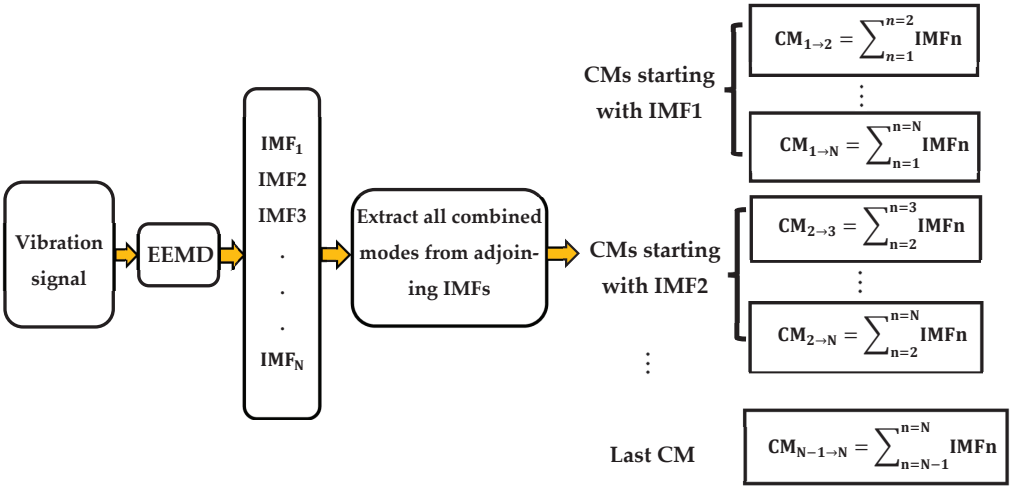

Figure 2. Flow chart of the proposed combined modes ensemble empirical mode decomposition (CMEEMD).

3.2. Sensitive CM Selection Using KMAD Indicator

Once all the CMs have been extracted, we need to identify the appropriate combination of sensitive IMFs. An indicator was required to select this combination among all the other CMs. In many studies, maximum kurtosis was used to identify the most sensitive IMF. However, if we consider only the best IMF, we may lose information about faults contained in other IMFs [27]. Therefore, this paper uses the kurtosis of the combined IMFs. The probability of identifying the appropriate combination is higher when the kurtosis value of the corresponding combination is high. The expression of kurtosis is defined as follows [28]:

$$K = \frac{1}{N}\sum_{i=1}^{N}\frac{(x_i-\mu)^4}{\sigma^4} \quad (23)$$

where the amplitude of the vibration waveform is indicated by x_i, the mean of the signal by μ, the standard deviation by σ, and the length of the samples by N. According to [29–31], IMFs with high-frequency bands of the vibration signal contain the main fault information about the rolling bearings. It is known that the higher the frequency band, the larger the median absolute deviation (MAD). Therefore, the MAD can be used to identify IMFs with high-frequency bands. The expression of MAD is defined as follows [32]:

$$MAD\,(y) = \text{median}\,(|y_n - \text{median}(y)|) \quad (24)$$

where y_n represents the n-th sampling of the signal y. To ensure that only sensitive IMFs are combined in the effective combination, the proposed selection indicator aims to prevent unwanted IMFs from being added. Accordingly, as the number of IMFs in the combination decreases, the probability of obtaining the required combination increases. Based on all the

above, the paper proposes an indicator (KMAD), which combines kurtosis and MAD to select the appropriate combination of sensitive IMFs.

$$KMAD_{i\to j} = \frac{K_{i\to j} \ . MAD_i}{\sum_i^j MAD_n} \tag{25}$$

In this equation, $K_{i\to j}$ is the kurtosis value of $CM_{i\to j}$, where $CM_{i\to j}$ is the combined modes of adjoining IMFs from the i-th IMF to the j-th IMF, MAD_i is the mean absolute deviation of the i-th IMF that starts the combination, and $\sum_i^j MAD_n$ means the sum of MADs of IMFs from the i-th IMF to the j-th IMF. A combination with fewer IMFs has a lower value of $\sum_i^j MAD_n$, which increases the probability of obtaining the combination of useful IMFs. For each $CM_{i\to j}$, $KMAD_{i\to j}$ is calculated, where the highest value corresponds to the required combination.

3.3. The Enhanced Deconvolution Process

One of the most commonly used methods for this is MED. However, when the input signal contains noise, the effectiveness of the MED will be reduced. For this reason, noise will affect the MED output. Therefore, an enhanced deconvolution approach is presented in this paper, which aims to minimize noise interference in the MED output by integrating the three-sigma rule (see Section 2.3). Figure 3 is a flow chart illustrating the enhanced MED strategy, and the steps are as follows:

1. Apply the MED technique to the input signal;
2. Perform the de-noising method derived from the three-sigma rule on the MED output. It consists of the following steps:

- Normalize the MED output using zero-mean normalization;
- Calculate the root mean square value Y_{rms} of the normalized signal Y(t);
- Replace the sampling data y_i of Y(t) falling between $\pm 3Y_{rms}$ with zero while keeping y_i outside of $\pm 3Y_{rms}$ unmodified.

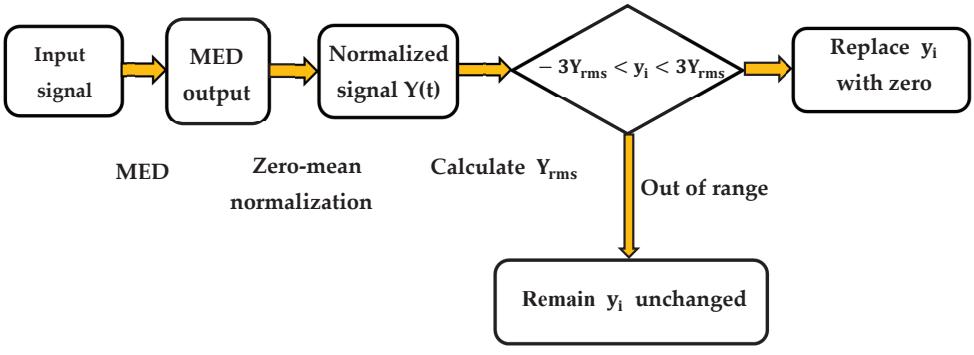

Figure 3. Proposed enhanced deconvolution process flowchart.

3.4. The Proposed Strategy for Bearing Fault Detection

This paper describes a novel feature extraction method based on CMEEMD and proposes a deconvolution process to diagnose the bearing fault from the vibration signals. Figure 4 illustrates the flowchart of the proposed method for detecting bearing defects. The detailed process of the feature extraction method proposed is as follows:

1. Perform CMEEMD on the fault vibration signal as follows:
   - Decompose the fault vibration signal with the defect into IMFs by EEMD;
   - Extract all combined modes (CMs) from adjoining IMFs (see Section 3.1).

2. Select the appropriate combination using the KMAD indicator (see Section 3.2):
   - Calculate the KMAD value of each CM;
   - Select the required combination based on the highest value of KMAD.
3. Perform the enhanced deconvolution process on the selected CM (see Section 3.3).

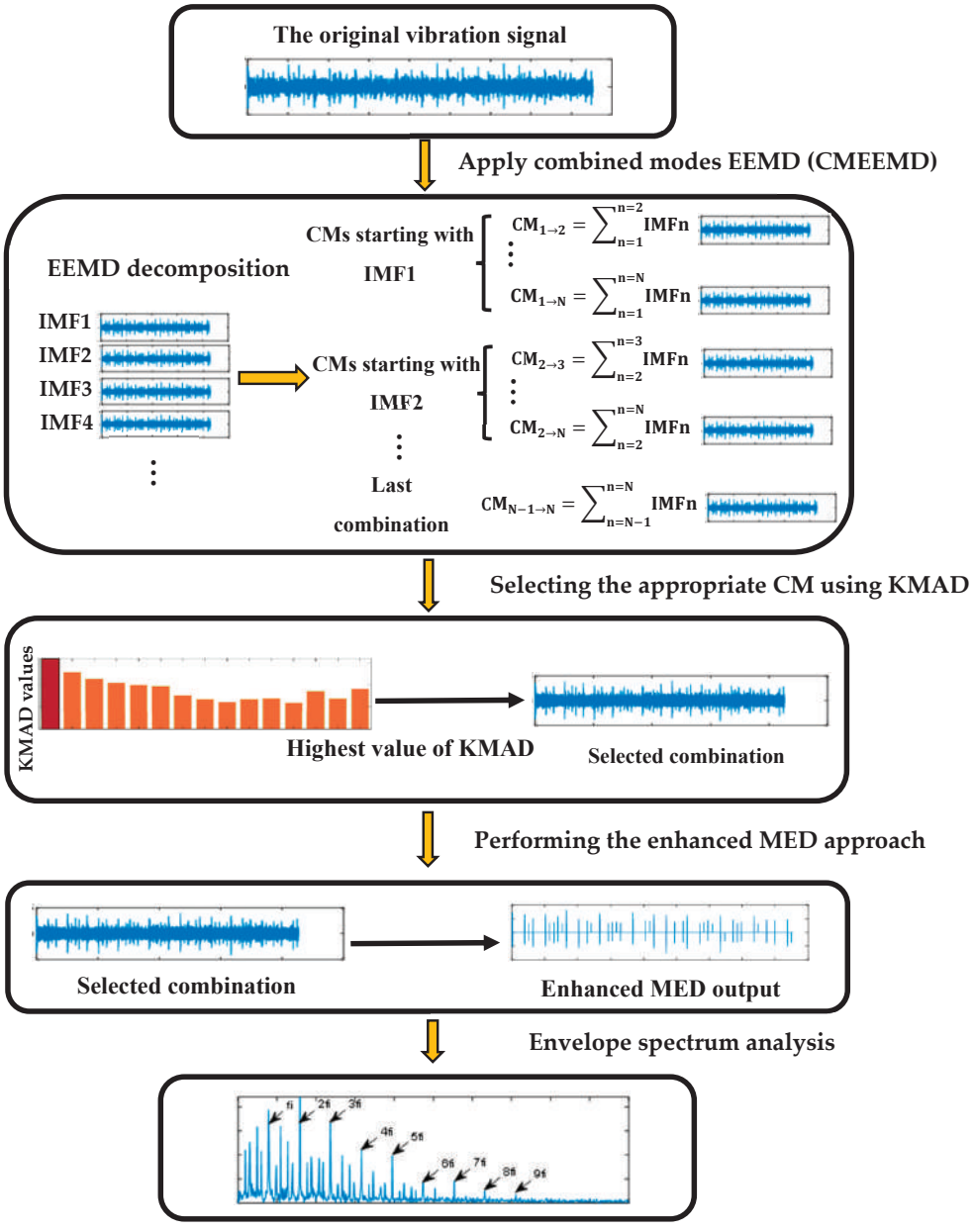

Figure 4. Proposed strategy using CMEEMD, kurtosis median absolute deviation (KMAD) and an Enhanced Deconvolution Process for diagnosing bearing faults.

4. The Simulation Validation

A simulation of an inner ring defect bearing is presented in this section to illustrate the effectiveness and usefulness of the suggested method for extracting fault characteristics. The periodic impulses represent the vibration waveform caused by a local failure in the bearing. However, these impulses are usually buried in white noise. As a result, we can obtain the simulated signal of the rolling bearing from [33]. In this paper, the sampling frequency is 12,000 Hz, the resonant frequency is 3000 Hz, the inner-race fault frequency is 79 Hz, the time lag is zero, the rotational frequency is 28 Hz, and the damping ratio B = 500. The random noise has a zero mean and variance of $\sigma^2 = 0.7^2$. The data length of the signal is 10,240. The simulated signal y(t) is plotted in Figure 5a. It can be seen that the noise effect prevents the extraction of periodic impulses. From the envelope spectrum in Figure 5b, although the fault characteristic fi and the first harmonic 2fi can be extracted, the remaining harmonics are covered by noise interference. To improve fault detection, this signal needs to be pre-processed.

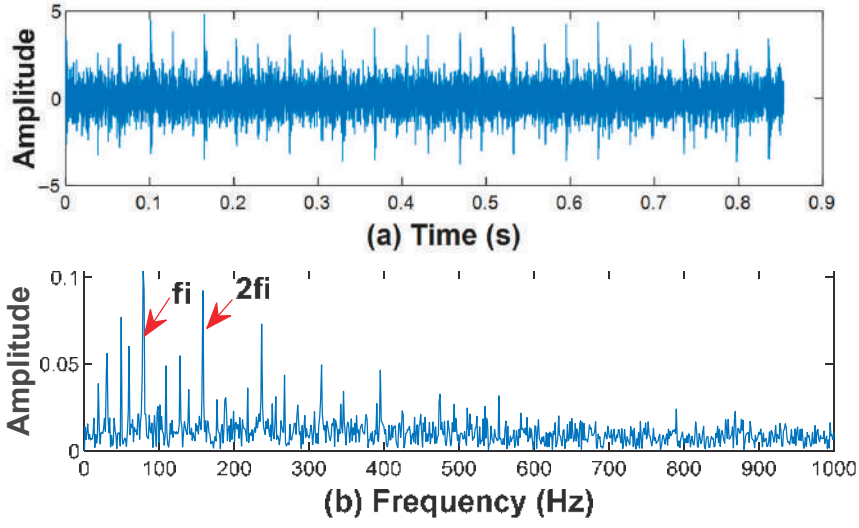

Figure 5. Inner ring fault simulated signal: (**a**) waveform; (**b**) envelope spectrum.

4.1. Analysis of the Proposed Method

Based on the detailed flowchart of the proposed feature extraction method described in Figure 4, the following processes are followed.

4.1.1. CMEEMD Analysis

According to [29–31], the significant defect information about rolling bearings is included in IMFs with high-frequency bands. Therefore, the proposed CMEEMD uses the EEMD to decompose this simulated signal into six IMFs. Then, one extracts all the CMs from the adjoining IMFs. Based on the recommended method for extracting combined modes CMs detailed in Section 3.1, fifteen CMs are generated from the six IMFs. The obtained IMFs are plotted in Figure 6, and the extracted CMs are illustrated in Figure 7. The next step identifies the most sensitive combination.

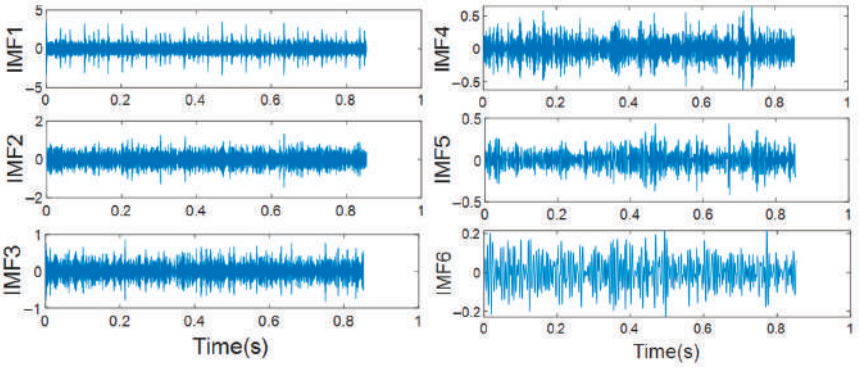

Figure 6. Decomposed result of the simulated signal by EEMD.

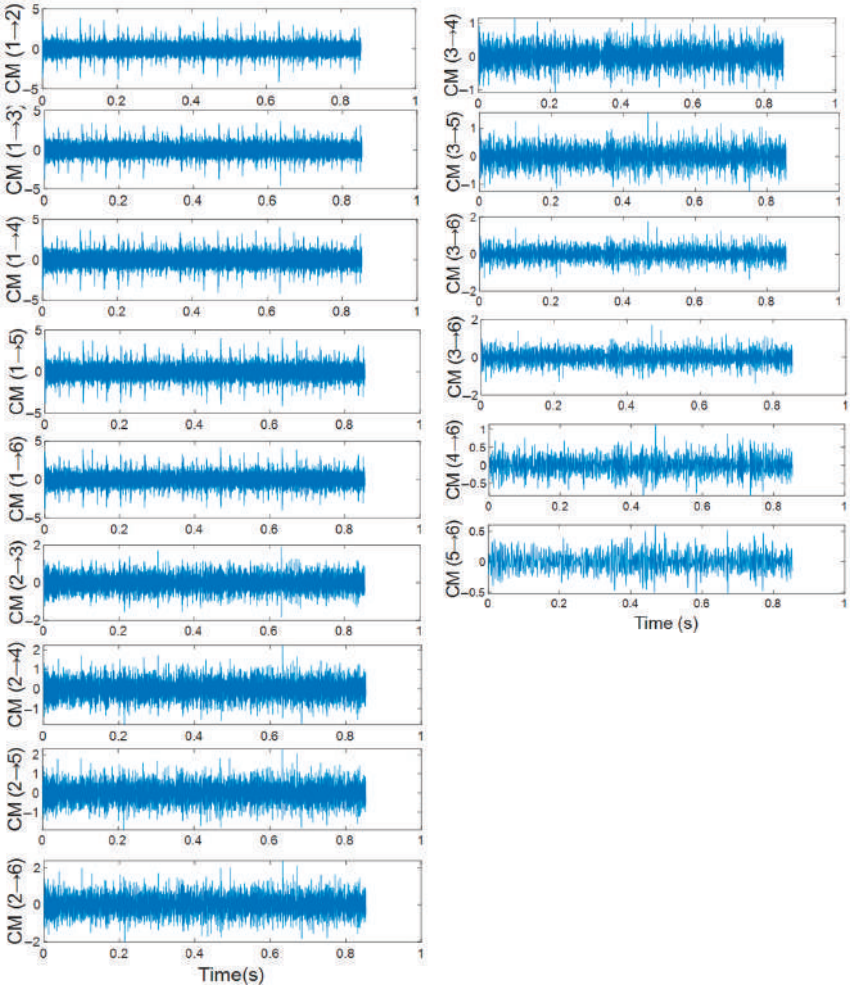

Figure 7. Extracted Combined modes (CMs) from the adjoining IMFs.

4.1.2. Selecting the Appropriate CM

Based on the time-domain waveforms given in Figure 7, the differences between the CMs are insignificant. Therefore, the most effective combination is selected using the proposed KMAD indicator. Based on Equation (25), the KMAD values of each combination are illustrated in Figure 8. It is observed that the combination $CM_{1\rightarrow 2}$ has the highest value among all the other combinations. This indicates that it is the appropriate combination of the sensitive IMFs, i.e., IMF1 and IMF2.

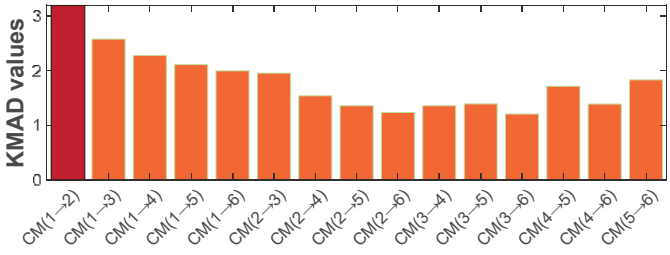

Figure 8. Kurtosis median absolute deviation (KMAD) values of each combination.

4.1.3. Performing the Proposed Deconvolution Process

This method focuses on minimizing noise interference in the MED output. The first step is to highlight the fault impulses in selected combination $CM_{1\rightarrow 2}$ using MED. Following that, we minimize the noise using the rule of three-sigma. As illustrated in Figure 9a, the noise is minimized, and the fault impulses are emphasized. From the envelope spectrum in Figure 9b, we can efficiently and accurately extract the inner race fault characteristic frequency f_i and nine harmonics ($2f_i$, $3f_i$, $4f_i$, $5f_i$, $6f_i$, $7f_i$, $8f_i$, $9f_i$, and $10f_i$). This indicates that the rolling bearing fault feature extraction method proposed in this paper can extract fault information excellently.

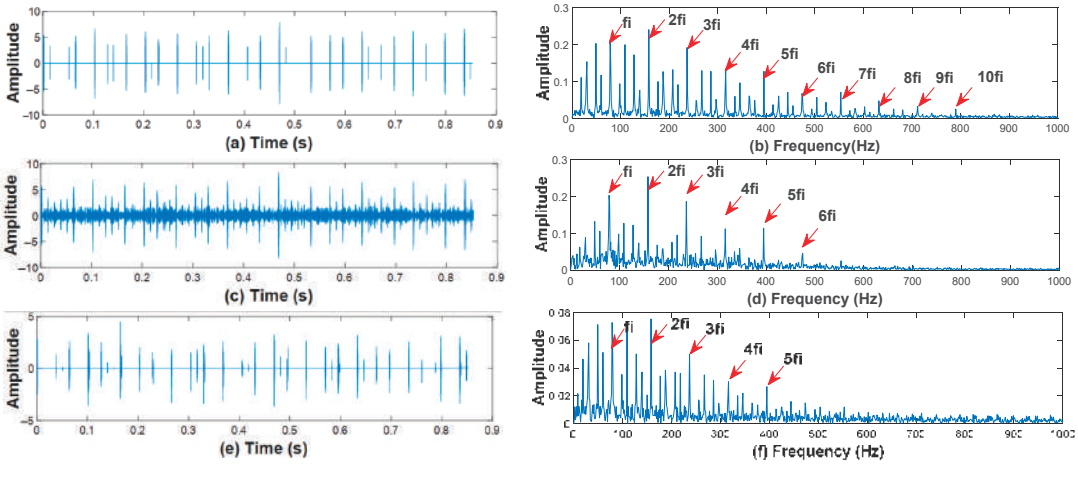

Figure 9. Simulated bearing fault diagnosis results for processing the selected CM using: proposed method (**a**,**b**); conventional MED (**c**,**d**); and wavelet denoising (**e**,**f**).

4.2. Advantages of the Proposed Methods for the Diagnosis of the Simulated Signal

To demonstrate the superiority of the proposed enhanced deconvolution process, the conventional MED is performed on the selected combination $CM_{1\rightarrow 2}$. Figure 9c,d shows the results of processing the selected combination $CM_{1\rightarrow 2}$. by the MED. As shown in

Figure 9c, the fault impulses are highlighted, and the noise level is decreased. However, some noise interference can still be seen. By comparing it with Figure 9a, it is clear that noise interference has been reduced significantly. From the envelope spectrum in Figure 9d, we can extract only the inner race fault characteristic frequency f_i and five harmonics ($2f_i$, $3f_i$, $4f_i$, $5f_i$, and $6f_i$). In comparison with Figure 9b, it is apparent that we can get more fault information. The comparison results demonstrate that the proposed enhanced MED outperformed the MED for improving fault detection. To demonstrate the superiority of the enhanced MED approach in minimizing noise, the wavelet de-noised method is performed on the selected combination $CM_{1\to2}$. Figure 9e shows that the noise interference is reduced to some extent; however, the extracted fault frequency and its harmonics in Figure 9f are not as good as in Figure 9b. In this case, the wavelet de-noising method is less efficient in suppressing noise, making it difficult to extract fault information from the combination $CM_{1\to2}$. The results demonstrate that the proposed enhanced MED outperformed the wavelet de-noising method in suppressing noise. The inter-harmonics (inter-characteristic frequencies of the faults) present the harmonics of the rotational frequency which are considered as extracted information. In Figure 9b, one can see that the harmonics multiple of the rotational frequency are obvious, while they are hidden in Figure 9d. This is due to the fact that the noise has been minimised in Figure 9a. In addition, a comparison of the conventional IMF selection method using maximum kurtosis with the proposed KMAD selection indicator is presented to illustrate its advantages. Table 1 shows the kurtosis values of the first six IMFs. It can be seen that IMF1 has the highest value of all the decomposition results, so it is selected as a sensitive IMF. IMF1 was treated using the enhanced deconvolution approach. As shown in the envelope spectrum of Figure 10a, the extracted fault information is weaker than the extracted fault information in Figure 10b. This indicates that the combination $CM_{1\to2}$ contains rich fault feature information. The KMAD indicator identified $CM_{1\to2}$ as a combination of suitable IMFs, i.e., IMF1 and IMF2. Consequently, if we choose only IMF1, the information contained in IMF2 will be lost. This proves that selecting the appropriate combination using the KMAD selection indicator overcomes the drawback of the IMF selection method using kurtosis to ensure that no information about the defect is lost.

Table 1. Kurtosis values of each intrinsic mode function (IMF).

IMF	Kurtosis
IMF1	4.6127
IMF2	3.2595
IMF3	3.0748
IMF4	3.0268
IMF5	2.9883
IMF6	2.8621

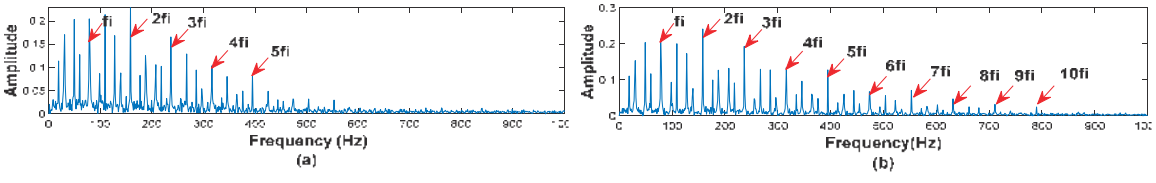

Figure 10. Diagnosis results of the simulated bearing fault using: (**a**) sensitive IMF-based Kurtosis; (**b**) sensitive CM-based KMAD.

5. Experimental Validation

Experimental data from the Case Western Reserve University [34] was used to validate the proposed method's effectiveness for detecting rolling bearing faults. As shown in Figure 11, the experimental set is composed of a 2 hp motor, a torque sensor/encoder, a dynamometer, and control electronics. Single point faults were introduced using electro-discharge machining, providing defects in the outer ring, the ball, and the inner ring. The rotating speed of the shaft varied from 1730 to 1797 RPM. We used the time signal of the drive end bearing in this study, recorded for the inner race, outer race, and ball fault. The data were gathered with 12,000 Hz. The deep groove ball bearing 6205-2RS JEM SKF was used in this experimental test. The bearing parameters are detailed in [34]. The bearing defect is localized in the early stages: a crack or spall. Rolling elements generate shock impulses every time they hit a local fault in the inner or outer ring. These repeated shock pulses produce a vibration at the frequency associated with the faulty element. This frequency is usually called the fault characteristics frequency, for example, BPFI (ball passing frequency inner race), BPFO (ball passing frequency outer race), and BFF (ball fault frequency), which are related to the inner race, the outer race, and the ball, respectively. The following are their mathematical equations [35]:

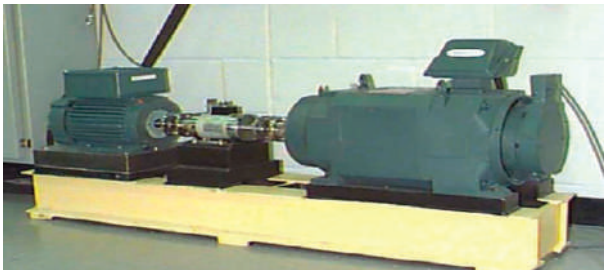

Figure 11. Experimental test rig from the Case Western Reserve University (CWRW) [34].

$$\mathrm{BPFI} = \frac{f_r}{2} N_b \left(1 + \frac{D_b \mathrm{COS}\beta}{D_c}\right) \tag{26}$$

$$\mathrm{BPFO} = \frac{f_r}{2} N_b \left(1 - \frac{D_b \mathrm{COS}\beta}{D_c}\right) \tag{27}$$

$$\mathrm{BFF} = \frac{f_r}{2} \frac{D_c}{D_b} \left[1 - \left(\frac{D_b \mathrm{COS}\beta}{D_c}\right)^2\right] \tag{28}$$

F_r, N_b, D_c, D_b, and β correspond to the frequency of rotation, rolling element number, pitch diameter, ball diameter, and angle of contact, respectively.

5.1. Case 1: Diagnosis of the Inner Race Fault

In this case, the vibration signal emanates from the inner race fault. The shaft speed is 1772 rpm, the load is 1hp, and the fault size is 0.007 inches. According to Equation (26), the calculated fault characteristic frequency for the inner race is 159.9 Hz. Taking 24,000 data points for analysis, I measured original bearing signal with an inner race fault signal is plotted in Figure 12a. The periodic impulses cannot be extracted due to the noise effect. From the envelope spectrum in Figure 12b, the fault characteristic *fi* and the first harmonic can be extracted. However, the other harmonics are surrounded by noise interference. Therefore, this signal requires pre-processing to improve fault detection.

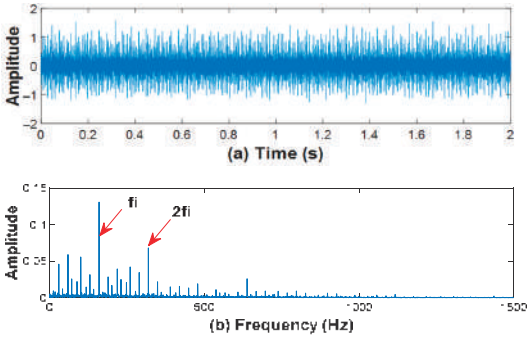

Figure 12. Experimental inner race defect: (**a**) waveform; (**b**) envelope spectrum.

5.1.1. Analysis of the Proposed Method

First, the proposed CMEEMD is used to extract the CMs from the experimental inner race fault signal. From the first six IMFs, fifteen combined modes (CMs) are generated using the method detailed in Section 3.1. The obtained IMFs are plotted in Figure 13, and the extracted CMs are illustrated in Figure 14. The next step is determining the most appropriate combination. By looking at the time domain waveform of each combination in Figure 14, it can be seen that the difference between the CMs is not significant. It is impossible to recognize directly which combination contains the most information about the fault. Therefore, the appropriate combination is selected using the proposed KMAD indicator. Based on Equation (25), Figure 15 illustrates the KMAD values of each combination. The combination $CM_{1\to2}$ has the highest value among all the other combinations, indicating that it is the best combination of the sensitive IMFs, including IMF1 and IMF2. Following this, the enhanced MED approach is executed on the selected combination. First, MED is used to minimize the entropy of $CM_{1\to2}$. After that, the output MED noise is minimized using the three-sigma rule. As illustrated in Figure 16a, the noise is restricted, and the fault impulses are highlighted. From the envelope spectrum in Figure 16b, we can extract the inner race fault characteristic frequency f_i and ten harmonics ($2f_i$, $3f_i$, $4f_i$, $5f_i$, $6f_i$, $7f_i$, $8f_i$, $9f_i$, $10f_i$, and $11f_i$). This suggests that the rolling bearing fault feature extraction method proposed in this paper is able to extract rich fault information.

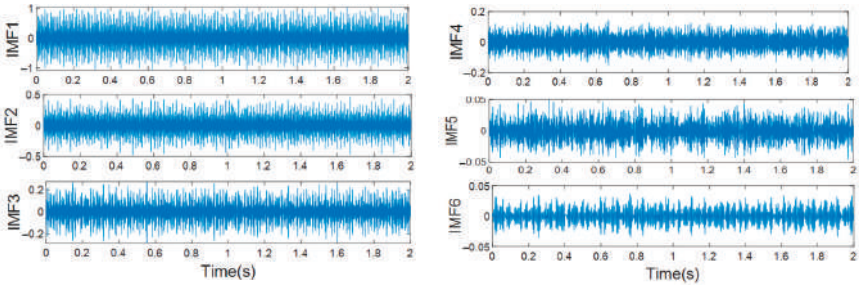

Figure 13. Decomposed result by EEMD.

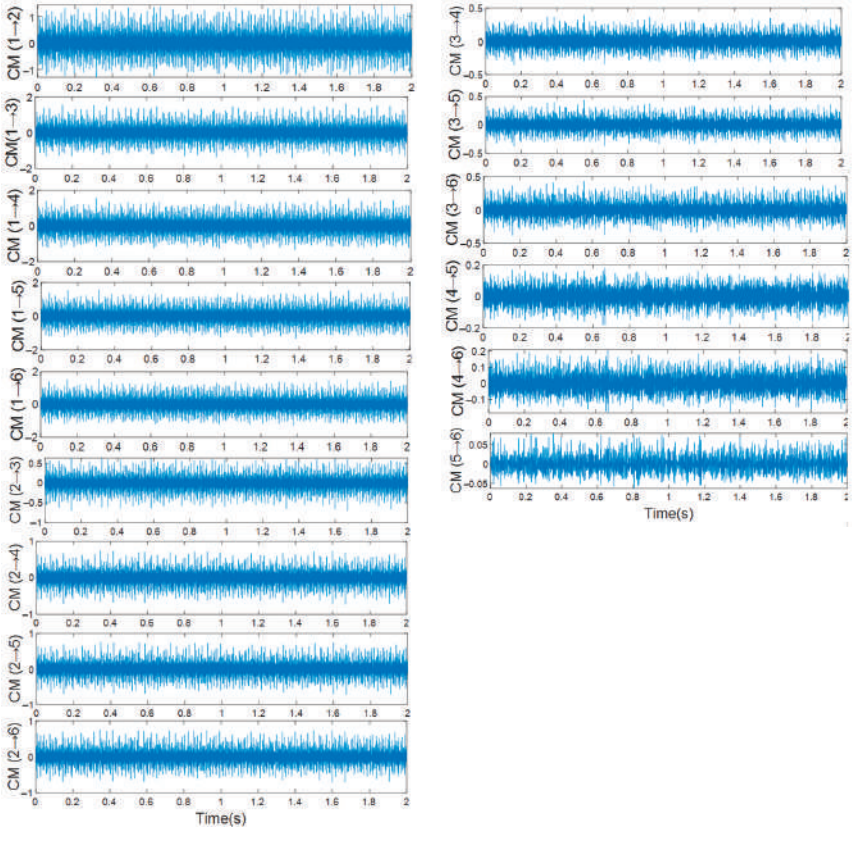

Figure 14. Extracted CMs result.

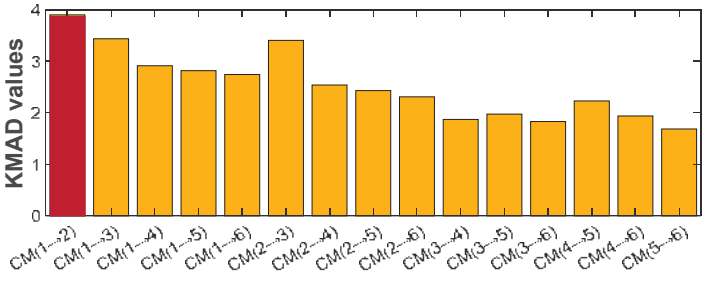

Figure 15. Sensitive CM selection using KMAD.

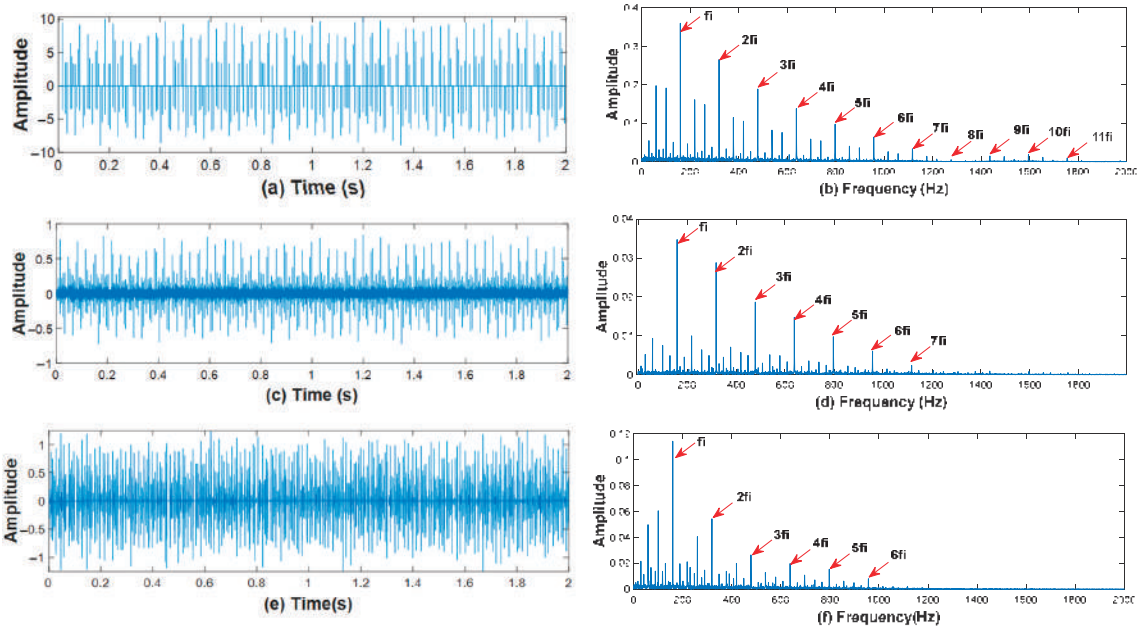

Figure 16. Inner race fault diagnosis results for processing the selected CM using: proposed method (**a**,**b**); conventional MED (**c**,**d**); and wavelet denoising (**e**,**f**).

5.1.2. Advantages of the Proposed Techniques for Inner Race Fault Diagnosis

Figure 16c,d shows the results of processing $CM_{1\to2}$ by the conventional MED. As shown in Figure 16c, the fault impulses are emphasized, and the noise level is reduced. However, it can be seen that some noise interference still exists. According to Figure 16a, noise interference has been reduced effectively. From the envelope spectrum in Figure 16d, we can distinguish only the inner race fault characteristic frequency f_i and six harmonics ($2f_i$, $3f_i$, $4f_i$, $5f_i$, $6f_i$, and $7f_i$). By comparing it with Figure 16b, it is clear that we can get more fault information. The comparison results show that the enhanced MED performs better than the MED in improving defect detection. To show the enhanced MED approach's superiority in eliminating noise, the wavelet de-noised method is performed on the selected combination $CM_{1\to2}$. As shown in Figure 16e, although the noise is reduced, the fault impulses are not highlighted as in Figure 16a. In addition, the extracted fault frequency and its harmonics in Figure 16f are not as excellent as those in Figure 16b. In this case, it can be said that the inability of the wavelet de-noising method to reduce noise effectively makes it difficult to extract rich fault information from the combination $CM_{1\to2}$. The comparison results demonstrate that the enhanced MED performs better than the wavelet de-noising method in eliminating noise. The amplitudes of the inter-harmonics shown in Figure 16b,d,f are much smaller than those shown in Figure 9b,d,f, respectively. This is due to the fact that a signal with high noise ($\sigma^2 = 0.7^2$) is created in the simulation. This makes it more difficult to eliminate noise interference in the simulated signal than in the experimental signal. As a result, the amplitude of the noise interference will mix with the inter-harmonics. To illustrate the advantages of the KMAD selection indicator, this paper conducted a comparison with the IMF selection method using kurtosis. Table 2 shows the kurtosis values of the first six IMFs. It is evident that IMF2 has the highest value among all the decomposition results, so it is selected as the sensitive IMF. IMF2 was processed using the enhanced MED approach. From the envelope spectrum of Figure 17a, it is clear that the extracted fault information is less than the extracted fault information in Figure 17b. This shows that the combination $CM_{1\to2}$ holds rich fault feature information.

The KMAD indicator selected $CM_{1\to2}$ as an appropriate combination of suitable IMFs, namely IMF1 and IMF2. As a result, if we take only IMF2, the information in IMF1 will be lost. This demonstrates that utilizing the KMAD selection indicator to select the appropriate combination overcomes the disadvantage of using kurtosis to choose the sensitive IMF and guarantees no information about the fault is lost.

Table 2. Kurtosis values of each IMF for Inner Race Fault Diagnosis.

IMF	Kurtosis
IMF1	4.6903
IMF2	4.7682
IMF3	4.3248
IMF4	3.0268
IMF5	2.5395
IMF6	2.6651

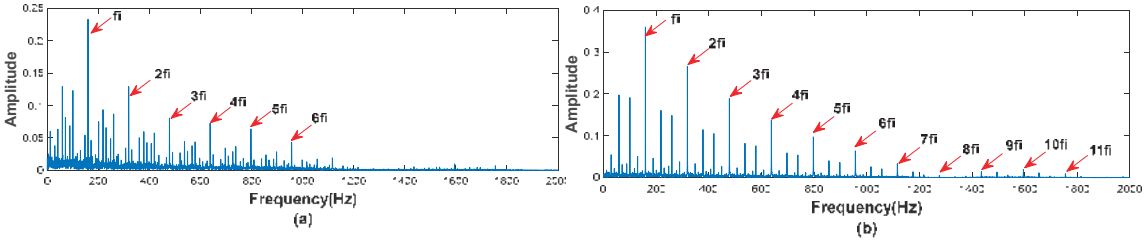

Figure 17. Diagnosis results using: (**a**) sensitive IMF-based Kurtosis; (**b**) sensitive CM-based KMAD.

5.2. Case 2: Diagnosis of the Outer Race Fault

The vibration signal in this case is caused by an outer race fault, with the shaft rotating at 1797 rpm and no load applied. The size of the fault is 0.021 inches, and the calculated fault characteristic frequency is 107.01 Hz. Taking 24,000 data points for analysis, Figure 18a shows the measured bearing signal with an outer race fault. It can be seen that the noise prevents the periodic impulses from being extracted. From the envelope spectrum in Figure 18b, although the fault characteristic frequency f_o and the first harmonic $2f_o$ can be extracted, the remaining harmonics are shrouded in noise interference. Therefore, this fault signal necessitates pre-processing to improve fault detection.

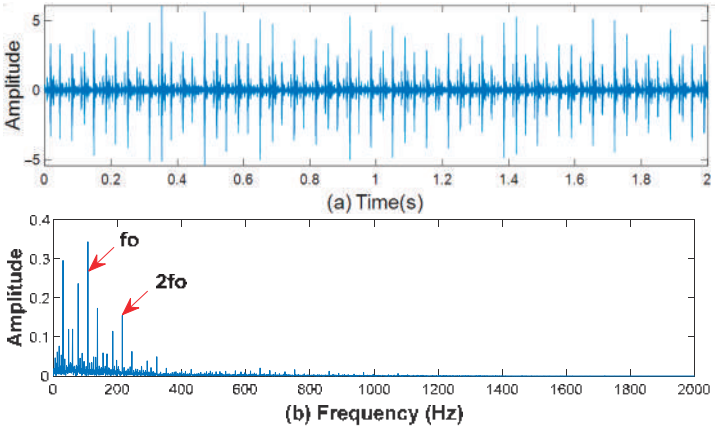

Figure 18. Experimental outer race defect: (**a**) waveform; (**b**) envelope spectrum.

5.2.1. Analysis of the Proposed Method

In the first step, CMEEMD extracts the CMs from the experimental outer race fault signal. Using the CMs extraction technique described in Section 3.1, fifteen CMs are created from the first six IMFs. Figure 19 shows the resulting IMFs, and Figure 20 shows the extracted CMs. The next step is to determine which combination is the most sensitive. The time-domain waveforms of each combination in Figure 20 show that there is no noticeable difference between the CMs. It is impossible to directly recognize the combination that combines only the useful IMFs. As a result, the suggested KMAD indicator is used to identify the appropriate combination. Figure 21 shows the KMAD values for each combination. The combination $CM_{1\to2}$ has the highest value. This indicates that it is a combination of sensitive IMFs, i.e., IMF1 and IMF2. Following that, the combination $CM_{1\to2}$ was processed using the enhanced MED approach. First, MED highlights the fault impulses of $CM_{1\to2}$. Then, the MED output is treated to the de-noised method derived from the three-sigma rule. As shown in Figure 22a, the noise is minimized, and the fault impulses are prominent. From the envelope spectrum in Figure 22b, we can accurately extract the outer race fault characteristic frequency f_o and nine harmonics ($2f_o$, $3f_o$, $4f_o$, $5f_o$, $6f_o$, $7f_o$, $8f_o$, $9f_o$, and $10f_o$). This implies that the proposed method for bearing fault feature extraction can effectively extract rich fault information.

5.2.2. Advantages of the Proposed Techniques for Outer Race Fault Diagnosis

The results of processing $CM_{1\to2}$ by MED are shown in Figure 22c,d. As seen in Figure 22c, the noise level is decreased, and the fault impulses are accentuated. However, there still exists noise interference. Compared to Figure 22a, noise interference has been significantly reduced. Analyzing the envelope spectrum in Figure 22d, it can be seen that we can extract less fault information than we can in Figure 22b. It is evident from the comparison results that the enhanced MED is more effective in improving fault detection compared to the MED. The wavelet de-noising method is performed on the selected combination, and the results are shown in Figure 22e,f. Although the noise has been reduced to a certain extent in Figure 22e, the extracted fault frequency and its harmonics in Figure 22f are less accurate than those extracted in Figure 22b. In this case, the inability of the wavelet de-noising to successfully decrease noise prevents the extraction of rich fault information from the combination $CM_{1\to2}$. The results of the comparison confirm that the proposed enhanced MED eliminates noise better than the wavelet de-noising method. To show the advantages of the CM selection method using KMAD, this paper performs a comparison with the IMF selection method using kurtosis. The kurtosis values for the first six IMFs are presented in Table 3. It appears that IMF2 has the highest value, so it is selected as a sensitive IMF. Next, IMF2 was treated using the enhanced MED approach. Based on the envelope spectrum of Figure 23a, we can extract only the outer race fault characteristic frequency f_o and three harmonics ($2f_o$, $3f_o$, $4f_o$). By comparing it with Figure 23b, it is clear that we can extract more fault information (f_o, $2f_o$, $3f_o$, $4f_o$, $5f_o$, $6f_o$, $7f_o$, $8f_o$, $9f_o$, and $10f_o$). This indicates that the selected combination contains rich defect information. The KMAD indicator identified $CM_{1\to2}$ as an appropriate combination of suitable IMFs, i.e., IMF1 and IMF2. Therefore, if we only select IMF2, the fault information in IMF1 will be wasted. This demonstrates that selecting the appropriate combination using the proposed indicator overcomes the disadvantage of the IMF selection using kurtosis to assure that no defect information is wasted.

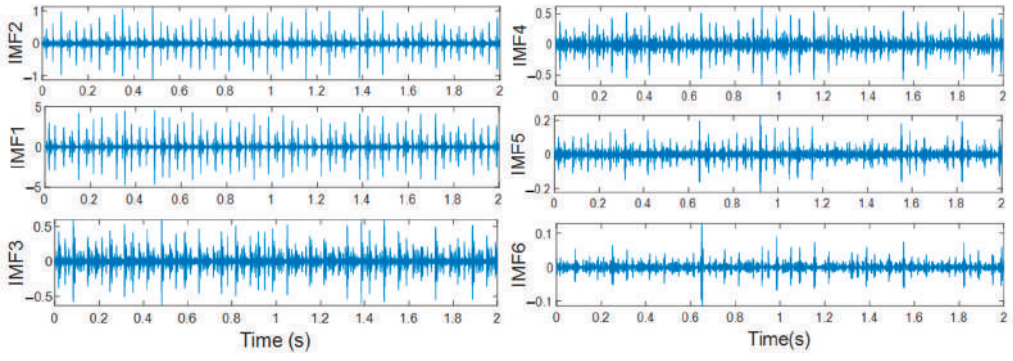

Figure 19. Decomposed result by EEMD.

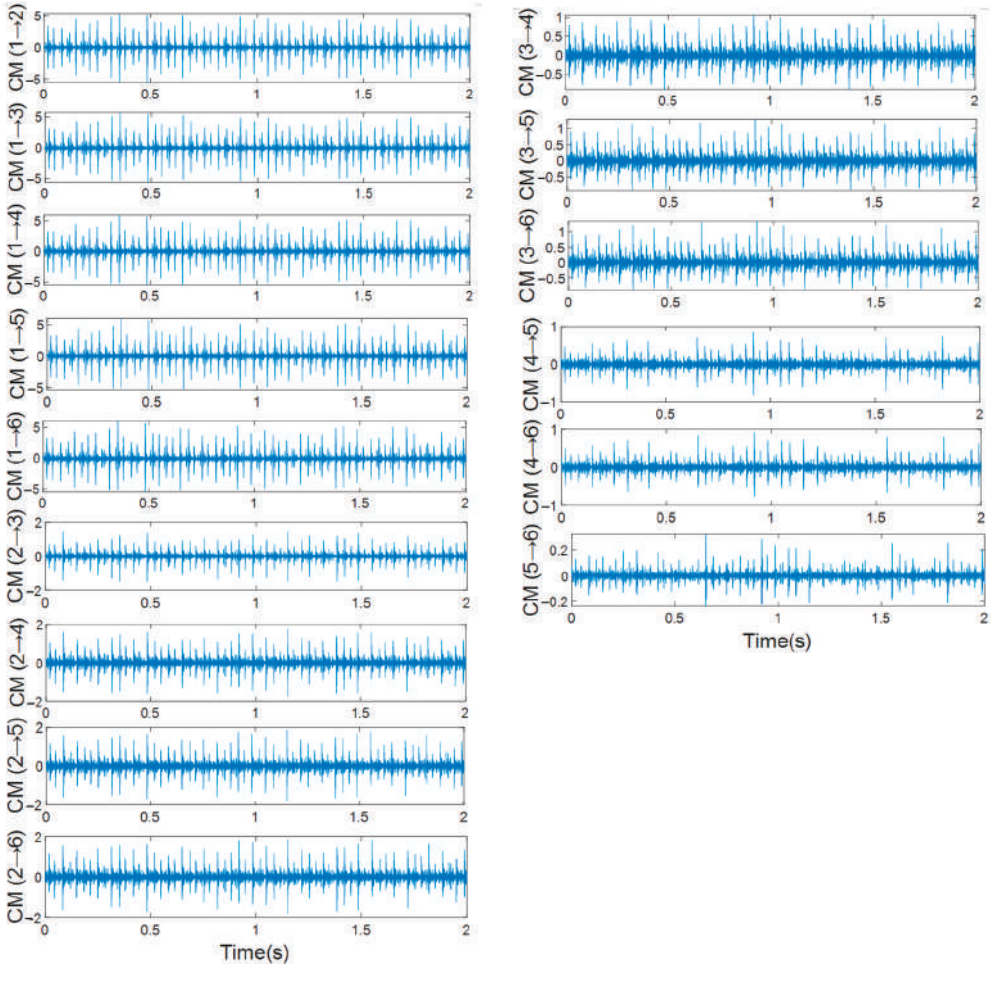

Figure 20. Extracted CMs result.

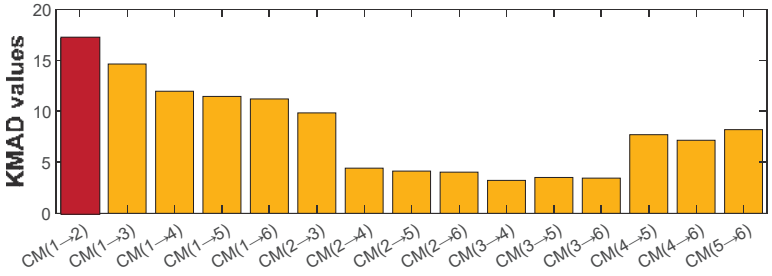

Figure 21. Sensitive CM selection using KMAD.

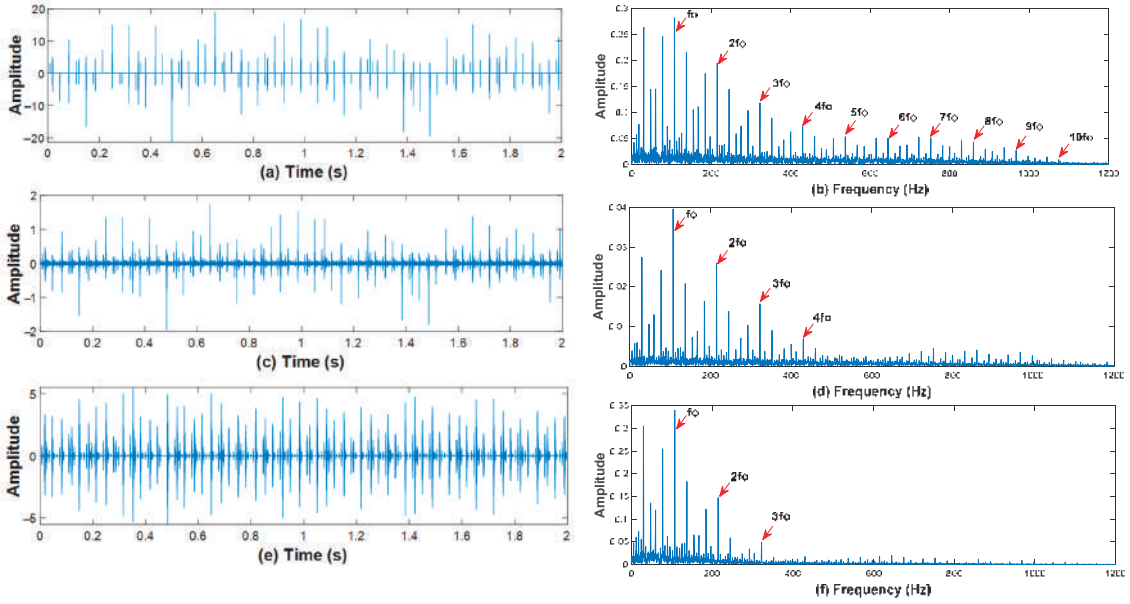

Figure 22. Outer race fault diagnosis results for processing the selected CM using: proposed method (**a**,**b**); conventional MED (**c**,**d**); and wavelet denoising (**e**,**f**).

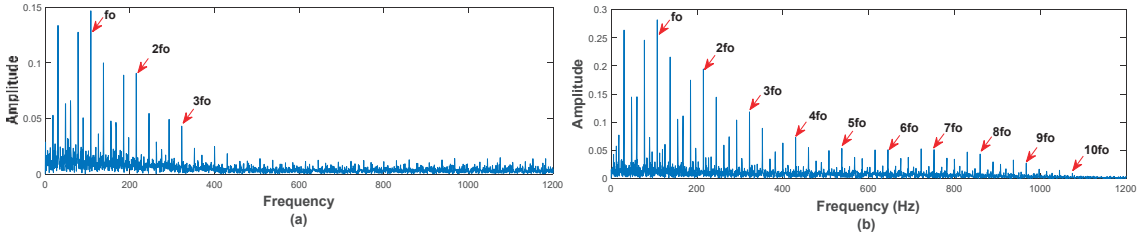

Figure 23. Diagnosis results using: (**a**) sensitive IMF-based Kurtosis; (**b**) sensitive CM-based KMAD.

Table 3. Kurtosis values of each IMF for Outer Race Fault Diagnosis.

IMF	Kurtosis
IMF1	17.7045
IMF2	25.1902
IMF3	10.6024
IMF4	8.8478
IMF5	10.0602
IMF6	11.0606

5.3. Case 3: Diagnosis of the Ball Bearing Fault

The ball race fault in this case generates the vibration signal. The shaft speed is 1772 rpm, the load is 1 hp, and the fault size is 0.028 inches. The calculated fault characteristic frequency for the ball race is 139.18 Hz based on Equation (28). Analyzing 24,000 data points, the bearing signal with a ball race fault is shown in Figure 24a. Due to the noise, it is difficult to distinguish the impact characteristics. From the envelope spectrum in Figure 24b, although the fault characteristic frequency f_b can be distinguished, its harmonics are masked by noise interference. To improve fault detection, this fault signal requires a pre-processing step.

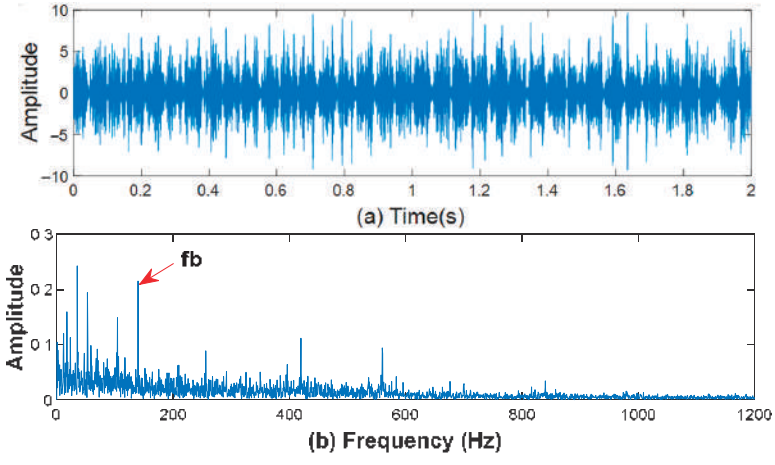

Figure 24. Experimental ball bearing defect: (**a**) waveform; (**b**) envelope spectrum.

5.3.1. Analysis of the Proposed Method

First, CMEEMD extracts the CMs of adjoining modes resulting from the decomposition of the ball defect vibration signal. The first six IMFs produce fifteen CMs using the CMs extraction technique described in Section 3.1. The obtained IMFs are shown in Figure 25, and the extracted CMs are shown in Figure 26. Identifying the most sensitive combination is the next step. According to Figure 26, there is no noticeable difference between the CMs based on their time-domain waveforms. Directly identifying the combination of useful IMFs is impossible. Therefore, the suggested KMAD indicator is used to identify the appropriate combination. According to Figure 27, the combination $CM_{1\to2}$ has the highest KMAD value. Accordingly, it indicates that it combines sensitive IMFs, i.e., IMF1 and IMF2. The combination $CM_{1\to2}$ was then performed using the enhanced deconvolution approach presented here. The noise is reduced considerably as shown in Figure 28a, and rich fault information (f_b, $2f_b$, $3f_b$, $4f_b$, $5f_b$, $6f_b$, $7f_b$, $8f_b$, and $9f_b$) can be extracted from the envelope spectrum presented in Figure 28b. This suggests that the proposed strategy can greatly enhance fault identification. Additionally, this demonstrates the validity of the proposed strategy for bearing fault feature extraction.

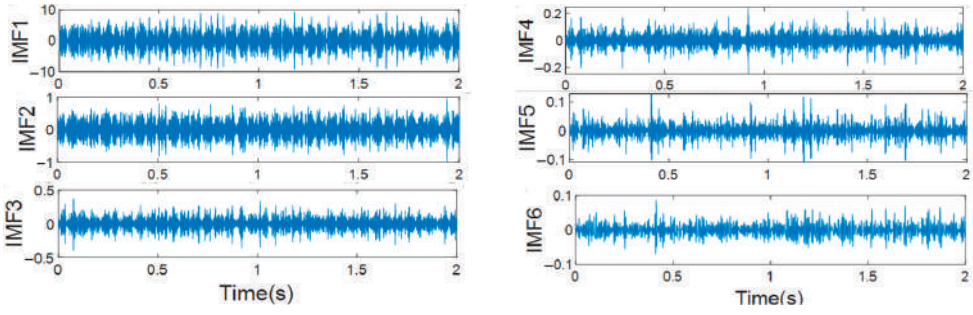

Figure 25. Decomposed result by EEMD.

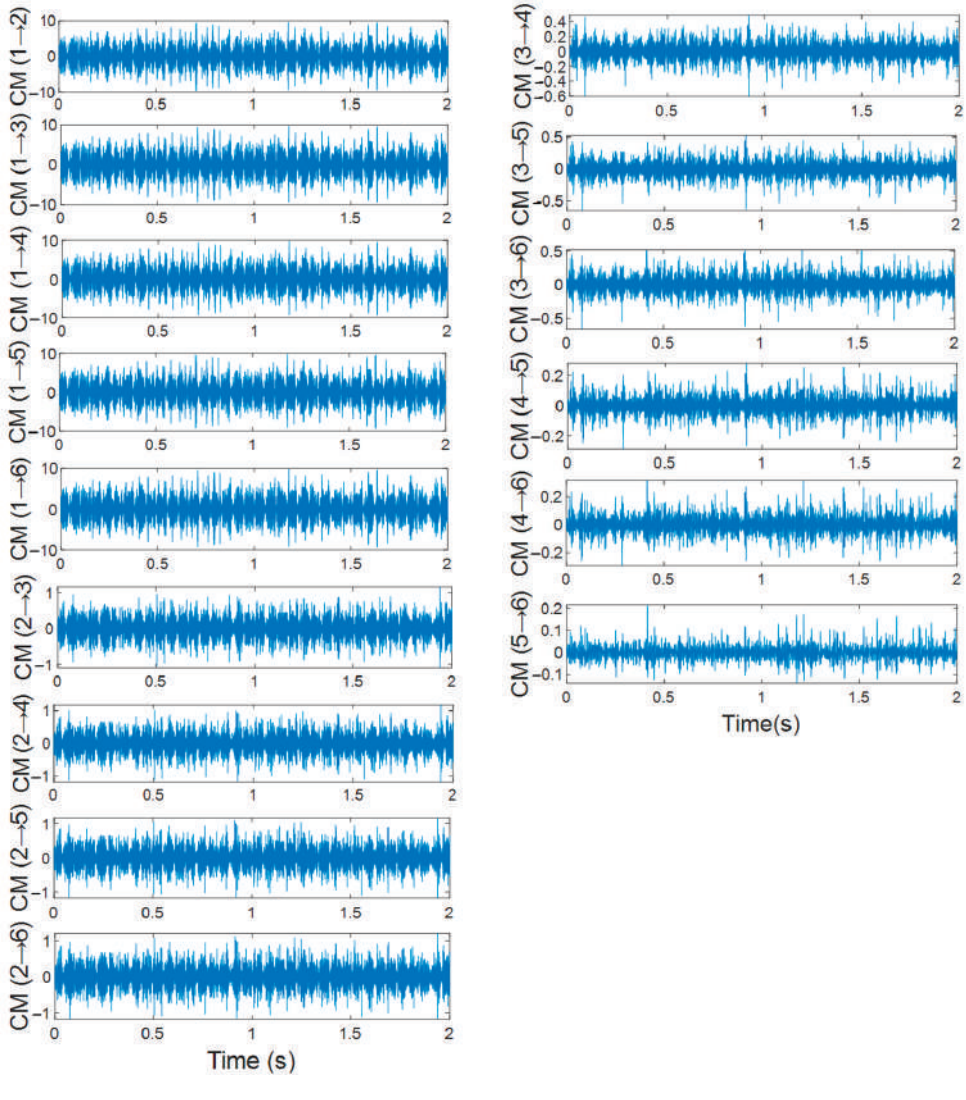

Figure 26. Extracted CMs result.

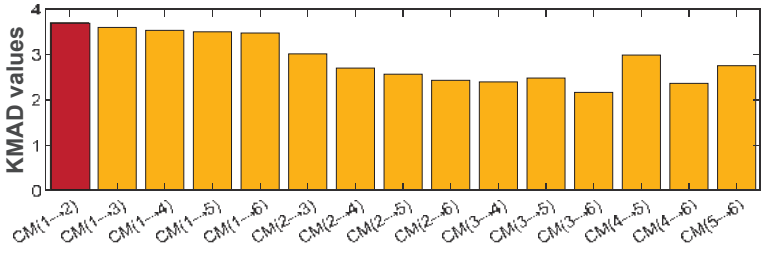

Figure 27. Effective CM selection based on KMAD.

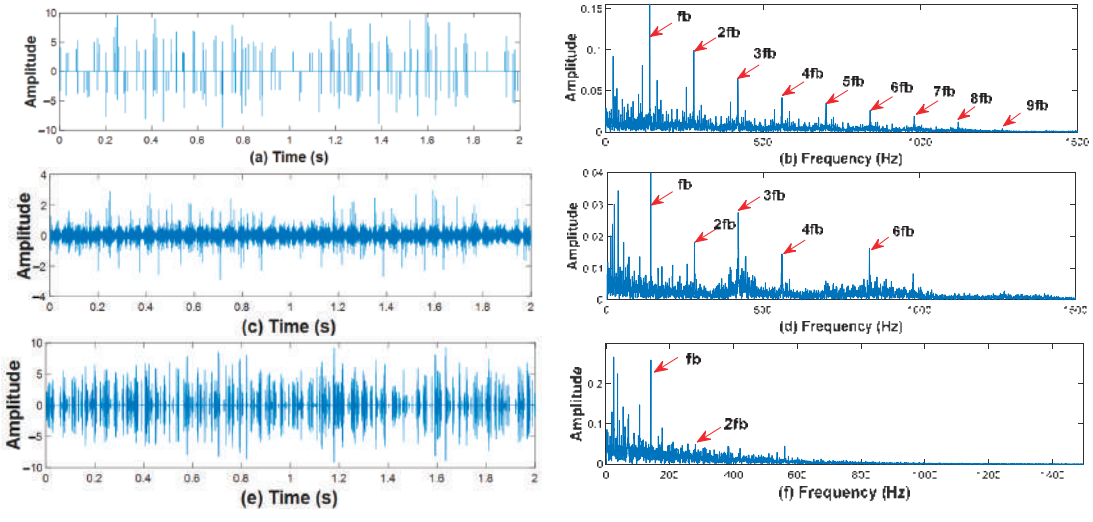

Figure 28. Ball fault diagnosis results for processing the selected CM using: proposed method (**a**,**b**); conventional MED (**c**,**d**); and wavelet denoising (**e**,**f**).

5.3.2. Advantages of the Proposed Techniques for Ball Bearing Fault Diagnosis

Figure 28c,d shows the results of processing the combination $CM_{1\to2}$ by the MED. As shown in Figure 28c, despite the noise level reduction, noise interference is still present. Compared to Figure 28a, the noise interference has been successfully minimized. Based on the envelope spectrum in Figure 28d, we can distinguish only the characteristic frequency of the ball race fault f_b and five harmonics ($2f_b$, $3f_b$, $4f_b$, $6f_b$, $7f_b$). Comparing it with Figure 28b, it is clear that the fault frequency with its multiplication components are extracted perfectly. It is evident from the results of the comparison that the enhanced MED is better than the MED for improving fault detection. The wavelet de-noised method is performed on the selected combination, and the results are shown in Figure 28e,f. Although the noise has been reduced to a certain extent in Figure 28e, the envelope spectrum presented in Figure 28f shows that we can distinguish only the characteristic frequency f_b and the first harmonic, whereas Figure 28b shows that we can perfectly extract fault information (f_b, $2f_b$, $3f_b$, $4f_b$, $5f_b$, $6f_b$, $7f_b$, $8f_b$, and $9f_b$). In this case, the inability of the wavelet de-noising approach to successfully decrease noise prevents the extraction of rich fault information from the combination $CM_{1\to2}$. It is evident from the comparison results that the enhanced MED suppresses noise more effectively than the wavelet de-noising technique. As an illustration of the advantages of the proposed CM selection method, we have compared it to the IMF selection method using maximum kurtosis. From Table 4, it can be seen that IMF5 has the highest value, so it is selected as a sensitive IMF. This IMF was processed using the proposed enhanced MED, and the envelope spectrum is shown in Figure 29a.

It is clear that no information about the defect can be extracted. This is due to the fact that the use of maximum kurtosis to select the sensitive IMF failed in this case, while the envelope spectrum in Figure 29b illustrated rich fault information. This is because the KMAD indicator proposed here succeeds in selecting the combination of valuable IMFs and proves its superiority for choosing the appropriate combination of useful IMFs.

Table 4. Kurtosis values of each IMF.

IMF	Kurtosis
IMF1	3.9782
IMF2	3.6592
IMF3	4.4182
IMF4	4.4670
IMF5	5.0951
IMF6	3.5202

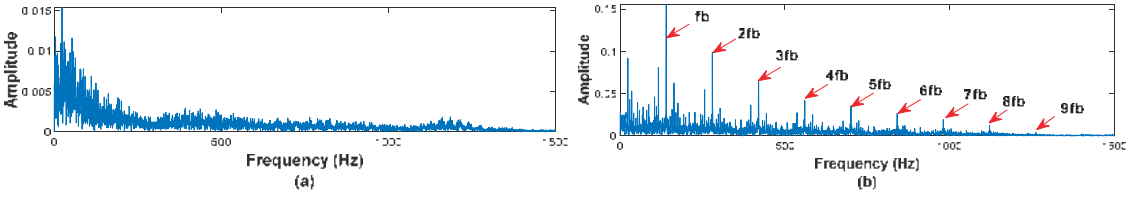

Figure 29. Diagnosis results using: (**a**) sensitive IMF-based kurtosis; (**b**) sensitive CM-based KMAD.

6. Conclusions

A novel rolling bearing fault feature extraction method is presented here, composed of the following proposed ideas: CMEEMD, the KMAD selection indicator, and an enhanced deconvolution approach. Firstly, the proposed CMEEMD extracts all the CMs from the original bearing vibration signal. A selection indicator named KMAD is proposed to identify the appropriate combination of suitable IMFs. This step aims to directly obtain a signal containing the most characteristic information about the fault, without going through the IMFs selection and reconstruction processes, and guaranteeing that no defect information is lost. Secondly, due to the effect of background noise, it is difficult to obtain rich fault information. Therefore, the proposed enhanced MED is performed on the selected combination. The principle of the enhanced MED is to minimize the noise of the MED output to obtain better analysis results. The selection method used in this paper has been applied to several other bearing vibration signals. From these experimental data, we found that the selected combination is most often $CM_{1\to2}$; however, in rare cases it can also be $CM_{1\to3}$ and $CM_{2\to3}$. On the other hand, several researchers confirm that the bearing defect information is included in the first IMFs. This supports and confirms the validity of the presented method.

The analysis of the simulated signal (presented in Section 4) and experimental rolling bearing cases (inner race, outer race, and ball race presented in Section 5) leads to the following results being concluded:

1. Compared to the MED technique, the enhanced MED presented in this paper is more robust in revealing defect pulses (taking Figure 9 as an example).
2. Comparison with the wavelet de-noising method demonstrated that the enhanced MED performs well with noise suppression and is more effective in revealing fault information (taking Figure 28 as an example).
3. Compared results between the sensitive IMF using maximum kurtosis and the sensitive CM using the proposed KMAD indicate that the CM selected contains rich fault feature information (taking Figure 17 as an example).

4. CMEEMD and KMAD proposed herein solves the drawback of the IMF selection method by using the maximum kurtosis value to ensure that no information about the defect is wasted (taking Figure 23 as an example).
5. In contrast to the conventional IMF selection method that failed to identify the appropriate IMF for the ball defect, the KMAD indicator was successful in selecting the appropriate combination of useful IMFs (see Figure 29).
6. The analysis of simulated and experimental rolling bearing signals confirms that the proposed strategy for bearing fault diagnosis can greatly enhance fault detection and effectively extract rich fault information (taking Figures 9 and 28 as examples).

Author Contributions: Conceptualization, Y.D.; methodology, Y.D., N.B., R.P., A.C.M., R.R. and S.S.; validation, Y.D., N.B. and A.C.M.; resources, Y.D., N.B. and A.C.M.; writing—original draft preparation, Y.D., N.B., A.C.M., R.R., R.P. and S.S.; writing—review and editing, Y.D., N.B., R.P., A.C.M., R.R. and S.S; visualization, Y.D., A.C.M., R.R., N.B., R.P. and N.B.; supervision, Y.D., R.R., R.P., N.B., A.C.M. and S.S.; paper submitting, R.P., R.R., N.B. and Y.D. All authors have read and agreed to the published version of the manuscript.

Funding: This research received no external funding.

Data Availability Statement: Not applicable.

Conflicts of Interest: The authors declare no conflict of interest.

References

1. Deekshit Kompella, K.C.; Venu Gopala Rao, M.; Srinivasa Rao, R. Bearing fault detection in a 3 phase induction motor using stator current frequency spectral subtraction with various wavelet decomposition techniques. *Ain Shams Eng. J.* **2018**, *9*, 2427–2439. [CrossRef]
2. Kumar, P.S.; Kumaraswamidhas, L.A.; Laha, S.K. Selecting effective intrinsic mode functions of empirical mode decomposition and variational mode decomposition using dynamic time warping algorithm for Rolling Element Bearing Fault diagnosis. *Trans. Inst. Meas. Control* **2018**, *41*, 1923–1932. [CrossRef]
3. Chen, L.; Xu, G.; Zhang, S.; Yan, W.; Wu, Q. Health indicator construction of machinery based on end-to-end trainable convolution recurrent neural networks. *J. Manuf. Syst.* **2020**, *54*, 1–11. [CrossRef]
4. Huang, N.E.; Shen, Z.; Long, S.R.; Wu, M.C.; Shih, H.H.; Zheng, Q.; Yen, N.-C.; Tung, C.C.; Liu, H.H. The empirical mode decomposition and the Hilbert spectrum for nonlinear and non-stationary time series analysis. *Proc. R. Soc. Lond. Ser. A Math. Phys. Eng. Sci.* **1998**, *454*, 903–995. [CrossRef]
5. Zheng, J.; Huang, S.; Pan, H.; Jiang, K. An improved empirical wavelet transform and refined composite multiscale dispersion entropy-based fault diagnosis method for rolling bearing. *IEEE Access* **2020**, *8*, 168732–168742. [CrossRef]
6. Wu, Z.; Huang, N. Ensemble empirical mode decomposition: A noise-assisted data analysis method. *Adv. Adapt. Data Anal.* **2009**, *1*, 1–41. [CrossRef]
7. Lei, Y.; Lin, J.; He, Z.; Zuo, M.J. A review on empirical mode decomposition in fault diagnosis of rotating machinery. *Mech. Syst. Signal Process.* **2013**, *35*, 108–126. [CrossRef]
8. Wang, H.; Chen, J.; Dong, G. Feature extraction of rolling bearing's early weak fault based on EEMD and tunable Q-factor wavelet transform. *Mech. Syst. Signal Process.* **2014**, *48*, 103–119. [CrossRef]
9. Yang, F.; Kou, Z.; Wu, J.; Li, T. Application of mutual information-sample entropy based Med-ICEEMDAN de-noising scheme for weak fault diagnosis of hoist bearing. *Entropy* **2018**, *20*, 667. [CrossRef]
10. Li, J.; Tong, Y.; Guan, L.; Wu, S.; Li, D. A UV-visible absorption spectrum denoising method based on EEMD and an improved universal threshold filter. *RSC Adv.* **2018**, *8*, 8558–8568. [CrossRef]
11. Ricci, R.; Pennacchi, P. Diagnostics of gear faults based on EMD and automatic selection of intrinsic mode functions. *Mech. Syst. Signal Process.* **2011**, *25*, 821–838. [CrossRef]
12. Li, Z.; Shi, B. Research of fault diagnosis based on sensitive intrinsic mode function selection of EEMD and Adaptive Stochastic Resonance. *Shock Vib.* **2016**, *2016*, 2841249. [CrossRef]
13. Ma, J.; Wu, J.; Wang, X. Incipient fault feature extraction of rolling bearings based on the MVMD and teager energy operator. *ISA Trans.* **2018**, *80*, 297–311. [CrossRef]
14. Luo, C.; Jia, M.P.; Wen, Y. The Diagnosis Approach for Rolling Bearing Fault Based on Kurtosis Criterion EMD and Hilbert Envelope Spectrum. In Proceedings of the 2017 IEEE 3rd Information Technology and Mechatronics Engineering Conference (ITOEC), Chongqing, China, 3–5 October 2017.
15. Damine, Y.; Megherbi, A.C.; Sbaa, S.; Bessous, N. Study of the IMF Selection Methods Using Kurtosis Parameter for Bearing Fault Diagnosis. In Proceedings of the 2022 IEEE 19th International Multi-Conference on Systems, Signals & Devices (SSD), Setif, Algeria, 6–10 May 2022.

16. Pennacchi, P.; Ricci, R.; Chatterton, S.; Borghesani, P. Effectiveness of med for fault diagnosis in roller bearings. *Springer Proc. Phys.* **2011**, *139*, 637–642. [CrossRef]
17. Chatterton, S.; Ricci, R.; Pennacchi, P.; Borghesani, P. Signal Processing Diagnostic Tool for rolling element bearings using EMD and Med. *Lect. Notes Mech. Eng.* **2013**, 379–388. [CrossRef]
18. Ding, J.; Huang, L.; Xiao, D.; Jiang, L. A fault feature extraction method for rolling bearing based on intrinsic time-scale decomposition and AR minimum entropy deconvolution. *Shock Vib.* **2021**, *2021*, 1–19. [CrossRef]
19. Zhao, H.; Min, F.; Zhu, W. Test-cost-sensitive attribute reduction of data with normal distribution measurement errors. *Math. Probl. Eng.* **2013**, *2013*, 6673965. [CrossRef]
20. Fang, K.; Zhang, H.; Qi, H.; Dai, Y. Comparison of EMD and EEMD in Rolling Bearing Fault Signal Analysis. In Proceedings of the 2018 IEEE International Instrumentation and Measurement Technology Conference (I2MTC), Houston, TX, USA, 14–17 May 2018.
21. Wiggins, R.A. Minimum entropy deconvolution. *Geoexploration* **1978**, *16*, 21–35. [CrossRef]
22. González, G.; Badra, R.E.; Medina, R.; Regidor, J. Period estimation using minimum entropy deconvolution (MED). *Signal Process.* **1995**, *41*, 91–100. [CrossRef]
23. Sawalhi, N.; Randall, R.B.; Endo, H. The enhancement of fault detection and diagnosis in rolling element bearings using minimum entropy deconvolution combined with spectral kurtosis. *Mech. Syst. Signal Process.* **2007**, *21*, 2616–2633. [CrossRef]
24. Shojae Chaeikar, S.; Manaf, A.A.; Alarood, A.A.; Zamani, M. PFW: Polygonal fuzzy weighted—An SVM kernel for the classification of overlapping data groups. *Electronics* **2020**, *9*, 615. [CrossRef]
25. Qin, B.; Luo, Q.; Zhang, J.; Li, Z.; Qin, Y. Fault frequency identification of rolling bearing using reinforced ensemble local mean decomposition. *J. Control Sci. Eng.* **2021**, *2021*, 2744193. [CrossRef]
26. Wang, H.-D.; Deng, S.-E.; Yang, J.-X.; Liao, H. A fault diagnosis method for rolling element bearing (REB) based on reducing Reb Foundation vibration and noise-assisted vibration signal analysis. *Proc. Inst. Mech. Eng. Part C J. Mech. Eng. Sci.* **2018**, *233*, 2574–2587. [CrossRef]
27. Zhen, D.; Guo, J.; Xu, Y.; Zhang, H.; Gu, F. A novel fault detection method for rolling bearings based on non-stationary vibration signature analysis. *Sensors* **2019**, *19*, 3994. [CrossRef] [PubMed]
28. Dibaj, A.; Hassannejad, R.; Ettefagh, M.M.; Ehghaghi, M.B. Incipient fault diagnosis of bearings based on parameter-optimized VMD and Envelope Spectrum Weighted Kurtosis index with a new sensitivity assessment threshold. *ISA Trans.* **2021**, *114*, 413–433. [CrossRef]
29. Chen, J.; Yu, D.; Yang, Y. The application of energy operator demodulation approach based on EMD in machinery fault diagnosis. *Mech. Syst. Signal Process.* **2007**, *21*, 668–677. [CrossRef]
30. Yang, Y.; Yu, D.; Cheng, J. A fault diagnosis approach for roller bearing based on IMF envelope spectrum and SVM. *Measurement* **2007**, *40*, 943–950. [CrossRef]
31. Cheng, Y.; Wang, Z.; Chen, B.; Zhang, W.; Huang, G. An improved complementary ensemble empirical mode decomposition with adaptive noise and its application to rolling element bearing fault diagnosis. *ISA Trans.* **2019**, *91*, 218–234. [CrossRef]
32. Sun, Y.; Yu, J. Fault detection of rolling bearing using sparse representation-based adjacent signal difference. *IEEE Trans. Instrum. Meas.* **2021**, *70*, 1–16. [CrossRef]
33. Liu, T.; Chen, J.; Dong, G.; Xiao, W.; Zhou, X. The fault detection and diagnosis in rolling element bearings using frequency band entropy. *Proc. Inst. Mech. Eng. Part C J. Mech. Eng. Sci.* **2012**, *227*, 87–99. [CrossRef]
34. Download a Data File: Case School of Engineering: Case Western Reserve University. Available online: https://engineering.case.edu/bearingdatacenter/download-data-file (accessed on 24 October 2020).
35. Saruhan, H.; Sandemir, S.; Çiçek, A.; Uygur, I. Vibration analysis of rolling element bearings defects. *J. Appl. Res. Technol.* **2014**, *12*, 384–395. [CrossRef]

energies

MDPI

Article

Analytical Modeling, Analysis and Diagnosis of External Rotor PMSM with Stator Winding Unbalance Fault

Ahmed Belkhadir [1,2], Remus Pusca [1], Driss Belkhayat [2], Raphaël Romary [1,*] and Youssef Zidani [2]

[1] Univ. Artois, UR 4025, Laboratoire Systèmes Electrotechniques et Environnement (LSEE), F-62400 Béthune, France
[2] Univ. Cadi Ayyad, P.O. Box 549, Laboratoire des Systèmes Electriques, Efficacité Energétique et Télécommunications (LSEEET), Faculty of Sciences and Technologies, Marrakech 40000, Morocco
* Correspondence: raphael.romary@univ-artois.fr

Abstract: Multiple factors and consequences may lead to a stator winding fault in an external rotor permanent magnet synchronous motor that can unleash a complete system shutdown and impair performance and motor reliability. This type of fault causes disturbances in operation if it is not recognized and detected in time, since it might lead to catastrophic consequences. In particular, an external rotor permanent magnet synchronous motor has disadvantages in terms of fault tolerance. Consequently, the distribution of the air-gap flux density will no longer be uniform, producing fault harmonics. However, a crucial step of diagnosis and controlling the system condition is to develop an accurate model of the machine with a lack of turns in the stator winding. This paper presents an analytical model of the stator winding unbalance fault represented by lack of turns. Here, mathematical approaches are used by introducing a stator winding parameter for the analytical modeling of the faulty machine. This model can be employed to determine the various quantities of the machine under different fault levels, including the magnetomotive force, the flux density in the air-gap, the flux generated by the stator winding, the stator inductances, and the electromagnetic torque. On this basis, a corresponding link between the fault level and its signature is established. The feasibility and efficiency of the analytical approach are validated by finite element analysis and experimental implementation.

Keywords: stator winding unbalance fault; external rotor permanent magnet synchronous motor; fault harmonics; diagnosis; lack of turns; analytical approach; finite element analysis

Citation: Belkhadir, A.; Pusca, R.; Belkhayat, D.; Romary, R.; Zidani, Y. Analytical Modeling, Analysis and Diagnosis of External Rotor PMSM with Stator Winding Unbalance Fault. *Energies* **2023**, *16*, 3198. https://doi.org/10.3390/en16073198

Academic Editors: Moussa Boukhnifer and Larbi Djilali

Received: 3 March 2023
Revised: 25 March 2023
Accepted: 28 March 2023
Published: 1 April 2023

1. Introduction

In recent years, external rotor permanent magnet synchronous motors (ER-PMSMs) mounted directly in the wheels of vehicles has been one of the trends in drive systems employed in hybrid and electrical vehicle (HEV) powertrains. The design of this type of motor presents a challenge, as it must be characterized by high durability and energy efficiency [1–3].

Interest in continually developing techniques for the diagnosis of faults in electrical machines is related to several factors. Firstly, the overall number of embedded motors that are employed in different applications, such as industrial systems, renewable energy generating systems, and HEVs [4]. However, owing to the ageing of materials, manufacturing faults, or sever conditions, various types of electrical, mechanical, and magnetic faults can occur in the machine [5], for example: open phase faults, interturn short circuit faults, lack of turns (LTs) faults in the stator winding, eccentricity, demagnetization, and magnetic circuit faults [6]. Hence, the integration of detection strategies, diagnosis, and fault-tolerant control becomes unavoidable. Moreover, during the real operation of the ER-PMSM, LTs faults may emerge due to manufacturing tolerances or ageing issues. Therefore, once the LTs fault appears, the stator current increases to generate enough torque, which leads to

torque and speed ripples, and further exacerbates thermal problems. As a result, early diagnosis of the LTs fault is critical for preventing deterioration of ER-PMSM performance and reducing eventual losses by implementing the most effective corrective measures. These measures may consist of repairing the faulty machine or, in certain situations, appropriately reconfiguring the control strategy [6].

Currently, several studies have been conducted on the diagnosis and localization of stator winding faults in ER-PMSMs. Modeling and experiments have been used as the first step in these studies, and research aims to extract electrical signals and quantities such as voltage and currents, mechanical quantities such as speed, torque and vibration, and magnetic field signals such as magnetic flux and density [7–9]. Secondly, appropriate signal processing methods were employed to extract fault characteristics from various signals, identify the mode, assess the severity, and classify the fault [10,11].

The lack of turns (LTs) faults can be detected via different approaches based on signals, data, and models. The first technique aims to identify characteristic fault frequencies in measured ER-PMSM signals [12,13], which are processed using time-frequency signal analysis tools, such as the Fourier transform [14,15], wavelet transforms [16], and the Hilbert–Huang transform [17]. Unlike the Fourier transform, the drawback of wavelets and Hilbert–Huang transforms is their incompatibility with real-time analysis. Additionally, a detection technique using an analysis of the external field, provided by sensors positioned around the machine, using information fusion methods is proposed in [18–21], but these methods require an accurate knowledge of the external stray flux.

Advanced machine learning method are also employed to detect ER-PMSM stator faults. These methods are attractive due to their advanced data processing capabilities combined with external machine signals, such as vibration, acoustic noise, and torque [22]. A one-dimensional convolutional neural network model, which analyzes torque and current signals to diagnose the motor across a wide range of speeds, variable loads, and fault levels, is proposed in [23]. These kinds of advanced algorithms are very efficient, but they require a large amount of computation and historical data to form models and classify localized defects, as well as extremely high hardware requirements.

This research focuses on the diagnosis of LTs faults in ER-PMSMs by examining and analyzing the current and speed spectrum, allowing a simple and powerful implementation of an online fault diagnosis approach. To better understand the influence and consequences of the fault, an analytical approach and finite element model validation were employed. The finite element analysis (FEA) offers the benefits of a well-established application and high computational precision and accuracy. The analytical approach involves the development of a mathematical model that replicates the behavior of the machine in the presence of the fault. This model can be used to predict the impact of the fault on various machine quantities, and can contribute to the development of effective fault diagnosis methods. Overall, the combination of the analytical approach and FEA validation provides comprehensive knowledge of the impact of the LTs fault on ER-PMSMs employed in electric mobility.

The main contributions of this research are as follows: a novel technique and approach for modeling LTs faults in ER-PMSMs. The suggested analytical model requires less computational time and can subsequently provide an accurate reference for real-time fault diagnosis, accuracy, and maintenance. Then, the experimental validation for an ER-PMSM operating in the case of a motor is presented. Experimental measurements that must be taken to ensure a reliable diagnosis are also presented.

The main structure of this paper is as follows: in Section 2, the healthy and faulty analytical models are established to examine how the LTs fault impacts the various electrical and mechanical quantities of the machine, and the FEA is used to verify the effectiveness and accuracy of the proposed analytical model. The experimental setup is provided in Section 3, and the experimental results are in Section 4. Finally, Section 5 summarizes the conclusions and prospects of the presented work.

2. Exhaustive Analysis of LTs Fault

After evoking the secondary consequences at the origin of the stator winding unbalance fault illustrated by LTs, this section aims to provide a global comprehension of the machine in healthy and faulty conditions using an analytical approach and numerical validation.

The development of a mathematical model enabling simulation of the behavior of the ER-PMSM in the two healthy and faulty operating modes is indicated below. This model is based on a 2D extension of the winding function approach to determine the different inductances of the machine, taking into consideration all the space harmonics, the real geometry of the ER-PMSM, as well as the distribution of the windings in the stator slots. The model of the 24 slots and 22 poles of the ER-PMSM with concentric winding is shown in Figure 1. The major specifications of the machine are listed in Table 1.

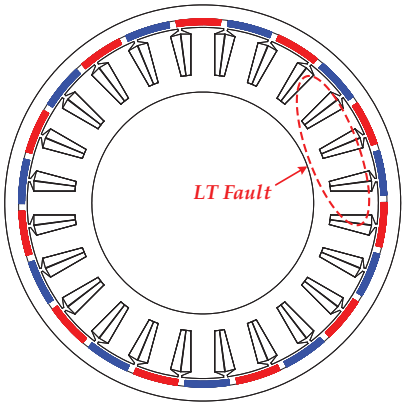

Figure 1. The model of the double-layer fractional-slot concentrated-wound ER-PMSM.

Table 1. ER-PMSM parameters.

Parameter	Symbol	Value	Parameter	Symbol	Value
Rated power (kW)	P	1.5	Inner rotor diameter (mm)	–	183
Rated speed (rpm)	w	600	Length (mm)	L_{axe}	35
DC bus voltage (V)	V_{DC}	150	Air-gap length (mm)	g	1.365
Rated current (A_{RMS})	I_N	11	Stator slot width (mm)	${l_e}^s$	10.37
Rated torque (Nm)	Γ_e	24	Stator tooth width (mm)	${l_d}^s$	21.1431
Number of poles	p	22	Stator fictive slot depth (mm)	p^s	2.0740
Number of phases	m	3	Slot opening width (mm)		2
Number of slots	N^s	24	Magnet thickness (mm)	h_m	3
Number of turns per coil	N_T	22	Residual flux density of PM (T)	B_r	1.26
Outer stator diameter (mm)	–	112	Magnet-arc to pole-pitch ratio (%)	α_p	85.55
Inner stator radius (mm)	R_s	88.6350	Permanent magnets	–	NdFeB N38SH
Outer rotor diameter (mm)	–	186	Magnetic steel	–	M530-50A

The analytical model is developed based on the assumptions given throughout this section, as follow [24]:

(1) Magnetic saturation is negligible;
(2) Ideal ferromagnetic steel and the magnetic energy is concentrated in the air-gap;
(3) Small air-gap relative to the internal diameter of the stator and radial magnetic field (tangential magnetic fields are negligible);
(4) Neglected conductivity and eddy current effects.

2.1. Analytical Approach

2.1.1. Distribution Function of the ER-PMSM

The distribution function of a coil placed in the magnetic circuit delivers information about its position. Therefore, the objective is to apply the winding function approach to compute the inductances of the 24 slots and 22 poles of a double-layer fractional-slot concentrated-wound (FSCW) ER-PMSM (24/22) [24]. Their waveforms are shown in Figure 2.

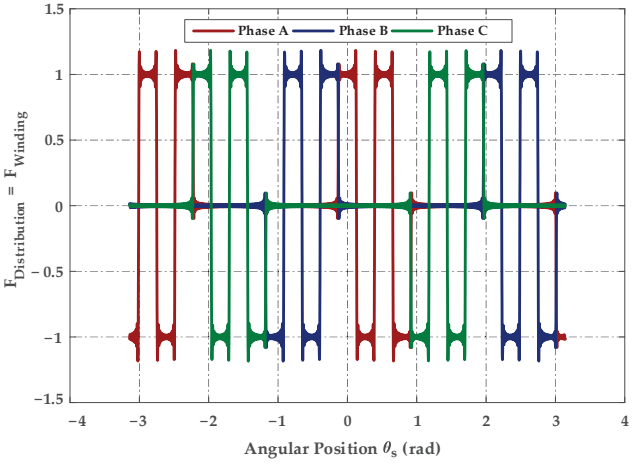

Figure 2. Distribution function of ER-PMSM.

The Fourier decomposition of the distribution function can be given by:

$$F_{distribution} = \frac{P_e}{2\pi} O_c + \frac{2}{\pi} \sum_{h=1}^{+\infty} \frac{1}{h} \sin\left(hP_e \frac{O_c}{2}\right) \cos(hP_e\theta_s) \quad (1)$$

The total distribution function of a winding is the sum of the distribution functions of a winding, and the sum of the distribution functions of the coils in a series of the same phase per pair of poles of this winding.

$$F_{distribution,T}(\theta_s) = \sum_{i=1}^{q} F_{distribution}(\theta_s) \quad (2)$$

where P_e is the winding periodicity, O_c is the coil opening angle, q is the coil number, and θ_s is the angular position in relation to the stator reference axis.

2.1.2. Winding Function of the ER-PMSM

The winding function presents the magnetomotive force (MMF) of a single-turn winding carrying a unit current. We may represent these functions as a series of harmonics due to the winding's periodicity and each phase coil's function, which contains periodic square pulses. In this analysis instance, the mean value of the distribution function is null. However, Figure 2 illustrates the winding function, which is proportional to the distribution function.

$$F_w(\theta_s) = F_{distribution,T}(\theta_s) - \langle F_{distribution,T}(\theta_s) \rangle \quad (3)$$

The spatial harmonic amplitudes of the winding function, obtained from Equation (3), for a stator with concentrated winding around a double-layer tooth is illustrated in Figure 3.

Evidently, the harmonic of rank h = 11 had the highest amplitude of 0.4396 for a machine (24/22).

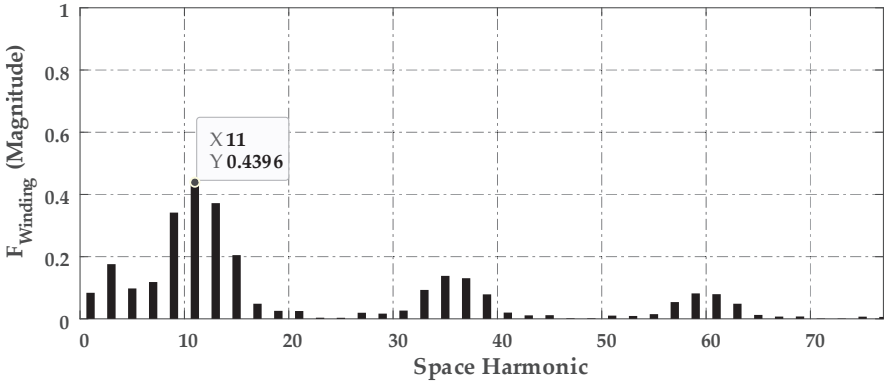

Figure 3. Harmonic spectrum of the winding function.

2.1.3. Winding Factor of the ER-PMSM

The winding factor presents the efficiency of the coil arrangement to create a MMF and determines the capacity of the electromagnetic torque production. We can write a general presentation of the total winding factor K_w of harmonic h, using the voltage phasor diagram [25]:

$$K_w = K_d K_p \tag{4}$$

where K_d is the distribution factor, K_p is the pitch factor, $\alpha_u = p\frac{2\pi}{Q}$ is the slot angle, m is the number of phases, $Q = 2qpm$ is the number of slots, $\tau_p = \frac{\pi D}{2p}$ is the pole pitch, and D is the diameter of the air-gap.

$$K_d = \frac{\sin\left(h\frac{q\alpha_u}{2}\right)}{q\sin\left(h\frac{\alpha_u}{2}\right)} = \frac{\sin\left(h\frac{Q}{2pm}\frac{2\pi p}{2Q}\right)}{q\sin\left(h\frac{2\pi p}{2q2pm}\right)} = \frac{\sin\left(h\frac{\pi}{6}\right)}{q\sin\left(h\frac{\pi}{6q}\right)} \tag{5}$$

$$K_p = \sin\left(h\frac{O_c}{\tau_p}\frac{\pi}{2}\right) \tag{6}$$

According to Figure 4, the spectrum represents the spatial distribution of the winding factor. The maximum torque of the machine generated in the air-gap will be created by the h11 component, with a winding factor of 0.949. This component corresponds to the fundamental, with a rank $h = p$.

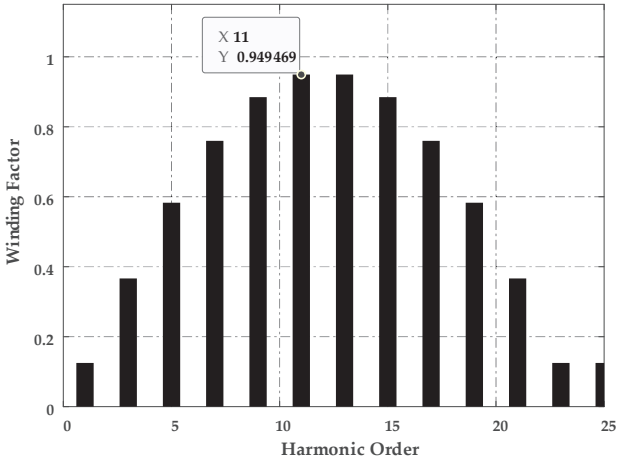

Figure 4. Harmonic spectrum of the winding factor.

2.1.4. Magnetomotive Force (MMF)

A. Healthy MMF of the ER-PMSM

The MMF of a double-layer FSCW stator is rich in harmonics. However, this harmonic content leads to torque ripples, unbalanced saturation, and iron losses [26,27]. For this reason, the combination of slots and number of poles has specific features that must be examined and studied before that the machine is designed. The harmonics of the winding factor (Figure 4) are frequently employed as an indication of the properties of this combination [28].

The spatial MMF distribution of a phase winding is obtained by superimposing the MMF of all its coils. Due to the periodicity of the winding, the healthy MMF of each phase j includes periodic square pulses, and can be represented by a Fourier series decomposition, as follows:

$$\varepsilon_j^s(t,\theta_s) = K_w N_T i_j^s(t) F_w(\theta_s) \tag{7}$$

where N_T is the turns number and $i_j^s(t) = \sqrt{2} I_j^s \sin(\omega t + \varphi_j)$ is the temporal expression of sinusoidal current.

The total healthy MMF generated by the 22 pole, 24 slot FSCW stator is determined using the following formula:

$$\varepsilon^s(t,\theta_s) = \sum_{j=1}^{m} \left(\varepsilon_j^s(t,\theta_s) \right) \tag{8}$$

$$\varepsilon^s(t,\theta_s) = \frac{1}{\pi} m I_{\max} N_T \sum_{h=1}^{+\infty} \frac{1}{h} K_w \sin\left(h P_e \frac{O_c}{2} \right) \cos(h P_e \theta_s - (\omega t - \varphi)) \tag{9}$$

The distribution of the total healthy MMF of the three-phase stator winding is shown in Figure 5 when it is supplied with a balanced three-phase current of f = 110 Hz. The harmonic spectrum of the total MMF distribution in the healthy case is determined from Equations (8) and (9), and illustrated in Figure 6. We notice that the harmonic of rank h11 is the most dominating of ER-PMSM (24/22).

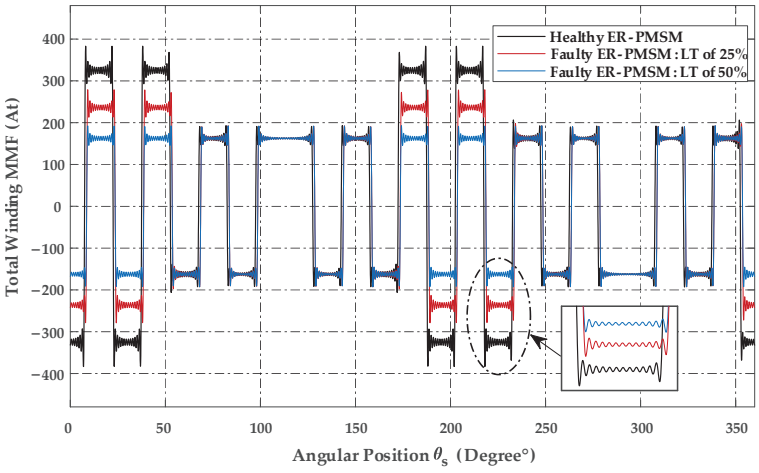

Figure 5. Healthy and faulty stator MMF distribution.

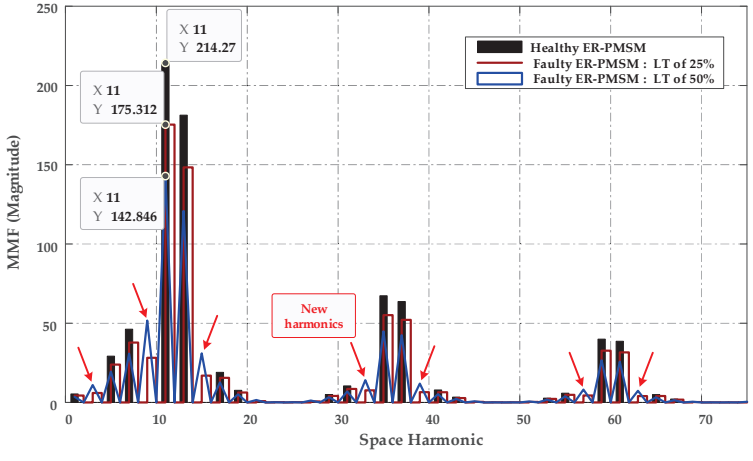

Figure 6. Spatial harmonic spectrum of the total healthy and faulty MMF.

B. Faulty MMF of the ER-PMSM

When a stator winding unbalanced fault of LTs occurs in the machine, the stator MMF will be impacted by the fault. The general analytic model of the faulty MMF is obtained using the previously stated methodologies and is shown in Figure 5, which can be represented by the following expressions:

$$\varepsilon^{s}_{j,faulty}(t,\theta_s) = K_w F_{w,faulty}(\theta_s) N_T i^{s}_{j}(t) \tag{10}$$

$$F_{w,faulty}(\theta_s) = \frac{N_f}{N_T} F_{w,a}(\theta_s) + F_{w,b}(\theta_s)\cos\left(\omega t - \frac{2\pi}{3}\right) + F_{w,c}(\theta_s)\cos\left(\omega t + \frac{2\pi}{3}\right) \tag{11}$$

$$\varepsilon^{s}_{faulty}(t,\theta_s) = \sum_{j=1}^{+\infty} \varepsilon^{s}_{j,faulty}(t,\theta_s) \tag{12}$$

The analytical modeling in the faulty state is performed for two fault levels: 25% and 50% LTs in phase A.

Where $F_{w,faulty}$ is the winding function in the faulty state, and N_f is the number of faulty stator turns.

A comparison between the harmonic content of the MMF is presented in Figure 6. Evidently, when the machine is subjected to the LTs fault, all of the odd harmonics are present in the spectrum, as well as the appearance of new harmonics that are due to the LTs fault levels (Red arrows).

2.1.5. Air-Gap Flux Density

The permeance function is proportional to the inverse of the air-gap thickness, and depends only on the average permeance of the air-gap and the form of the stator slots.

For determination of the air-gap permeance, a simplified geometry of the motor shown in Figure 7 is considered, with a fictitious model for the slots resulting from the assumptions for a nonsalient FSCW ER-PMSM, and with radial field lines.

$$\wp(\theta_s) = P_0 + \sum_{K_s=1}^{+\infty} P_{K_s} \cos(K_s N^s \theta_s) \tag{13}$$

$$P_0 = \frac{\mu_0}{g + p^s}\left(1 + \frac{p^s r_d^s}{g}\right) \tag{14}$$

$$P_{K_s} = 2\mu_0 \frac{p^s}{g(g + p^s)} \frac{\sin\left(K_s r_d^s \pi\right)}{K_s \pi} \tag{15}$$

where $\mu_0 = 4\pi 10^{-7}$ is the permeability of a vacuum approximately equal to that of the air, $p^s = l^e{}_s/5$ is the stator fictive slot depth [18], r_d^s is the stator toothing ratio, and K_s is the permeance rank.

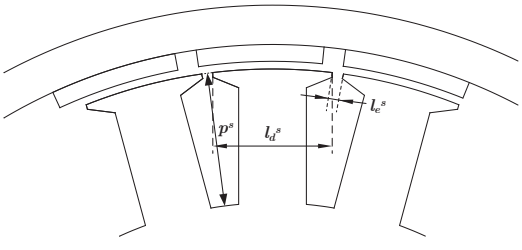

Figure 7. Geometry adopted for the stator slots of the ER-PMSM.

The healthy and faulty air-gap flux density for a sinusoidal current system can be written as the following expression:

$$b^s(t, \theta_s) = \wp(\theta_s)\varepsilon^s(t, \theta_s) \tag{16}$$

$$b^s_{faulty}(t, \theta_s) = \wp(\theta_s)\varepsilon^s_{faulty}(t, \theta_s) \tag{17}$$

Here, it is assumed that the magnetic field distribution would be affected in the fault condition. Depending on the two levels of the LTs fault, there is a reduction in the flux inside the stator core. Based on Figure 9, the magnitude of the flux density is considerably impacted by the fault. The spectrum of the flux density harmonic in the air-gap is depicted in Figure 10. The amplitude of the fundamental component in the healthy condition and no-load case is 0.0652 T.

2.1.6. Inductances in Healthy and Faulty FSCW ER-PMSMs

To be able to determine the different parameters of the machine in healthy and damaged modes for examining the structure of the ER-PMSM, it is crucial to calculate the

values of the self and mutual inductances. In order to examine several configurations, these calculations are performed using an analytical approach, as well as a numerical and experimental validation model.

Inductances have a crucial role in this modeling technique since they account for the many effects that might occur in the machine. Accurate modeling will lead to additional information of the signals, and a good compromise in terms of model accuracy.

The inductances of the machine will be determined analytically using the previously stated winding function.

A. Healthy Magnetic Flux

The magnetic flux produced by a phase *i* flowing through a phase *j* winding is provided by the following equations:

$$\Phi_{ji,h}(t) = N_T \iint b_i^s(t,\theta_s) ds j \tag{18}$$

$$\Phi_{ji,h}(t) = (N_T)^2 I_i(t) R_s L_{axe} K_w \int_0^{2\pi} F_{distribution,j}(\theta_s) \wp(\theta_s) F_{w,i}(\theta_s) d\theta_s \tag{19}$$

The self-magnetic flux of phase A is given by:

$$\Phi_{aa,h}(t) = \frac{2}{P_e} R_s L_{axe} (N_T)^2 \frac{2I_{\max}}{\pi} \wp(\theta_s) \sum_{h=1}^{+\infty} \left[\frac{1}{h^2} K_w \sin^2\left(hP_e \frac{O_c}{2} \right) \cos(\omega t - \varphi) \right] \tag{20}$$

The mutual magnetic flux between phase A and phase B can be expressed by:

$$\begin{array}{l} \Phi_{ab,h}(t) = \frac{2}{P_e} R_s L_{axe} (N_T)^2 \frac{2I_{\max}}{\pi} \wp(\theta_s) \\ \sum\limits_{h=1}^{+\infty} \left[\frac{1}{h^2} K_w \sin\left(hP_e \frac{O_c}{2} \right) \left(\sin\left(hP_e \frac{3O_c}{2} \right) - \sin\left(hP_e \frac{O_c}{2} \right) \right) \cos(\omega t - \varphi) \right] \end{array} \tag{21}$$

where R_s is the inner stator radius.

B. Faulty Magnetic Flux

The self-magnetic flux of phase A in the faulty state is given by:

$$\Phi_{a11,faulty}(t) = \frac{2}{P_e} R_s L_{axe} (N_f)^2 \frac{2I_{\max}}{\pi} \wp(\theta_s) \sum_{h=1}^{+\infty} \left[\frac{1}{h^2} K_w \sin^2\left(hP_e \frac{O_c}{2} \right) \cos(\omega t - \varphi) \right] \tag{22}$$

$$\begin{array}{l} \Phi_{a12,faulty}(t) = -\frac{1}{P_e} R_s L_{axe} (N_f)^2 \frac{2I_{\max}}{\pi} \wp(\theta_s) \\ \sum\limits_{h=1}^{+\infty} \left[\frac{1}{h^2} K_w \sin\left(hP_e \frac{O_c}{2} \right) \left(\sin\left(hP_e \frac{3O_c}{2} \right) - \sin\left(hP_e \frac{O_c}{2} \right) \right) \cos(\omega t - \varphi) \right] \end{array} \tag{23}$$

The total flux linkage of a phase winding is the sum of the aforementioned, as follows:

$$\Phi_{a,faulty}(t) = \sum_{n=1}^{8} \Phi_{an,faulty}(t) \tag{24}$$

A faulty mutual magnetic flux between phase A and phase b is given by:

$$\begin{array}{l} \Phi_{a1b8,faulty}(t) = \frac{1}{P_e} R_s L_{axe} N_T N_f \frac{2I_{\max}}{\pi} \wp(\theta_s) \\ \sum\limits_{h=1}^{+\infty} \left[\frac{1}{h^2} K_w \sin\left(hP_e \frac{O_c}{2} \right) \left(\sin\left(hP_e \frac{3O_c}{2} \right) - \sin\left(hP_e \frac{O_c}{2} \right) \right) \cos(\omega t - \varphi) \right] \end{array} \tag{25}$$

$$\begin{array}{l} \Phi_{a5b4,faulty}(t) = \frac{1}{P_e} R_s L_{axe} N_T N_f \frac{2I_{\max}}{\pi} \wp(\theta_s) \\ \sum\limits_{h=1}^{+\infty} \left[\frac{1}{h^2} K_w \sin\left(hP_e \frac{O_c}{2} \right) \left(\sin\left(hP_e \frac{3O_c}{2} \right) - \sin\left(hP_e \frac{O_c}{2} \right) \right) \cos(\omega t - \varphi) \right] \end{array} \tag{26}$$

$$\Phi_{ab,faulty}(t) = \Phi_{a1b8,faulty}(t) + \Phi_{a5b4,faulty}(t) \quad (27)$$

Figure 11 depicts the magnetic flux produced by the three phases with a fault of 25% and 50% of LTs of phase A.

C. Inductances in Healthy and Faulty States

The ER-PMSM inductances are calculated using the approach provided in [25,29], which uses the winding function corresponding to the MMF produced by the stator winding. Accordingly, the self or mutual inductances are determined from the following relation:

$$L_{ji,h} = (N_T)^2 R_s L_{axe} K_w \int_0^{2\pi} F_{distribution,j}(\theta_s) \wp(\theta_s) F_{w,i}(\theta_s) d\theta_s \quad (28)$$

According to the analytical modeling of the faulty magnetic flux proposed and calculated from Equations (25) and (28), the general form of the faulty self and mutual inductance can be expressed as follows:

$$L_{a-A25\%/50\%} = \frac{\Phi_{a,faulty}(t)}{I_a(t)}; \quad M_{a-A25\%/50\%-b} = \frac{\Phi_{ab,faulty}(t)}{I_a(t)} \quad (29)$$

where the faulty inductances depend on the severity of the LTs fault, and the number of faulty stator turns N_f. The analytical calculation of self and mutual inductances is conducted as an example to explain the complete procedure. The other inductances can be derived similarly. Figure 12a–c exhibit, respectively, the healthy and faulty inductances according to the two LTs fault levels. All of the results obtained for healthy and degraded operations by the analytical and numerical approaches are close.

An AC immobilization test is employed for the experimental measurement (Figure 12). In this method, an AC current flows in phase A, while the other two phases are in an open circuit. The self-inductance is then obtained using the RMS voltage and current measured at different rotor positions [30].

2.2. Numerical Validation: Finite Element Analysis

In order to evaluate and validate the analytical approach, a two-dimensional FEA-2D model of the motor is tested and simulated (Figure 1). The analysis of the behavior for the LTs fault, with consideration of the electrical and mechanical quantities of the machine in operational mode, is performed in an open-loop system. All of the testing and analysis will be focused on the intrinsic features of the LTs fault. The main structural parameters and specifications are listed in Table 1. Figure 8 illustrates the study ER-PMSM machine with faulted turns and the mesh of the FEA model.

The impact of the LTs fault is at first examined without the influence of the controllers under two fault severities. The ER-PMSM with 24 slots and 22 poles is used for the fault analysis. The following analyses are performed at a level of 25% and 50% of LTs in phase A of the machine.

Figure 8. ER-PMSM with LTs in phase A. (**a**) ER-PMSM stator winding with LTs fault in phase A; (**b**) the mesh of the ER-PMSM FEA analysis.

Performance Analysis of ER-PMSM with LTs Fault

Figure 9 illustrates the radial air-gap flux density at no load obtained by the analytical model and the FEA model in the healthy and faulty states according to the two LT fault levels. In the case of an unbalanced stator winding fault, the amplitudes of the no-load flux density waveforms drop. However, all analyses are consistent with the analytical analyses.

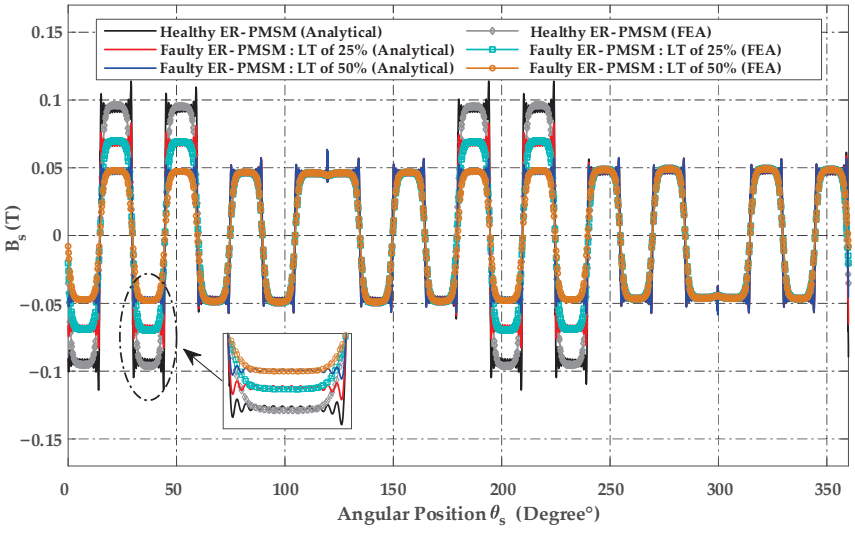

Figure 9. Air-gap flux density distribution in the healthy and faulty cases.

The harmonic spectrum is depicted in Figure 10. The flux density in healthy and faulty circumstances is mainly composed of the fundamental and other harmonics, as well as the appearance of new harmonics attributable to the faults (red arrows). In addition, the amplitude of the fundamental suffers a diminution in the faulty cases compared to the healthy condition.

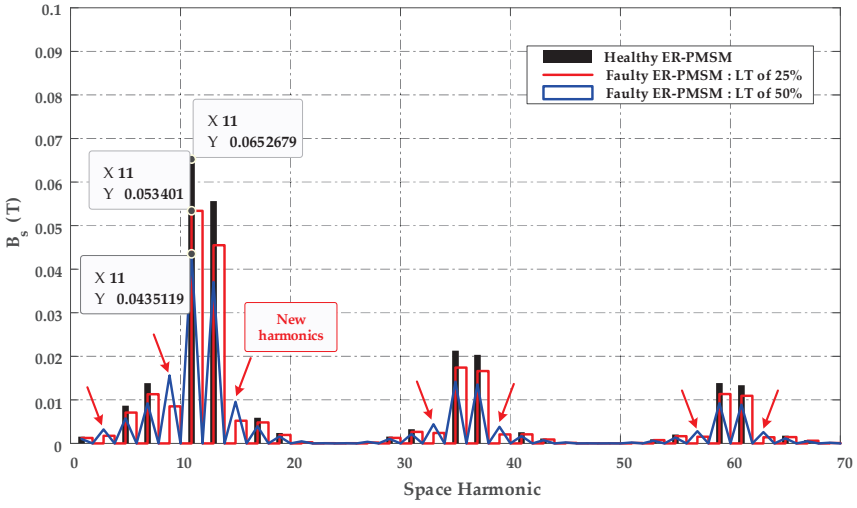

Figure 10. Spatial harmonic spectrum of the healthy and faulty air-gap flux density.

Figure 11 shows the total fluxes generated by the stator power supply in the two situations of the LTs fault of 25% and 50% of phase A, developed theoretically using the analytical model described previously, and the finite element method at a speed of 600 rpm. Due to the change in the stator winding induced by the fault in phase A, an unbalance arises depending on the level of the fault, which leads to torque ripples (Figure 13). This analysis will be used to determine the inductance of the machine in the presence of the fault. The inductances take a critical role in the modeling process, since they consider the many phenomena that might appear within the machine. Accurate modeling will lead to additional information of the signals and a good compromise in terms of the accuracy of the model.

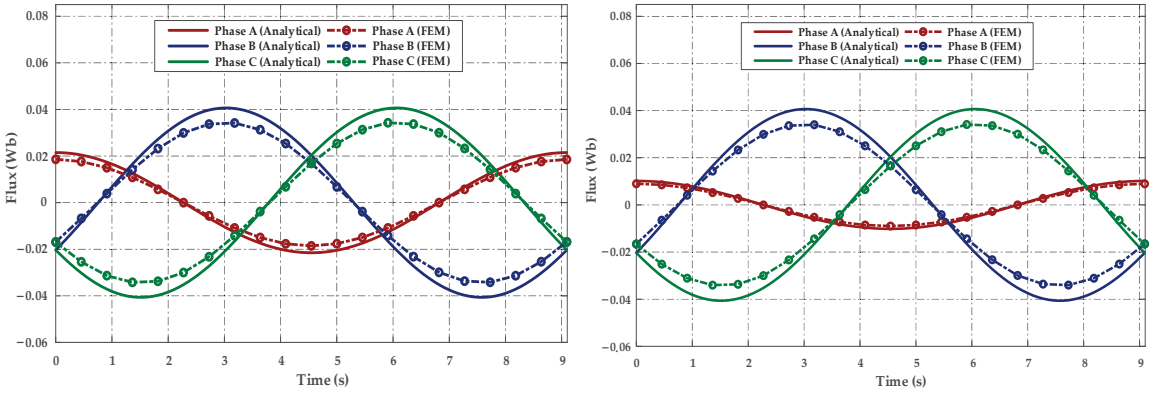

Figure 11. Total flux created by the stator winding, (**a**) Total flux with 25% of LTs fault; (**b**) total flux with 50% of LTs fault.

The inductances of the ER-PMSM are reported in Figure 12. The values given for the inductances, calculated using the winding function approach from the real distribution of windings in the stator slots, are closer to those of the finite element analysis and the experimental ones. On the other hand, a considerable discrepancy is noted between the FEA and analytical findings for the analytically calculated inductance. This discrepancy

can be associated with the inadequacy of the winding function to take into account the real flux paths, geometry, and nonuniformly saturated iron in an FSCW ER-PMSM machine.

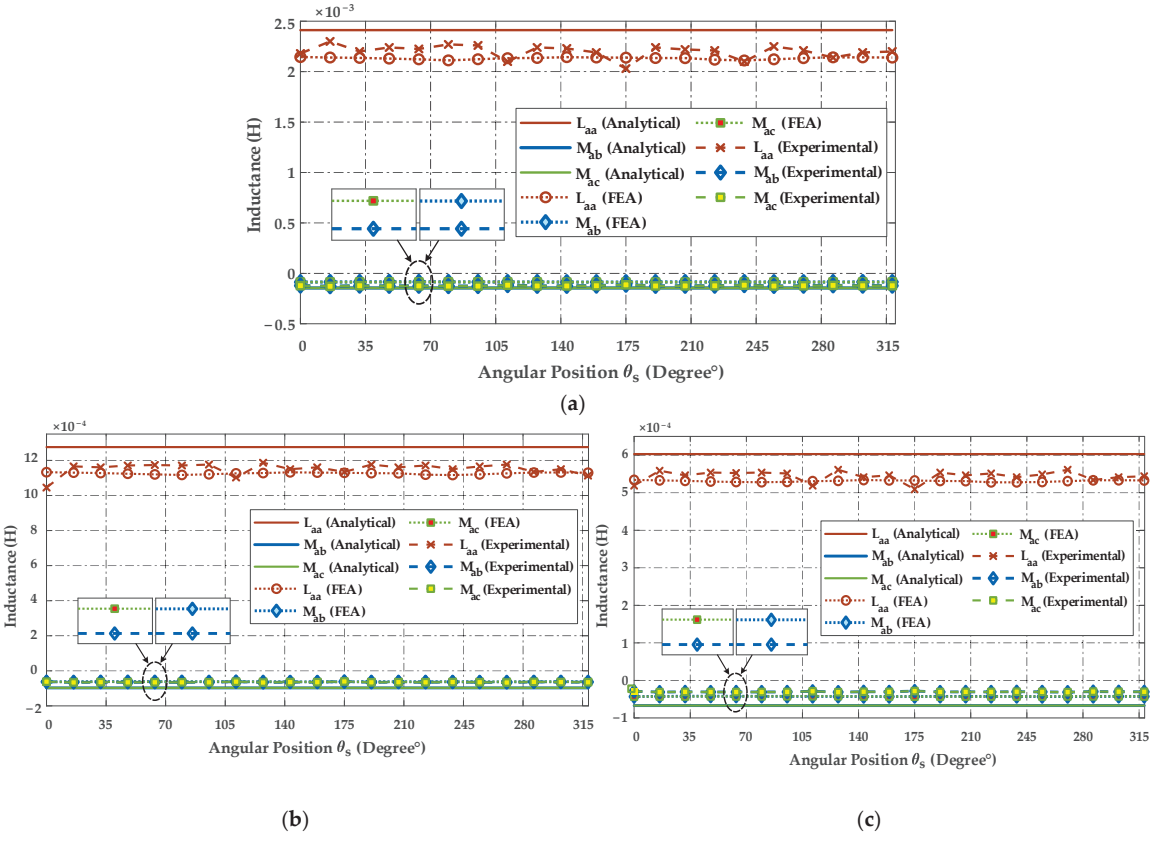

Figure 12. Comparison between inductances derived by the analytical approach, FEA, and experimental measurements. (**a**) Healthy inductances; (**b**) faulty inductances with 25% of LTs fault; (**c**) faulty inductances with 50% of LTs fault.

In Figure 13, the ER-PMSM is operated at nominal load. The temporal representation of the output torque of the machine by FEA for the three cases is provided. In the LTs fault circumstances of 25% and 50% of phase A, the torque decreases accordingly concerning the healthy state, according to the fault's severity level. Moreover, due to the change of its symmetry, torque ripples appear, which are due to the growth of harmonics. The evolution of the faulty torque reveals torque ripples corresponding to the double of the frequency, owing to the decrease of the resistance and the inductance of a phase, which makes the bandwidth wider. The results concerning the torque are provided in Table 2. It can be observed that the level of the torque ripples is related to the severity of the fault.

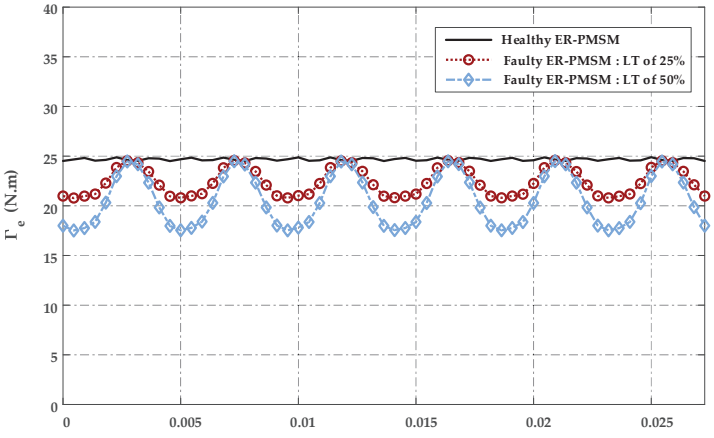

Figure 13. Electromagnetic torque comparison.

Table 2. Summary of simulation results of electromagnetic torque.

State	Torque Ripples (N·m)
Healthy ER-PMSM	$\begin{cases} \Gamma_{e-\min} = 24.5023 \\ \Gamma_{e-\max} = 24.8956 \end{cases}$
Faulty state: LTs of 25%	$\begin{cases} \Gamma_{e-\min} = 20.7869 \\ \Gamma_{e-\max} = 24.5755 \end{cases}$
Faulty state: LTs of 50%	$\begin{cases} \Gamma_{e-\min} = 17.5335 \\ \Gamma_{e-\max} = 24.4895 \end{cases}$

3. Experimental Setup

This section describes the configuration and experimental campaign of the test bench devoted to the control and diagnosis of the LTs fault of the ER-PMSM, to validate and verify the theoretical and numerical methodologies. The parameters of the faulty machine are reported in Table 1. The test bench is illustrated in Figure 14a. The structure of the stator winding of the machine has been designed in such a way as to offer the possibility of achieving various levels of LTs and interturn short circuit ITSC defects (Figure 14b). The architecture of the experimental platform is given in Figure 14c. The experimental bench for control and diagnosis consists mainly of a three-phase ER-PMSM of 22 poles and a power of 1.5 kW, coupled to a permanent magnet synchronous generator (PMSG). This PMSG is equipped with an incremental encoder connected to the interface with a specific cable to measure the rotation speed, as well as to capture the exact position of the rotor, whose stator is connected to a three-phase resistive load. The torque is measured via a T22/50 Nm torque meter connected to an MX440B universal amplifier module from HBM's QuantumX. The machine is driven in a closed-loop and the motor is fielded by a Semikron three-phase IGBT inverter at 5 kHz. The control and signal acquisition are performed via a dSpace-MicroLabBox 1202 platform. The DC bus voltage V_{DC} is maintained at 150 V by the grid through the three-phase autotransformer and a diode bridge rectifier.

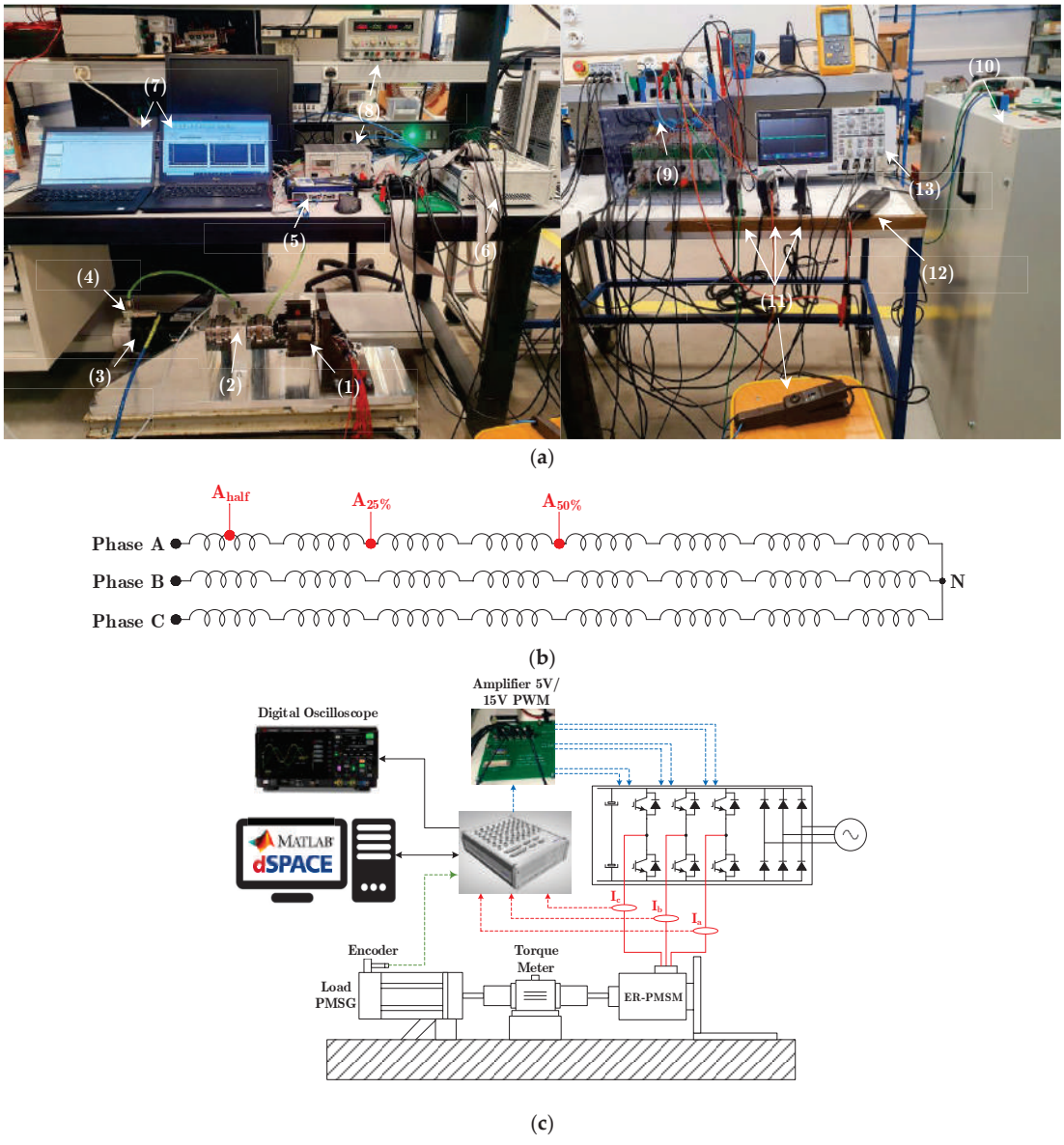

Figure 14. Experimental setup. (**a**) Global view of the test bench setup for control and diagnosis of the ER-PMSM; (1) ER-PMSM 1.5 kW; (2) torque meter T22/50 Nm; (3) load PMSG; (4) encoder; (5) MX440B module; (6) dSpace 1202 MicroLabBox; (7) MATLAB/Simulink ControlDesk platform; (8) DC power supply; (9) Semikron 3Φ inverter; (10) power supply 3Φ/50 Hz; (11) current sensors; (12) voltage sensor; (13) digital oscilloscope. (**b**) Structure of the stator winding of the ER-PMSM; (**c**) block diagram of the setup.

The faulty harmonics are aimed at kf_s, with the values measured in decibels (dB). As a result, for fault sensitivity, we consider the case of the LTs fault in half of an elementary coil A_{half}, of 25% and 50%, corresponding, respectively, to 11 turns, 44 turns, and 88 turns. In reality, the 25% and 50% cases are rarely possible, and the fault is often apparent on

some turns. Nonetheless, these values, although large, provide a vision of the tendency to monitor the machine with the fault and the evolution of these harmonics.

4. Experimental Results

Figure 14c depicts a synoptic diagram of the experimental implementation that indicates the experimental validation of the ER-PMSM control results in the healthy condition with an LTs fault of 25% and 50%. The experimental results are acquired by a digital oscilloscope linked to the real-time interface. The choice of the sampling frequency significantly impacts the quality of the signals, particularly the phase currents, speeds, and electromagnetic torque, and whatever the control algorithm used. For each healthy/faulty scenario, a load torque condition is tested: 8 Nm for a speed of 600 rpm. In this section, we present the experimental results illustrating the behavior of the ER-PMSM impacted by 25% and 50% LTs fault in its stator winding. Figure 15 depicts the flow chart of the control loop used in this paper with the LTs fault diagnosis.

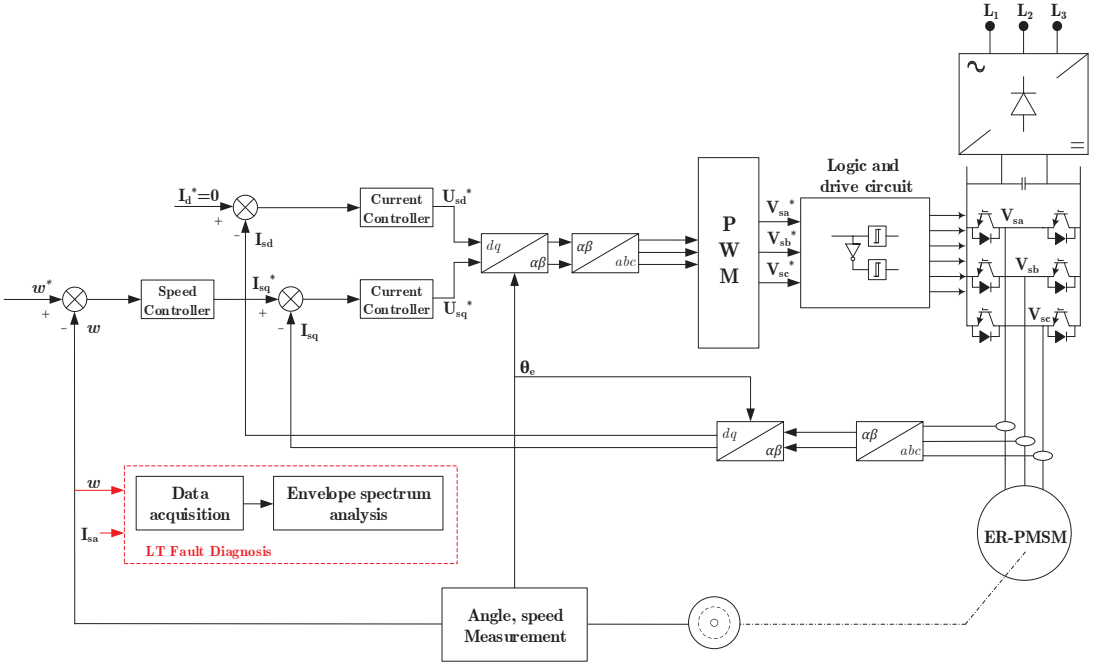

Figure 15. The flow chart of the proposed strategy.

4.1. Healthy State of the ER-PMSM

The following section examines the behavior of the machine in the healthy state. Figure 16 depicts the electrical and mechanical quantities recorded in real-time. The presentation of the experimental results will be restricted to the intersective PWM. We are interested in the rotational speed and the waveform of the stator currents. Figure 16a shows that the rotor speed follows its reference. The three-phase stator currents are shown in Figure 16b and in the d-q rotating frame in Figure 16c. The spectral analysis of the signals offers a way to diagnose this type of stator winding fault. We present the spectral analysis of the rotational speed and the stator current, using the fast Fourier transform (FFT) in steady state at rated load. We will show how this method makes it possible to determine the frequency content of the rotational speed and the stator current, and thus to find the lines associated with the LTs faults of 25% and 50%.

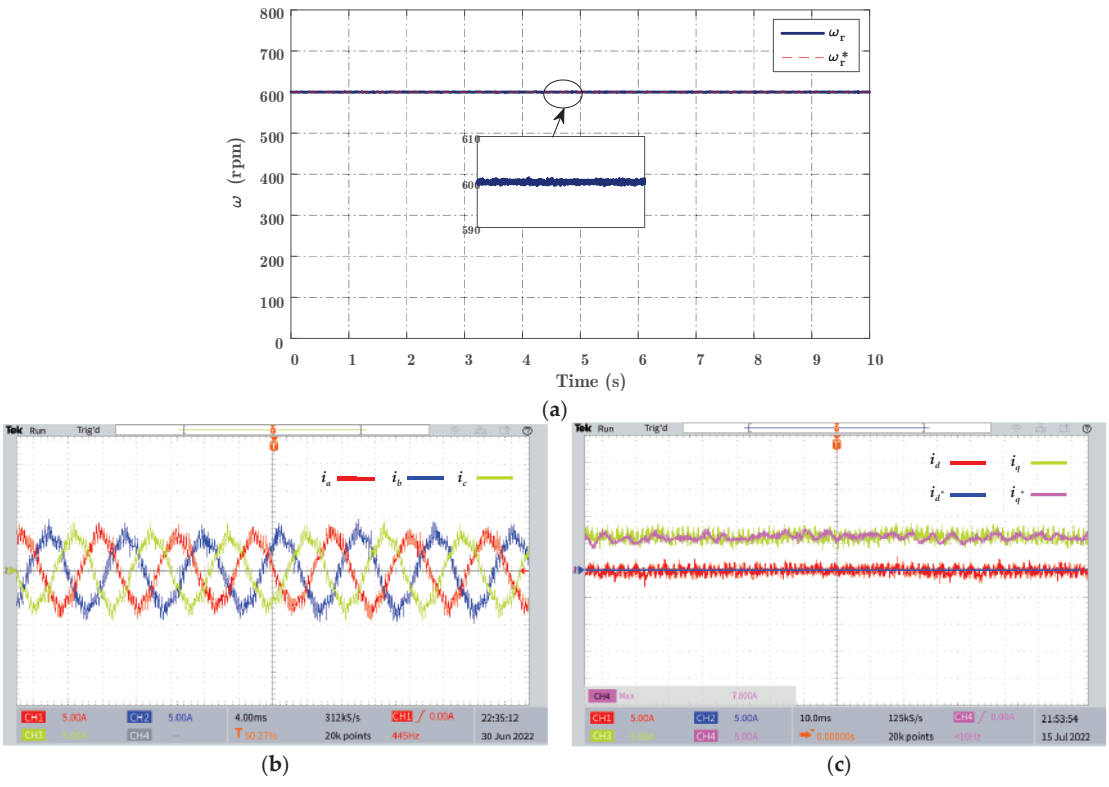

Figure 16. Electrical and mechanical characteristics in the healthy state. (**a**) Rotor speed; (**b**) stator phase currents; (**c**) direct and quadratic current component.

4.2. Faulty State of the ER-PMSM

The following section provides the experimental results of the machine with the LTs fault. Figures 17 and 18 exhibit the results obtained from the control of the different electrical and mechanical parameters of the machine with a fault in the stator winding. The presence of the LTs fault in stator phase A, according to the severity level, shows:

- The rotor speed is not substantially influenced by the LTs fault because of the control loop that hides and compensates for the effect of the fault;
- High ripples arise in the stator current of phase A, the direct current i_d, and the quadratic current i_q. The influence of the fault generates an unbalance and a noticeable variation in the current envelope.

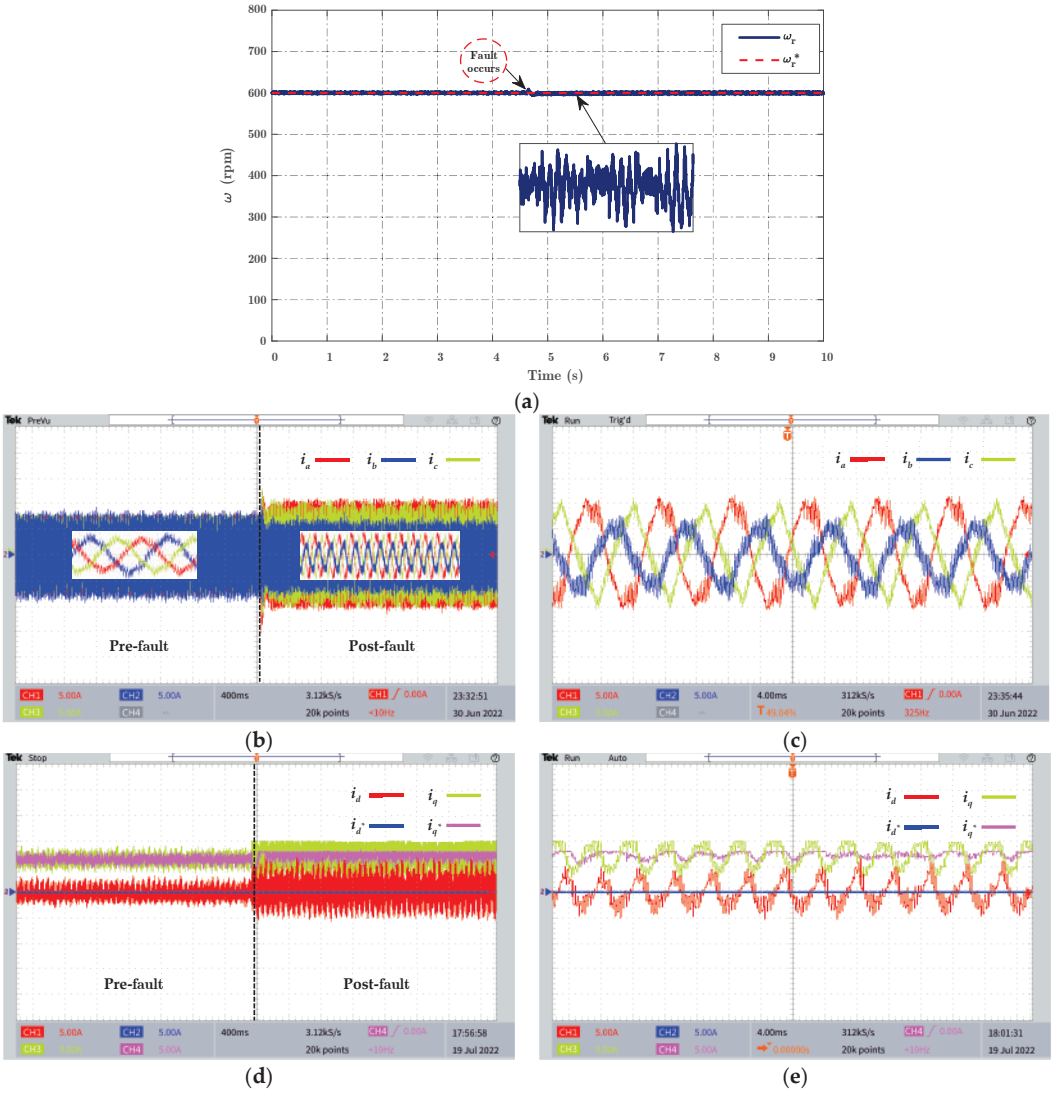

Figure 17. Electrical and mechanical characteristics in the faulty state with an LTs fault of 25%. (**a**) Rotor speed; (**b**) stator phase currents; (**c**) zoom of the stator phase currents; (**d**) direct and quadratic current component; (**e**) zoom of the direct and quadratic current component.

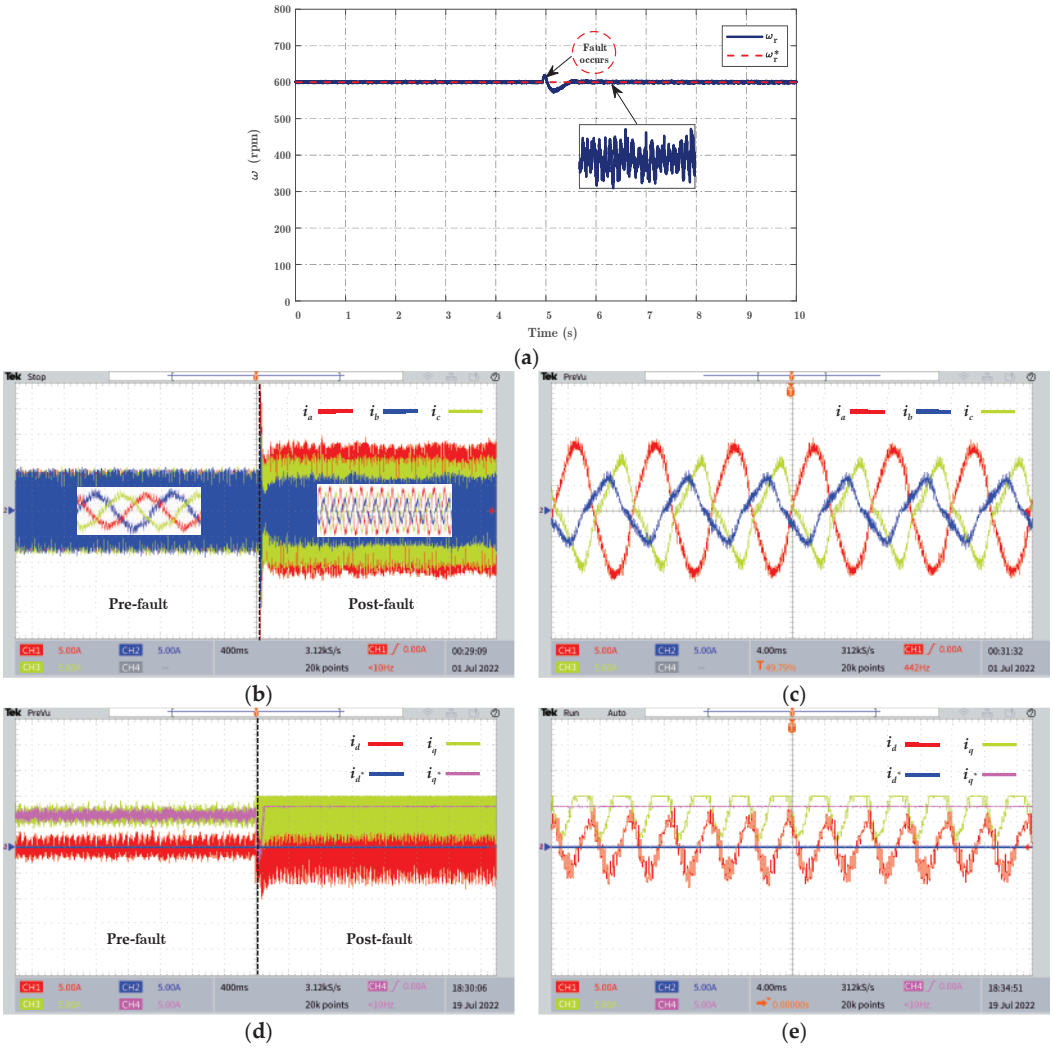

Figure 18. Electrical and mechanical characteristics in the faulty state with an LTs fault of 50%. (**a**) Rotor speed; (**b**) stator phase currents; (**c**) zoom of the stator phase currents; (**d**) direct and quadratic current component; (**e**) zoom of the direct and quadratic current component.

4.2.1. Motor Speed Signature Analysis

The examination of the motor speed signature analysis (MSSA) may provide a non-invasive method applied for the detection of stator winding faults. It is a nonparametric approach devoted to the analysis of stationary phenomena [31,32]. Figure 19 illustrates the spectrum analysis of the speed in the presence of an LTs fault of 25% to 50%. According to this study, we notice the appearance or the presence of several components having a direct relation with the defect according to the specified degree of severity. The appearance of the lines is an indicator of the existence of the LTs fault.

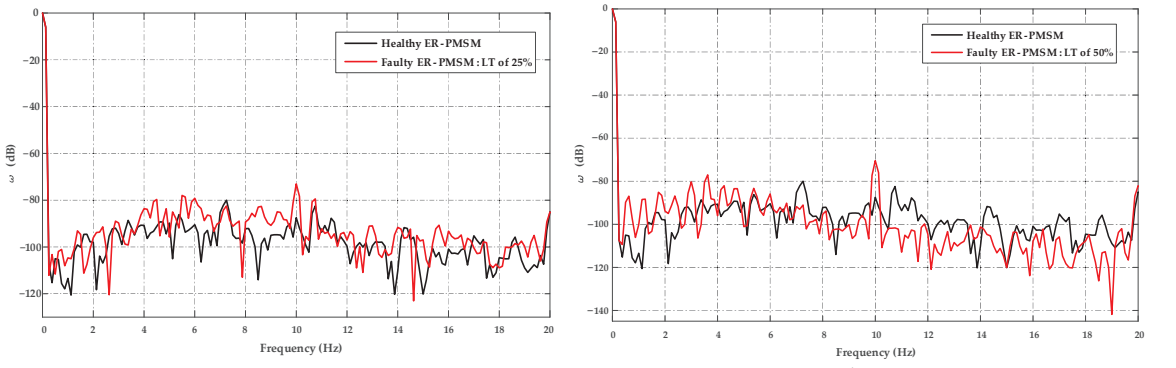

(**a**) (**b**)

Figure 19. Experimental speed spectrum of the ER-PMSM at 8 Nm load and 600 rpm, in healthy and faulty conditions. (**a**) LTs fault of 25%; (**b**) LTs fault of 50%.

4.2.2. Motor Current Signature Analysis

The next stage is to evaluate the application of the spectral analysis of the stator phase current envelope signal to LTs detection. The steady-state stator phase current envelope spectra for the motor operating with f_s = 110 Hz at 8 Nm load for 25% LTs fault level is illustrated in Figure 20. The examination of the motor current signature analysis (MCSA) reveals the influence of the LTs fault in the appearance of harmonics around the fundamental, which increases with the fault intensity. The influence of the fault is manifested by the presence of new visible frequency components in the current spectrum around the fundamental at $2f_s$ and $3f_s$. Based on this analysis, it can be inferred that the rise in amplitudes induced by the fault is significant. We can also highlight more typical criteria, such as the occurrence of kf_s frequency lines near the fundamental (k = 1, 2, 3, 4 . . .) on the stator current spectrum. Table 3 illustrates the magnitudes and frequency of the ER-PMSM stator current analysis fault.

Table 3. Experimental magnitude of current components generated by the ER-PMSM at 8 Nm load and f_s = 110 Hz.

ER-PMSM Magnitude (dB)	Current (dB)				
	f_s = 110 Hz	$2f_s$ = 220 Hz	$3f_s$ = 330 Hz	$4f_s$ = 440 Hz	$5f_s$ = 550 Hz
Healthy state	0	−43.361	−41.096	−55.616	−23.937
Faulty state: LTs of A_{half}	0	−43.177	−35.001	−45.819	−22.828
Faulty state: LTs of 25%	0	−31.636	−20.759	−38.989	−21.159
Faulty state: LTs of 50%	0	−37.708	−20.689	−42.237	−31.881

According to Figure 20, we notice that after the presence of the fault at a level of 25%, an appearance and increase of harmonics is reflected in the frequency domain. The presence of the LTs fault causes torque and speed ripples, which leads to significant mechanical vibrations in the machine, as well as an unbalance that manifests itself in the form of an important increase in the current of the faulty phase and a less significant increase for the other two phases. The spectral analysis of the MCSA indicates a visible rise in amplitude at $2f_s$, $3f_s$, and $4f_s$ for both fault levels. However, the fifth harmonic of the spectrum (550 Hz) will not be influenced by the 50% LTs fault. According to these results, we observe the existence of proportionality between the severity level of the LTs fault and the amplitude of the characteristic harmonic of the fault. Therefore, we can subsequently detect an incipient fault, which is the main objective of the LTs fault diagnosis. All information acquired from

the spectrum analysis can be employed in an automated fault detection process, while analyzing the presence of new harmonics and setting detection thresholds using adaptive observers for reconfiguration and fault isolation.

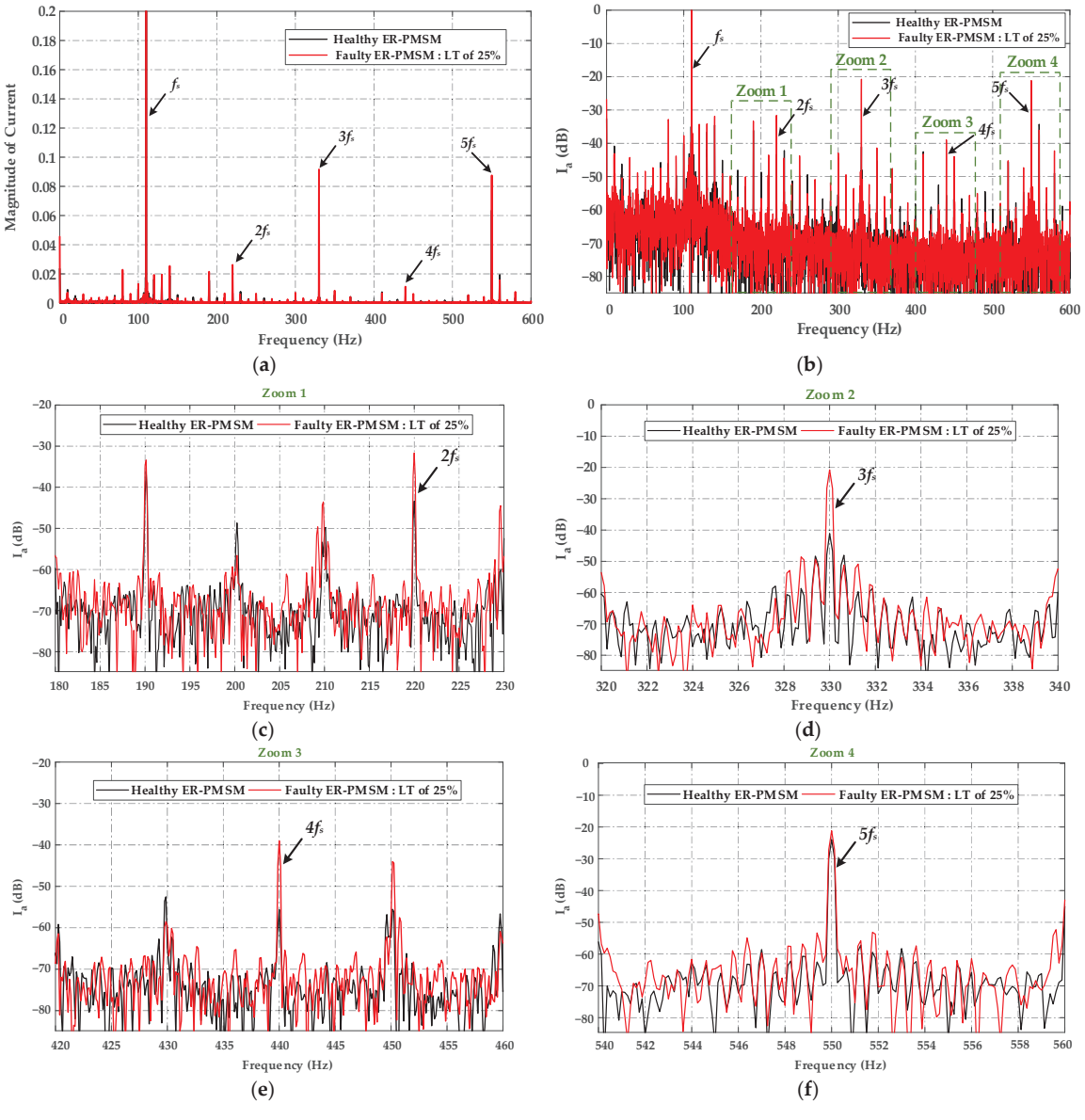

Figure 20. (**a**–**f**) Experimental current spectrum of the ER-PMSM at 8 Nm load and 600 rpm, in healthy and faulty conditions with an LTs fault of 25%.

The validity of the analytical model was proven by two approaches: FEA and experimental measurement of inductances and electromotive forces of the healthy and faulty machines. The occurrence of new harmonics can be attributed to several factors connected to the LTs fault, including torque and speed ripples, system nonlinearity, and unbalance of the ER-PMSM electromotive force. These factors can induce variations in the electri-

cal and mechanical behavior of the machine, resulting in spectral alterations that can be detected and analyzed to diagnose the fault. While validation of the analytical model by FEA and experimental measurements is crucial, understanding the underlying reasons for the spectrum changes is equally important for effective fault diagnosis in real-world applications.

5. Conclusions

This paper presents a new approach for modeling lack of turns (LTs) faults in the stator winding of external rotor permanent magnet synchronous motors (ER-PMSMs), which are of major importance in permanent magnet (PM) electrical machines since, in rotation, the induction effect generated by PMs aggravates the effects of these faults. Different operating conditions of ER-PMSMs with LTs fault provide a reference for real-time diagnosis, prediction, and maintenance planning. The suggested method has substantial advantages, such as fast calculation, good precision, and explicit physical correlations between different factors. For this purpose, theoretical operational performances of various operating situations have been evaluated.

The paper also examines the problem of diagnosing LTs faults in ER-PMSMs at their early stage by analyzing the spectral content of the speed and current signatures under various operating situations. The provided results confirm the efficiency of the diagnosis and the application of spectral analysis for the extraction of LTs fault indicators.

Future research will focus on the development and combination of adaptive fault-tolerant control of LTs faults, advanced fault diagnosis methodologies for ER-PMSMs, and the implementation of automated fault detection processes in automotive applications.

Author Contributions: Conceptualization, A.B., R.R., R.P., and D.B.; methodology, A.B., R.R., and R.P.; software, A.B.; validation, R.R., R.P., D.B., and Y.Z.; formal analysis, A.B.; investigation, A.B.; resources, A.B.; data curation, A.B.; experimental measurements, A.B.; writing—original draft preparation, A.B.; writing—review and editing, A.B., R.R., R.P., and D.B.; visualization, A.B., R.P., Y.Z., D.B., and R.R.; supervision, R.R., D.B., R.P., and Y.Z.; project administration, R.R., D.B., R.P., and Y.Z.; funding acquisition, R.R., and R.P. All authors have read and agreed to the published version of the manuscript.

Funding: This research work received no external funding.

Data Availability Statement: Data sharing not applicable.

Conflicts of Interest: The authors declare no conflict of interest.

References

1. Łebkowski, A. Design, Analysis of the Location and Materials of Neodymium Magnets on the Torque and Power of in-Wheel External Rotor PMSM for Electric Vehicles. *Energies* **2018**, *11*, 2293. [CrossRef]
2. Pop, C.V.; Fodorean, D.; Husar, C.; Irimia, C. Structural Behavior Evaluation of an In-Wheel Motor Based on Numerical and Experimental Approach. *Electr. Eng.* **2020**, *102*, 65–74. [CrossRef]
3. Ma, C.; Gao, Y.; Degano, M.; Wang, Y.; Fang, J.; Gerada, C.; Zhou, S.; Mu, Y. Eccentric Position Diagnosis of Static Eccentricity Fault of External Rotor Permanent Magnet Synchronous Motor as an In-wheel Motor. *IET Electr. Power Appl.* **2020**, *14*, 2263–2272. [CrossRef]
4. Ebrahimi, S.H.; Choux, M.; Huynh, V.K. Real-Time Detection of Incipient Inter-Turn Short Circuit and Sensor Faults in Permanent Magnet Synchronous Motor Drives Based on Generalized Likelihood Ratio Test and Structural Analysis. *Sensors* **2022**, *22*, 3407. [CrossRef] [PubMed]
5. Ebrahimi, B.M.; Javan Roshtkhari, M.; Faiz, J.; Khatami, S.V. Advanced Eccentricity Fault Recognition in Permanent Magnet Synchronous Motors Using Stator Current Signature Analysis. *IEEE Trans. Ind. Electron.* **2014**, *61*, 2041–2052. [CrossRef]
6. Belkhadir, A.; Belkhayat, D.; Zidani, Y.; Pusca, R.; Romary, R. Torque Ripple Minimization Control of Permanent Magnet Synchronous Motor Using Adaptive Ant Colony Optimization. In Proceedings of the 2022 8th International Conference on Control, Decision and Information Technologies (CoDIT), Istanbul, Turkey, 17–20 May 2022; pp. 629–635.
7. Orlowska-Kowalska, T.; Wolkiewicz, M.; Pietrzak, P.; Skowron, M.; Ewert, P.; Tarchala, G.; Krzysztofiak, M.; Kowalski, C.T. Fault Diagnosis and Fault-Tolerant Control of PMSM Drives–State of the Art and Future Challenges. *IEEE Access* **2022**, *10*, 59979–60024. [CrossRef]

8. Kudelina, K.; Asad, B.; Vaimann, T.; Rassõlkin, A.; Kallaste, A.; Khang, H. Van Methods of Condition Monitoring and Fault Detection for Electrical Machines. *Energies* **2021**, *14*, 7459. [CrossRef]
9. Ullah, Z.; Hur, J. A Comprehensive Review of Winding Short Circuit Fault and Irreversible Demagnetization Fault Detection in PM Type Machines. *Energies* **2018**, *11*, 3309. [CrossRef]
10. Chen, Y.; Liang, S.; Li, W.; Liang, H.; Wang, C. Faults and Diagnosis Methods of Permanent Magnet Synchronous Motors: A Review. *Appl. Sci.* **2019**, *9*, 2116. [CrossRef]
11. Solís, R.; Torres, L.; Pérez, P. Review of Methods for Diagnosing Faults in the Stators of BLDC Motors. *Processes* **2022**, *11*, 82. [CrossRef]
12. Liang, H.; Chen, Y.; Liang, S.; Wang, C. Fault Detection of Stator Inter-Turn Short-Circuit in PMSM on Stator Current and Vibration Signal. *Appl. Sci.* **2018**, *8*, 1677. [CrossRef]
13. Hang, J.; Zhang, J.; Cheng, M.; Huang, J. Online Interturn Fault Diagnosis of Permanent Magnet Synchronous Machine Using Zero-Sequence Components. *IEEE Trans. Power Electron.* **2015**, *30*, 6731–6741. [CrossRef]
14. Yepes, A.G.; Fonseca, D.S.B.; Antunes, H.R.P.; Lopez, O.; Marques Cardoso, A.J.; Doval-Gandoy, J. Discrimination Between Eccentricity and Interturn Faults Using Current or Voltage-Reference Signature Analysis in Symmetrical Six-Phase Induction Machines. *IEEE Trans. Power Electron.* **2023**, *38*, 2421–2434. [CrossRef]
15. Yang, M.; Chai, N.; Liu, Z.; Ren, B.; Xu, D. Motor Speed Signature Analysis for Local Bearing Fault Detection with Noise Cancellation Based on Improved Drive Algorithm. *IEEE Trans. Ind. Electron.* **2020**, *67*, 4172–4182. [CrossRef]
16. Haje Obeid, N.; Battiston, A.; Boileau, T.; Nahid-Mobarakeh, B. Early Intermittent Interturn Fault Detection and Localization for a Permanent Magnet Synchronous Motor of Electrical Vehicles Using Wavelet Transform. *IEEE Trans. Transp. Electrif.* **2017**, *3*, 694–702. [CrossRef]
17. Espinosa, A.G.; Rosero, J.A.; Cusido, J.; Romeral, L.; Ortega, J.A. Fault Detection by Means of Hilbert–Huang Transform of the Stator Current in a PMSM With Demagnetization. *IEEE Trans. Energy Convers.* **2010**, *25*, 312–318. [CrossRef]
18. Pusca, R.; Romary, R.; Touti, E.; Livinti, P.; Nuca, I.; Ceban, A. Procedure for Detection of Stator Inter-Turn Short Circuit in Ac Machines Measuring the External Magnetic Field. *Energies* **2021**, *14*, 1132. [CrossRef]
19. Irhoumah, M.; Pusca, R.; Lefèvre, E.; Mercier, D.; Romary, R. Stray Flux Multi-Sensor for Stator Fault Detection in Synchronous Machines. *Electronics* **2021**, *10*, 2313. [CrossRef]
20. Irhoumah, M.; Pusca, R.; Lefevre, E.; Mercier, D.; Romary, R.; Demian, C. Information Fusion with Belief Functions for Detection of Interturn Short-Circuit Faults in Electrical Machines Using External Flux Sensors. *IEEE Trans. Ind. Electron.* **2018**, *65*, 2642–2652. [CrossRef]
21. Irhoumah, M.; Pusca, R.; Lefevre, E.; Mercier, D.; Romary, R. Detection of the Stator Winding Inter-Turn Faults in Asynchronous and Synchronous Machines Through the Correlation Between Harmonics of the Voltage of Two Magnetic Flux Sensors. *IEEE Trans. Ind. Appl.* **2019**, *55*, 2682–2689. [CrossRef]
22. Shih, K.-J.; Hsieh, M.-F.; Chen, B.-J.; Huang, S.-F. Machine Learning for Inter-Turn Short-Circuit Fault Diagnosis in Permanent Magnet Synchronous Motors. *IEEE Trans. Magn.* **2022**, *58*, 1–7. [CrossRef]
23. Pietrzak, P.; Wolkiewicz, M.; Orlowska-Kowalska, T. PMSM Stator Winding Fault Detection and Classification Based on Bispectrum Analysis and Convolutional Neural Network. *IEEE Trans. Ind. Electron.* **2023**, *70*, 5192–5202. [CrossRef]
24. Farshadnia, M. *Advanced Theory of Fractional-Slot Concentrated- Wound Permanent Magnet Synchronous Machines*; Springer: Berlin/Heidelberg, Germany, 2018; ISBN 978-981-10-8708-0.
25. Pyrhonen, J. Juha Pyrhönen, Tapani Jokinen, Valéria Hrabovcová. In *Design of Rotating Electrical Machines*; Wiley: Hoboken, NJ, USA, 2014; Volume 614, ISBN 9781118581575.
26. Bianchi, N.; Fornasiero, E. Impact of MMF Space Harmonic on Rotor Losses in Fractional-Slot Permanent-Magnet Machines. *IEEE Trans. Energy Convers.* **2009**, *24*, 323–328. [CrossRef]
27. EL-Refaie, A.M. Fractional-Slot Concentrated-Windings Synchronous Permanent Magnet Machines: Opportunities and Challenges. *IEEE Trans. Ind. Electron.* **2010**, *57*, 107–121. [CrossRef]
28. Di Tommaso, A.O.; Genduso, F.; Miceli, R. A Software for the Evaluation of Winding Factor Harmonic Distribution in High Efficiency Electrical Motors and Generators. In Proceedings of the 2013 8th Eighth International Conference and Exhibition on Ecological Vehicles and Renewable Energies (EVER), Monte Carlo, Monaco, 27–30 March 2013. [CrossRef]
29. Hamiti, T.; Lubin, T.; Baghli, L.; Rezzoug, A. Modeling of a Synchronous Reluctance Machine Accounting for Space Harmonics in View of Torque Ripple Minimization. *Math. Comput. Simul.* **2010**, *81*, 354–366. [CrossRef]
30. *IEEE Std 115a*; IEEE Standard Procedures for Obtaining Synchronous Machine Parameters by Standstill Frequency Response Testing. IEEE: Piscatway, NJ, USA, 1987.
31. Shi, P.; Chen, Z.; Vagapov, Y.; Zouaoui, Z. A New Diagnosis of Broken Rotor Bar Fault Extent in Three Phase Squirrel Cage Induction Motor. *Mech. Syst. Signal Process.* **2014**, *42*, 388–403. [CrossRef]
32. Moumene, I.; Ouelaa, N. Application of the Wavelets Multiresolution Analysis and the High-Frequency Resonance Technique for Gears and Bearings Faults Diagnosis. *Int. J. Adv. Manuf. Technol.* **2016**, *83*, 1315–1339. [CrossRef]

energies

MDPI

Article

Impact of Inter-Turn Short Circuit in Excitation Windings on Magnetic Field and Stator Current of Synchronous Condenser under Unbalanced Voltage

Junqing Li [1], Chengzhi Zhang [1], Yuling He [2,*], Xiaodong Hu [1], Jiya Geng [1] and Yapeng Ma [1]

[1] School of Electrical and Electronic Engineering, North China Electric Power University, Baoding 071003, China
[2] Department of Mechanical Engineering, North China Electric Power University, Baoding 071003, China
* Correspondence: heyuling1@163.com

Abstract: Inter-turn short circuit in the excitation windings of synchronous condensers is a common fault that directly impacts their normal operation. However, current fault analysis and diagnosis of synchronous condensers primarily rely on voltage-balanced conditions, while research on short-circuit faults under unbalanced voltage conditions is limited. Therefore, this paper aims to analyze the fault characteristics of inter-turn short circuits in the excitation windings of synchronous condensers under unbalanced grid voltage. Mathematical models were developed to represent the air gap flux density and stator parallel currents for four operating conditions: normal operation and inter-turn short circuit fault under balanced voltage, as well as a process without fault and with inter-turn short circuit fault under unbalanced voltage. By comparing the harmonic content and amplitudes, various aspects of the fault mechanism of synchronous condensers were revealed, and the operating characteristics under different conditions were analyzed. Considering the four aforementioned operating conditions, finite element simulation models were created for the TTS-300-2 synchronous condenser in a specific substation as a case study. The results demonstrate that the inter-turn short circuit fault in the excitation windings under unbalanced voltage leads to an increase in even harmonic currents in the stator parallel currents, particularly the second and fourth harmonics. This validates the accuracy of the theoretical analysis findings.

Keywords: synchronous condenser; unbalanced voltage; inter-turn short circuit in excitation windings; finite element; fault analysis; stator parallel currents

Citation: Li, J.; Zhang, C.; He, Y.; Hu, X.; Geng, J.; Ma, Y. Impact of Inter-Turn Short Circuit in Excitation Windings on Magnetic Field and Stator Current of Synchronous Condenser under Unbalanced Voltage. *Energies* **2023**, *16*, 5695. https://doi.org/10.3390/en16155695

Academic Editor: Gianluca Brando

Received: 6 June 2023
Revised: 23 July 2023
Accepted: 26 July 2023
Published: 29 July 2023

1. Introduction

Currently, the ultra-high voltage direct current (UHVDC) system is rapidly developing, imposing more significant requirements on reactive power within the power grid. Large-scale synchronous condensers (LSSC), with high capacity, exhibit exceptional transient reactive power support and short-term overload capabilities. By positioning LSSC at the inverter end of a weak AC grid, commutation failures can be effectively prevented, and fault clearing speed can be accelerated [1]. Consequently, ensuring the reliable operation of LSSC is crucial in enhancing the dynamic voltage stability of power systems and ensuring the stable operation of UHVDC transmission [2].

Inter-turn short circuit in the excitation windings of synchronous condensers is a common fault not only limits the reactive power capability but also increases the excitation current, power losses, and local temperature of the synchronous condenser. In severe cases, it can exacerbate rotor vibrations, generate significant axial magnetization, and even completely shut down the synchronous condenser [3]. Analyzing characteristic patterns and accurately diagnosing inter-turn short circuit faults in the excitation windings are complex tasks within the field of system engineering. Fault diagnosis is typically carried out using methods such as the DC resistance method [4], AC impedance method [5], and repetitive pulse method [6]. Since synchronous condensers share structural similarities

with synchronous generators, research findings related to synchronous generators can be utilized for synchronous condensers [7–11]. M. Xu et al. [12] comprehensively analyzed the stator circulating current within parallel branches, considering various degrees and positions of rotor inter-turn short circuits. The analysis was performed using the finite element method, yielding valuable insights into the behavior of the circulating current. Currently, several studies have been conducted on inter-turn short circuit faults in the excitation windings of synchronous condensers. G. Xu et al. [13] present the single-phase short circuit faults' electromagnetic and temperature field calculation and the experimental validation. M. Ma et al. [14] investigated inter-turn short circuit faults in the rotor windings of synchronous condensers by analyzing commutation failures in high-voltage direct current transmission. Finite element analysis revealed that commutation failures can cause abnormal vibrations in the rotor side of the synchronous condenser, which positively correlates with the severity of the fault. Y. Zhang et al. [15] applied wavelet transform to preprocessed excitation current signals extracted from normal and faulty states of the synchronous condenser. The extracted features were input into a radial basis function neural network for fault diagnosis. Z. Chen et al. [16] analyzed inter-turn short circuit faults in the rotor windings of synchronous condensers from the perspective of temperature distribution and validated the analysis through finite element simulations. C. Wei et al. [17] investigated the relationship between the number of short-circuited turns in the excitation windings of synchronous condensers and the magnetic field current in the rotor windings, proposing an online monitoring fault diagnosis strategy. A. N. Novozhilov et al. [18] established a mathematical model for inter-turn short circuit faults in the excitation windings of synchronous condensers, achieving an accuracy range of 5% to 10%. Most existing research on the mentioned faults primarily focuses on the short circuit between turns in the excitation winding. However, the voltage waveform of the grid deviates from a standard sinusoidal shape due to the non-standard sinusoidal waveform generated by most generators. As a result, when a short circuit occurs in the excitation winding, it can be seen as a combination of unbalanced voltage and a short circuit between turns in the excitation winding. The prevalence of unbalanced voltage further complicates the fault analysis, as the fault environments studied in literature may not accurately reflect real-world scenarios. Consequently, matching the observed fault characteristics of the synchronous condenser with known fault patterns during on-site diagnostics becomes challenging, often leading to incorrect or even misdiagnosis. Therefore, it is crucial to research the compound fault of unbalanced voltage and short circuits in the excitation winding. This research aims to identify distinctive fault characteristics specific to this type of fault and differentiate them from fault characteristics caused by individual faults. Such investigations are essential for achieving accurate diagnosis and establishing reliable diagnostic criteria in scenarios involving these compound faults. J. LI et al. [19] conducted a simulation study on the inter-turn short circuit fault in the stator winding of a doubly-fed induction generator. They used finite element modeling to analyze the changes in stator line voltage, rotor line current, and electromagnetic torque when the excitation winding experiences an inter-turn short circuit fault, considering the presence of inherent grid voltage imbalance and static eccentricity. However, their study [19] focused solely on simulation modeling analysis and did not investigate the theoretical research on mathematical expressions of the relevant fault characteristic quantities after the occurrence of the fault. As a result, their study has certain limitations that need to be addressed.

Among the electrical characteristic-oriented methods, the current-based method is most widely employed since it does not require extra equipment and can make full use of the stator winding as search coils for further processing. In addition, the parallel branch circulating current signal in the stator winding carries valuable fault information and, in certain cases, offers more effective fault diagnosis than rotor vibration signals. To address the issue of voltage imbalance, this paper begins by investigating the air gap flux density and proceeds to derive expressions for both the air gap flux density and stator parallel branch circulating current of the synchronous condenser in four distinct operating

conditions. Additionally, it conducts a comprehensive analysis of the characteristics of the stator parallel branch circulating current under different operating conditions, shedding light on their intricate dynamics: normal operation of the synchronous condenser under balanced voltage, inter-turn short circuit fault in the excitation windings of the synchronous condenser under balanced voltage, normal operation of the synchronous condenser under voltage imbalance, and inter-turn short circuit fault in the excitation windings of the synchronous condenser under voltage imbalance. The degree of voltage imbalance is varied by adjusting the voltage magnitude. Mathematical representations are derived, and a finite element simulation model of the synchronous condenser is constructed to validate the analysis. This study aims to provide a theoretical basis for diagnosing inter-turn short circuit faults in the excitation windings of synchronous condensers under voltage imbalance conditions.

The main structure of this paper is as follows: In Section 2, the expressions for the air gap flux density and stator parallel currents under different fault types of a synchronous condenser are derived, and the impacts of faults are analyzed from a theoretical perspective. Section 3 validates the proposed analytical model's effectiveness and accuracy using finite element analysis, and the changes in air gap flux density and stator parallel currents after faults in the synchronous condenser are analyzed using the finite element model, which is consistent with the theoretical analysis. Finally, Section 4 summarizes the conclusions of this paper.

2. Analysis of Composite Faults in Synchronous Condensers

To compare the variations in air gap magnetic flux density, stator parallel current amplitude, and harmonic content under different operating conditions, this paper focuses on four scenarios: normal operation of the synchronous condenser under balanced voltage, inter-turn short circuit fault in the excitation windings of the synchronous condenser under balanced voltage, normal operation of the synchronous condenser under voltage imbalance, and inter-turn short circuit fault in the excitation windings of the synchronous condenser under voltage imbalance. Compared to symmetrical grid voltage, it is assumed that when the grid voltage becomes asymmetric, the amplitude of one or two phases is reduced. Nevertheless, the derived formulas apply to all cases, demonstrating their universality.

2.1. Analysis of Air Gap Magnetic Field

2.1.1. Air Gap Magnetic Potential during Normal Operation of Synchronous Condenser under Balanced Grid Voltage

Neglecting higher-order harmonics, the air gap magnetic potential of the synchronous condenser during normal operation can be expressed as follows:

$$\begin{aligned} f(\alpha_m, t) &= F_s \cos(\omega t - \alpha_m - \psi - \tfrac{\pi}{2}) + F_r \cos(\omega t - \alpha_m) \\ &= F_1 \cos(\omega t - \alpha_m - \beta) \end{aligned} \tag{1}$$

$$F_1 = \sqrt{F_s^2 \cos^2 \psi + (F_r - F_s \sin \psi)^2} \tag{2}$$

$$\beta = \arctan \frac{F_s \cos \psi}{F_r - F_s \sin \psi} \tag{3}$$

where ω is the stator current angular frequency and rotor rotational angular velocity, α_m is the stator spatial electrical angle, ψ is the internal power factor angle, F_s is the armature magnetic flux amplitude, and F_r is the excitation magnetic flux amplitude.

2.1.2. Air Gap Magnetic Potential during Inter-Turn Short Circuit Fault in the Excitation Windings of Synchronous Condenser under Balanced Grid Voltage

When an inter-turn short circuit occurs in the excitation windings of the synchronous condenser, it generates a counteracting magnetic field [20]. The reverse magnetic MMF (Magneto-Motive Force) generated by the short-circuited winding is given by

$$F_d(\theta_r) = \begin{cases} -\frac{I_{f0}N_{short}(2\pi-\alpha)}{2\pi} & -\frac{\alpha}{2} < \theta_r < \frac{\alpha}{2} \\ \frac{I_{f0}N_{short}\alpha}{2\pi} & \text{other} \end{cases} \tag{4}$$

where I_{f0} is the excitation current, N_{short} is the number of turns in the short-circuited winding in the same slot, α is the mechanical angle between the slot where the short-circuited winding is located and the adjacent slot, θ_r is the mechanical angle of the rotor. The magnetic potential resulting from the short circuit can be expressed in terms of its harmonic components through Fourier decomposition:

$$F_d(\theta_r) = \frac{-2N_{short}I_{f0}}{\pi}\sum_{n=1}^{\infty}\frac{\sin(n\alpha/2)}{n}\cos n\theta_r \tag{5}$$

After performing the Fourier transform on $F_d(\theta_r)$, it can be observed that the main magnetic field in the air gap exhibits various harmonics. When $\alpha \neq 2$ kπ/n, taking $n = 1,2$, and $\theta_r = \omega t - \alpha_m$, we have

$$\begin{aligned} f(\alpha_m, t) &= F_s\cos(\omega t - \alpha_m - \psi - \tfrac{\pi}{2}) + F_r\cos(\omega t - \alpha_m) \\ &\quad -F_{d1}\cos(\omega t - \alpha_m) - F_{d2}\cos(2\omega t - 2\alpha_m) \\ &= F_1\cos(\omega t - \alpha_m - \beta) - F_{d2}\cos(2\omega t - 2\alpha_m) \end{aligned} \tag{6}$$

$$F_{d1} = \frac{2N_{short}I_{f0}}{\pi}\sin\frac{\alpha}{2} \tag{7}$$

$$F_{d2} = \frac{N_{short}I_{f0}}{\pi}\sin\alpha \tag{8}$$

$$F_1 = \sqrt{F_s^2\cos^2\psi + (F_r - F_{d1} - F_s\sin\psi)^2} \tag{9}$$

$$\beta = \arctan\frac{F_s\cos\psi}{F_r - F_{d1} - F_s\sin\psi} \tag{10}$$

2.1.3. The Air Gap Magnetic Potential of the Synchronous Condenser under Unbalanced Grid Voltage Conditions without Any Faults Occurring

Under balanced grid voltage, the armature magnetic field of the synchronous condenser exhibits a synchronized circular rotation with the rotor. However, when the grid voltage becomes unbalanced, the armature magnetic field undergoes distortion, assuming an elliptical shape. The symmetrical component method can be applied to characterize the armature magnetic field expression in such scenarios. In this method, the positive-sequence armature magnetic field rotates synchronously with the rotor, while the negative-sequence armature magnetic field rotates in the opposite direction. Meanwhile, the zero-sequence armature magnetic field remains at zero [21]. Consequently, in the presence of an unbalanced grid voltage, the expression for the armature magnetic potential is given by

$$f_s(\alpha_m, t) = F_s^+\cos(\omega t - \alpha_m - \psi - \frac{\pi}{2}) + F_s^-\cos(\omega t + \alpha_m - \psi - \frac{\pi}{2}) \tag{11}$$

where $F_s{}^+$ is the positive-sequence armature magnetic flux amplitude, $F_s{}^-$ is the negative-sequence armature magnetic flux amplitude. Based on the previous assumption, both $F_s{}^+$ and $F_s{}^-$ are smaller than F_s. The negative-sequence magnetic field caused by the unbal-

anced grid voltage induces a double-frequency current in the rotor winding. Therefore, the expression for the excitation current is as follows:

$$I_f(t) = I_{f0} + I_{f2}\cos 2\omega t \tag{12}$$

where I_{f0} is the direct current excitation current generated by the generator excitation system, I_{f2} is the amplitude of the twice-frequency excitation current induced. The expression for the excitation magnetic field generated by the excitation current is as follows:

$$\begin{aligned} f_r(\alpha_m, t) &= (I_{f0} + I_{f2}\cos 2\omega t)Nk\cos(\omega t - \alpha_m) \\ &= F_r\cos(\omega t - \alpha_m) + I_{f2}Nk\cos 2\omega t\cos(\omega t - \alpha_m) \end{aligned} \tag{13}$$

where k is the waveform coefficient of the excitation magnetic flux. Therefore, the expression for the synthesized air-gap magnetic potential generated under unbalanced voltage conditions is as follows:

$$\begin{aligned} f(\alpha_m, t) &= f_s(\alpha_m, t) + f_r(\alpha_m, t) \\ &= F_1\cos(\omega t - \alpha_m - \beta) + F_2\cos(\omega t + \alpha_m - \gamma) \\ &+ \tfrac{1}{2}I_{f2}Nk\cos(3\omega t - \alpha_m) \end{aligned} \tag{14}$$

$$F_1 = \sqrt{F_s^{+2}\cos^2\psi + \left(F_r - F_s^+\sin\psi\right)^2} \tag{15}$$

$$\beta = \arctan\frac{F_s^+\cos\psi}{F_r - F_s^+\sin\psi} \tag{16}$$

$$F_2 = \sqrt{F_s^{-2}\cos^2\psi + \left(\frac{1}{2}I_{f2}NK - F_s^-\sin\psi\right)^2} \tag{17}$$

$$\gamma = \arctan\frac{F_s^-\cos\psi}{\frac{1}{2}I_{f2}NK - F_s^-\sin\psi} \tag{18}$$

Equations (14)–(18) reveal that unbalanced voltage conditions lead to the induction of a double-frequency current in the excitation winding of the synchronous condenser. As a consequence, third harmonic components are produced in the air gap. It is worth noting that the amplitude of the third harmonic exhibits a direct proportionality to the double-frequency current.

2.1.4. The Air Gap Magnetic Flux in the Synchronous Condenser When There Is an Inter-Turn Short Circuit in the Excitation Winding under Unbalanced Grid Voltage

Under unbalanced grid voltage, a negative-sequence magnetic field is produced, generating double-frequency excitation current in the rotor. Therefore, it becomes essential to account for the influence of this double-frequency current on the excitation magnetic flux when investigating inter-turn short circuits in the excitation winding. The expression for the air gap magnetic flux in the synchronous condenser under these circumstances is as follows:

$$\begin{aligned} f(\alpha_m, t) &= F_s^+\cos(\omega t - \alpha_m - \psi - \tfrac{\pi}{2}) + F_s^-\cos(\omega t + \alpha_m - \psi - \tfrac{\pi}{2}) \\ &+ F_r\cos(\omega t - \alpha_m) + I_{f2}Nk\cos 2\omega t\cos(\omega t - \alpha_m) \\ &- F_{d1}\cos(\omega t - \alpha_m) - F_{d2}\cos(2\omega t - 2\alpha_m) \\ &- F'_{d1}\cos(\omega t - \alpha_m)\cos 2\omega t - F'_{d2}\cos(2\omega t - 2\alpha_m)\cos 2\omega t \\ &= F_1\cos(\omega t - \alpha_m - \beta) + F_2\cos(\omega t + \alpha_m - \gamma) \\ &- F_{d2}\cos(2\omega t - 2\alpha_m) + (\tfrac{1}{2}I_{f2}Nk - \tfrac{1}{2}F'_{d1})\cos(3\omega t - \alpha_m) \\ &- \tfrac{1}{2}F'_{d2}\cos 2\alpha_m - \tfrac{1}{2}F'_{d2}\cos(4\omega t - 2\alpha_m) \end{aligned} \tag{19}$$

$$F'_{d1} = \frac{2N_{short}I_{f2}}{\pi}\sin\frac{\alpha}{2} \tag{20}$$

$$F'_{d2} = \frac{N_{short}I_{f2}}{\pi}\sin\alpha \tag{21}$$

$$F_1 = \sqrt{F_s^{+2}\cos^2\psi + (F_r - F_{d1} - F_s^{+}\sin\psi)^2} \tag{22}$$

$$\beta = \arctan\frac{F_s^{+}\cos\psi}{F_r - F_{d1} - F_s^{+}\sin\psi} \tag{23}$$

$$F_2 = \sqrt{F_s^{-2}\cos^2\psi + (\frac{1}{2}I_{f2}NK - \frac{1}{2}F'_{d1} - F_s^{-}\sin\psi)^2} \tag{24}$$

$$\gamma = \arctan\frac{F_s^{-}\cos\psi}{\frac{1}{2}I_{f2}NK - \frac{1}{2}F'_{d1} - F_s^{-}\sin\psi} \tag{25}$$

According to Equations (19)–(25), the presence of unbalanced voltage, coupled with an inter-turn short circuit in the excitation winding, gives rise to a multifaceted air gap magnetic flux in the synchronous condenser. This flux encompasses several components, namely even harmonic components induced by the inter-turn short circuit, a DC component introduced by the rotor's double-frequency current, and odd harmonic components.

2.1.5. Air Gap Magnetic Flux Density

During operation, the air gap magnetic flux density of the synchronous condenser, denoted as Λ_0 per unit area, remains constant. The following expression is derived to represent the air gap magnetic flux density:

$$B(\alpha_m, t) = \Lambda_0 f(\alpha_m, t) \tag{26}$$

2.2. Analysis of Parallel Branch Current Circulation in the Stator

The stator winding of a large synchronous condenser is connected in a double Y configuration, employing a three-phase double-layer winding form. This configuration comprises two parallel branches for each phase (A, B, and C), with multiple coil windings connected in series within each branch. Hence, the expression for the instantaneous value of the induced electromotive force in a single branch of the parallel stator winding of the synchronous condenser is as follows:

$$\begin{aligned} e_1(\alpha_m, t) &= N_z k_{w1} B(\alpha_m, t) l v \\ &= N_z k_{w1} B(\alpha_m, t) l (2\tau f) \\ &= 2N_z k_{w1} \tau l f \Lambda_0 F_1 \cos(\omega t - \alpha_m - \beta) \end{aligned} \tag{27}$$

where l is the air gap length, f is the electrical frequency, N_z is the number of conductors connected in series in a single stator branch, and k_{w1} is the fundamental winding factor. Figure 1 illustrates the equivalent circuit of the parallel branch in phase A of the synchronous condenser. The circuit includes R_{a1}, R_{a2}, X_{a1}, and X_{a2}, which represent the resistance and leakage reactance of the two branches. The circulating current is denoted as i_c.

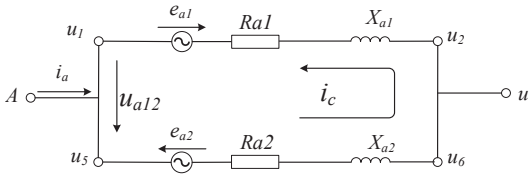

Figure 1. A phase winding equivalent circuit diagram.

When the synchronous condenser is operating normally, applying Kirchhoff's Voltage Law (KVL) to the stator parallel circuit yields the following equation:

$$e_1(\alpha_m, t) + e_2(\alpha_m, t) + i_c(R_{a1} + R_{a2}) + ji_c(X_{a1} + X_{a2}) = 0 \tag{28}$$

The expression for the stator parallel circuit current can be obtained from Equation (28) as follows:

$$i_c = -\frac{e_1(\alpha_m, t) + e_2(\alpha_m, t)}{(R_{a1} + R_{a2}) + j(X_{a1} + X_{a2})} \tag{29}$$

2.2.1. Under the Condition of Balanced Grid Voltage, the Synchronous Condenser Operates without Any Faults

The induced electromotive force in the two parallel branches during the normal operation of the synchronous condenser is given by the following expression:

$$\begin{cases} e_1(\alpha_m, t) = 2N_z k_{w1} \tau l f \Lambda_0 [F_1 \cos(\omega t - \alpha_m - \beta)] \\ e_2(\alpha_m, t) = 2N_z k_{w1} \tau l f \Lambda_0 [F_1 \cos(\omega t - \alpha_m - \pi - \beta)] \end{cases} \tag{30}$$

The stator parallel branch current in this case is

$$i_c = -\frac{e_1(\alpha_m, t) + e_2(\alpha_m, t)}{(R_{a1} + R_{a2}) + j(X_{a1} + X_{a2})} = 0 \tag{31}$$

Based on Equation (31), it can be concluded that during normal operation of the synchronous condenser, the stator parallel branch current is zero, indicating the absence of any current flowing through the stator parallel branches in this case.

2.2.2. Grid Voltage Balance Synchronous Condenser Excitation Winding Inter-Turn Short Circuit Occurs

When a short circuit occurs in the excitation winding of the synchronous condenser, the induced electromotive force in the two parallel branches can be expressed as follows:

$$\begin{cases} e_1(\alpha_m, t) & = 2N_z k_{w1} \tau l f \Lambda_0 \\ & \quad [F_1 \cos(\omega t - \alpha_m - \beta) - F_{d2} \cos(2\omega t - 2\alpha_m)] \\ e_2(\alpha_m, t) & = 2N_z k_{w1} \tau l f \Lambda_0 \\ & \quad [F_1 \cos(\omega t - \alpha_m - \pi - \beta) - F_{d2} \cos(2\omega t - 2\alpha_m - 2\pi)] \end{cases} \tag{32}$$

The parallel stator current is given by

$$\begin{aligned} i_c &= -\frac{e_1(\alpha_m, t) + e_2(\alpha_m, t)}{(R_{a1} + R_{a2}) + j(X_{a1} + X_{a2})} \\ &= \frac{4N_z k_{w1} \tau l f \Lambda_0 F_{d2} \cos 2(\omega t - \alpha_m)}{(R_{a1} + R_{a2}) + j(X_{a1} + X_{a2})} \end{aligned} \tag{33}$$

Based on the above analysis, it can be concluded that during an inter-turn short circuit in the excitation winding of the synchronous condenser under balanced grid voltage, the stator parallel current exhibits a second harmonic component that is directly proportional to

F_{d2}. In other words, the magnitude of the parallel current is directly related to the severity of the short circuit.

2.2.3. The Air Gap Magnetic Potential of the Synchronous Condenser under Unbalanced Grid Voltage Conditions without Any Faults Occurring

In the case of unbalanced grid voltage, the induced electromotive force in the two parallel branches of the stator is given by the following expression:

$$\begin{cases} e_1(\alpha_m, t) & = 2N_z k_{w1} \tau l f \Lambda_0 [F_1 \cos(\omega t - \alpha_m - \beta) \\ & \quad + F_2 \cos(\omega t + \alpha_m - \gamma) + \frac{1}{2} I_{f2} N k \cos(3\omega t - \alpha_m)] \\ e_2(\alpha_m, t) & = 2N_z k_{w1} \tau l f \Lambda_0 [F_1 \cos(\omega t - \alpha_m - \beta - \pi) \\ & \quad + F_2 \cos(\omega t + \alpha_m - \gamma + \pi) + \frac{1}{2} I_{f2} N k \cos(3\omega t - \alpha_m - \pi)] \end{cases} \tag{34}$$

At this time, the stator parallel current is given by

$$i_c = -\frac{e_1(\alpha_m, t) + e_2(\alpha_m, t)}{(R_{a1} + R_{a2}) + j(X_{a1} + X_{a2})} = 0 \tag{35}$$

Based on the analysis, it can be concluded that during the operation of the synchronous condenser under unbalanced grid voltage conditions, there are no stator parallel currents induced under normal operation.

2.2.4. The Air Gap Magnetic Flux in the Synchronous Condenser When There Is an Inter-Turn Short Circuit in the Excitation Winding under Unbalanced Grid Voltage

In the presence of an inter-turn short circuit in the excitation winding of the synchronous condenser under unbalanced grid voltage, the induced electromotive forces in the two stator branches can be expressed as follows:

$$\begin{cases} e_1(\alpha_m, t) & = 2N_z k_{w1} \tau l f \Lambda_0 [F_1 \cos(\omega t - \alpha_m - \beta) + F_2 \cos(\omega t + \alpha_m - \gamma) \\ & \quad - F_{d2} \cos(2\omega t - 2\alpha_m) + (\frac{1}{2} I_{f2} N k - \frac{1}{2} F'_{d1}) \cos(3\omega t - \alpha_m) \\ & \quad - \frac{1}{2} F'_{d2} \cos 2\alpha_m - \frac{1}{2} F'_{d2} \cos(4\omega t - 2\alpha_m)] \\ e_2(\alpha_m, t) & = 2N_z k_{w1} \tau l f \Lambda_0 [F_1 \cos(\omega t - \alpha_m - \beta - \pi) + F_2 \cos(\omega t + \alpha_m + \pi - \gamma) \\ & \quad - F_{d2} \cos(2\omega t - 2\alpha_m - 2\pi) + (\frac{1}{2} I_{f2} N k - \frac{1}{2} F'_{d1}) \cos(3\omega t - \alpha_m - \pi) \\ & \quad - \frac{1}{2} F'_{d2} \cos(2\alpha_m - 2\pi) - \frac{1}{2} F'_{d2} \cos(4\omega t - 2\alpha_m - 2\pi)] \end{cases} \tag{36}$$

At this time, the parallel stator current is given by

$$\begin{aligned} i_c & = -\tfrac{e_1(\alpha_m, t) + e_2(\alpha_m, t)}{(R_{a1} + R_{a2}) + j(X_{a1} + X_{a2})} \\ & = \tfrac{4N_z k_{w1} \tau l f \Lambda_0}{(R_{a1} + R_{a2}) + j(X_{a1} + X_{a2})} \\ & \quad [\tfrac{1}{2} F'_{d2} \cos 2\alpha_m + F_{d2} \cos(2\omega t - 2\alpha_m) + \tfrac{1}{2} F'_{d2} \cos(4\omega t - 2\alpha_m)] \end{aligned} \tag{37}$$

Based on the theoretical analysis presented, it can be concluded that the parallel stator current in the synchronous condenser, under the combined conditions of unbalanced grid voltage and inter-turn short circuit in the excitation winding, is predominantly characterized by even harmonics. The magnitude of the parallel stator current is determined by the degree of grid voltage unbalance and the severity of the inter-turn short circuit.

Inter-turn short circuit faults in the excitation winding of the synchronous condenser result in significant modifications to the air gap flux density and parallel stator current. Unbalanced grid voltage conditions further influence these changes in characteristics. Consequently, these distinctive variations can serve as reliable references for fault diagnosis. A comprehensive verification will be conducted through finite element simulation to validate our findings.

3. Simulation Analysis

This paper presents a case study on the TTS-300-2 type novel synchronous condenser at a specific power station. To investigate its behavior, a two-dimensional (2D) finite element simulation model and its corresponding external circuit are developed using Ansys Maxwell 2021 R1 software. This approach enables a comprehensive analysis of the synchronous condensers' performance and facilitates valuable insights into its operation. The utilization of adaptive meshing in condensor modeling offers significant advantages by automatically adjusting the grid density in response to electromagnetic field variations. This adaptive approach enhances the accuracy of simulation results, improves computational efficiency, and optimizes both time and computational resources. In this paper, we employed an adaptive mesh design for the simulation. Details regarding the mesh partition can be found in Table 1. The Finite Element Method is a numerical technique used to solve integral and partial differential equations, offering superior accuracy compared to other analytical analyses. It employs magnetic linearized parameters to accurately model electromagnetic phenomena. In this study, a 2D field-circuit coupled model of the synchronous condenser is developed in ANSYS Maxwell using the Finite Element Method. It is important to note that, for simplicity, the model neglects the effects of skin effects and eddy current losses. The electromagnetic field expression for the electrical machine is represented by Equation (38).

$$\begin{cases} \frac{\partial}{\partial x}(\mu\frac{\partial A}{\partial x}) + \frac{\partial}{\partial y}(\mu\frac{\partial A}{\partial y}) = -J_z \\ A = A_0 \end{cases} \tag{38}$$

where A is the axial components of the magnetic vector potential; A_0 is the magnetic vector potential in the first boundary; J_Z is source current density; μ is material reluctivity.

Table 1. The main information of Mmesh division in 2D finite element model.

Component	Num Elements	Min Edge Length (mm)	Max Edge Length (mm)	Min Element Area (mm^2)	Max Element Area (mm^2)
Stator	13,303	0.0050	0.1044	2.65×10^{-5}	0.00270
Rotor	5745	0.0035	0.0420	1.50×10^{-5}	0.00054
OuterRegion	4914	0.0040	0.0237	1.20×10^{-5}	0.00021
InnerRegion	1836	0.0035	0.0240	1.05×10^{-5}	0.00015
Band	945	0.0073	0.0236	6.24×10^{-5}	0.00020
Shaft	674	0.0079	0.0257	4.09×10^{-5}	0.00023
Stator Coil	23	0.0060	0.0219	4.80×10^{-5}	0.00012
Excitation coil	28	0.0096	0.0224	6.72×10^{-5}	0.00016

Figures 2 and 3 illustrate the model and circuit schematic representations, respectively. The critical parameters of the synchronous condenser are provided in Table 2. In Figure 3, the symbols LPhaseA, LPhaseA1, LPhaseB, LPhaseB1, LPhaseC, and LPhaseC1 represent the windings of the three-phase double parallel branches. The excitation winding is denoted as LField, while the faulty portion responsible for the inter-turn short circuit is referred to as LShortWinding. By manipulating the parameters LField and LShortWinding, precise control over the number of turns in the short-circuited winding can be achieved. Furthermore, the resistances LR and LShortR correspond to LField and LShortWinding, respectively, and must be adjusted accordingly when altering the number of turns.

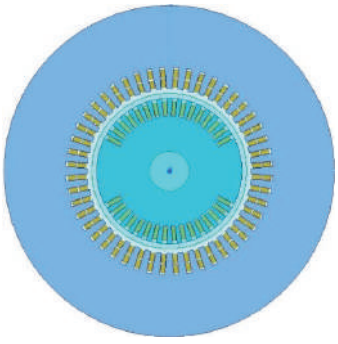

Figure 2. Two-dimensional finite element model of new type synchronous condenser.

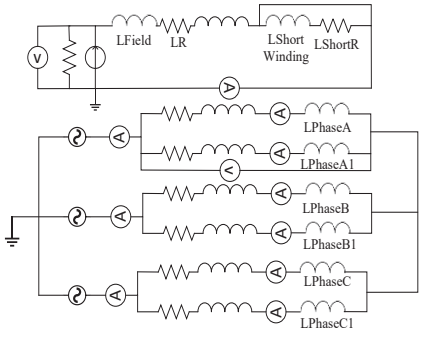

Figure 3. External circuit settings.

Table 2. Parameters of New Synchronous Condenser.

Parameter	Value	Parameter	Value
Rated capacity (Mvar)	300	Number of stator slots	48
Rated exaltation current (A)	1800	Rotor slot number	32
Rated field voltage (V)	407	Stator rated voltage (kV)	20
Number of conductors per slot of stator	2	Stator rated current (A)	8660
Number of turns per slot of rotor	12	Number of parallel branches of stator winding	2
Number of pole-pairs	1	Number of phases	3
Rotor body length (mm)	5950	Inner diameter of stator core (mm)	1240
Air gap length (mm)	70	Frame cushion diameter (mm)	2500
Maximum leading phase operation capability (Mvar)	−200	Rated power factor	0
No-load excitation voltage (V)	137	No-load excitation current (A)	705
Rated speed (rpm)	3000	Rated frequency (Hz)	50

3.1. Model Accuracy Verification

Given the short operating time and the absence of actual on-site fault data for large synchronous condensers, conducting direct short-circuit experiments on-site is impractical. Therefore, to validate the accuracy of the simulation model, simulations were performed under rated operating conditions to analyze the output torque, stator phase voltage, and phase current on the rotor shaft. The rated operating condition of the synchronous condenser refers to its operation at the rated voltage provided in Table 2, carrying the rated load and being connected to the power grid. The specific results are illustrated in Figures 4–6. Additionally, we conducted a comparative analysis between the actual data of stator phase voltage and stator phase current obtained during the synchronous condenser's rated operation and the corresponding simulation data. The detailed results are presented in Table 3.

From the figures, it is evident that the average output torque of the synchronous condenser is zero, which aligns with its expected operational state. Moreover, the phase voltages and currents comply with the rated parameters, and the error falls within an acceptable range. The three-phase currents exhibit symmetry, and there exists a time gap of approximately 5 ms between the stator phase current and the phase voltage. This gap indicates that the stator phase current leads the phase voltage by 90°. These observations confirm the accuracy of the simulation model. By accurately simulating the output torque, stator phase voltage, and phase current under rated conditions, the simulation model has demonstrated its ability to replicate the behavior of the synchronous condenser. Despite the challenges posed by the lack of actual fault data and on-site experiments, the validated simulation results instill confidence in the reliability of the model for further analysis and fault diagnosis.

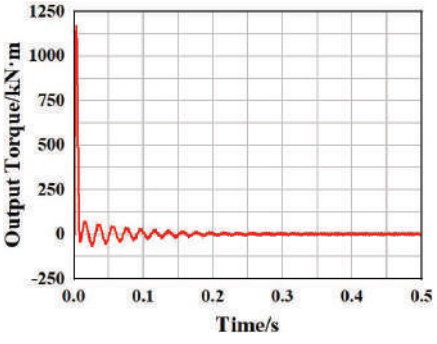

Figure 4. Output torque.

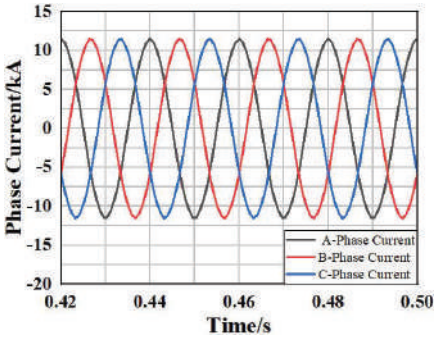

Figure 5. Three-phase current.

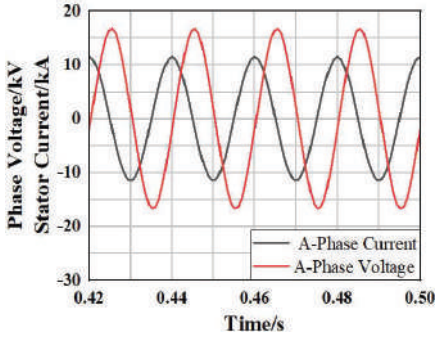

Figure 6. A-phase winding terminal voltage and stator current.

Table 3. Comparison of actual data and simulation data.

Data Type	Actual Data	Simulation Data	Error
Stator phase voltage (kV)	11.547	11.536	0.0954%
Stator phase current (kA)	8.66	8.61	0.5774%

The 2D finite element simulation model of the TTS-300-2 synchronous condenser used in this paper was based on operational parameters primarily extracted from the device's technical manual. Key electrical and structural parameters from Table 2 were accurately applied during the model setup to ensure alignment with the equipment's characteristics. Furthermore, by conducting simulations at the rated voltage and load, we validated the accuracy of torque, phase voltage, and phase current output results under the TTS-300-2 synchronous condenser's rated operating conditions. As a result, the selected parameters effectively mimic the actual device's operational characteristics, guaranteeing the reliability of the simulation analysis.

To simulate the short-circuit of the excitation winding, this study conducted simulation analyses with different numbers of coil turns (1 turn, 3 turns, and 5 turns) short-circuited in the first slot near the large tooth side. In the voltage imbalance simulation, the B-phase and C-phase voltages were maintained at their rated values. In contrast, only the magnitude of the A-phase voltage was adjusted to control the degree of voltage imbalance in the power grid. Specifically, the A-phase voltage values of 96%, 93%, and 90% of the rated voltage were chosen to highlight the simulation results. Due to space constraints, only a partial waveform is presented in this section.

3.2. Analysis of Simulation Results

3.2.1. Analysis of Air Gap Flux Density and Stator Parallel Circulating Current in Faulty Conditions of Synchronous Condenser under Balanced Grid Voltage

- Analysis of Air Gap Magnetic Flux Density

Figure 7a,b depict the analysis results of air gap magnetic flux density under balanced grid voltage with a short circuit fault. Analysis of Figure 7a reveals that a rotor inter-turn short circuit leads to a reduction in air gap magnetic flux density due to a loss of magnetic potential. The severity of the inter-turn short circuit corresponds to a more pronounced decay in the magnetic flux density. Figure 7b demonstrates that in the absence of an inter-turn short circuit, the air gap magnetic flux density is primarily composed of fundamental frequency and odd harmonic components, with only minor influence from slotting effects in the stator and rotor, resulting in a small amount of even harmonic components. The occurrence of a second harmonic in the air gap magnetic density under normal conditions could be attributed to simulation errors resulting in non-uniformity within the air gap magnetic field. However, the presence of an inter-turn short circuit significantly increases the even harmonic magnetic flux density, which intensifies as the severity of the short circuit increases. This observation confirms the accuracy of the derived magnetic field theory.

- Analysis of Parallel Circulation between Stator Branches

Figure 8a,b depict the analysis results of stator parallel branch circulating currents under balanced grid voltage with a short circuit fault. In normal operating conditions, no circulating current or harmonic component is present in the stator parallel branches. However, the occurrence of a short circuit in the excitation winding leads to the generation of circulating currents in the parallel branches, with a predominant presence of even harmonic circulating currents, especially the second harmonic component. Moreover, as the fault severity increases, the amplitude of the harmonic circulating currents also intensifies. This observation confirms the accuracy of the theoretical derivation.

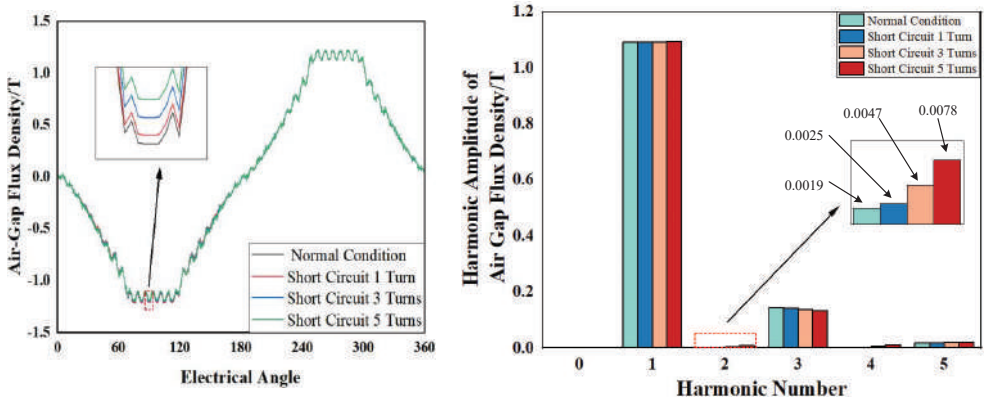

(**a**) (**b**)

Figure 7. (**a**) Air gap flux density of different short circuit degrees under grid voltage balance; (**b**) Harmonic analysis of air gap flux density with different short circuit degrees under grid voltage balance.

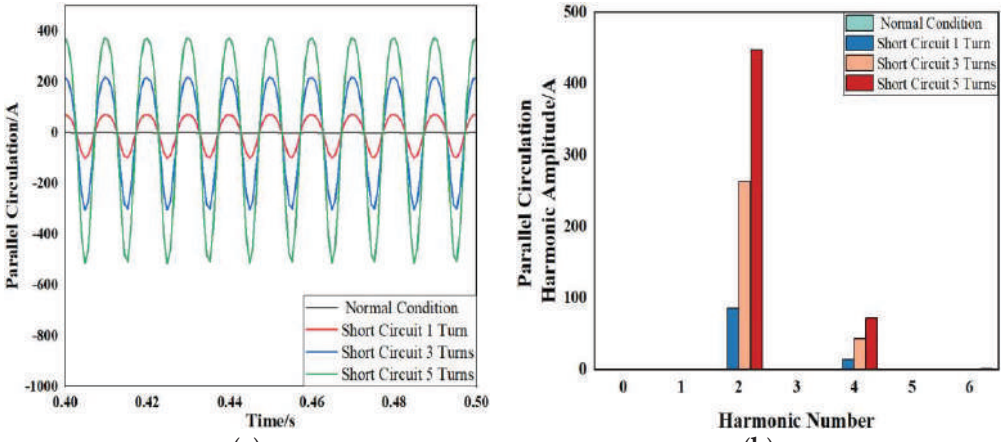

(**a**) (**b**)

Figure 8. (**a**) Stator parallel circulation with different short circuit degrees when grid voltage is balanced; (**b**) Harmonic analysis of stator parallel circulating current with different short circuit degrees under grid voltage balance.

3.2.2. Analysis of Air Gap Flux Density and Stator Parallel Circulation When the Grid Voltage Is Unbalanced and the Synchronous Condenser Is Fault-Free

- Analysis of Air Gap Magnetic Flux Density

Figure 9a,b showcase the analysis results of air gap flux density under the condition of unbalanced grid voltage. Based on the preceding analysis, it is evident that unbalanced grid voltage causes a reduction in air gap flux density, with a greater degree of voltage imbalance resulting in a more substantial loss of air gap flux density. In the presence of voltage imbalance, the amplitude of the fundamental component exhibits a negative correlation with the degree of voltage imbalance. In contrast, the amplitude of the third harmonic component demonstrates a positive correlation. This behavior can be attributed to the induction of twice the frequency current in the excitation winding by the negative-sequence magnetic fields caused by voltage imbalance. Consequently, third-harmonic magnetic fields are superimposed on the existing third harmonic, leading to an amplified amplitude

of the third harmonic and an increased level of magnetic field distortion. According to Equation (14), voltage imbalance in the grid leads to the emergence of third harmonic components in the air gap magnetic field. Consequently, the magnetic field assumes an elliptical shape, deviating from the circular shape predicted by Equation (1). This elliptical magnetic field causes variations in both the amplitude and harmonic content of the air gap magnetic field at different time points, as illustrated in Table 4. Table 4 illustrates the temporal variations of the magnetic field under unbalanced voltage conditions. The primary changes observed are in the amplitude and fundamental amplitude. Although the third harmonic also undergoes changes, its magnitude remains relatively small and inconspicuous due to the low degree of failure.

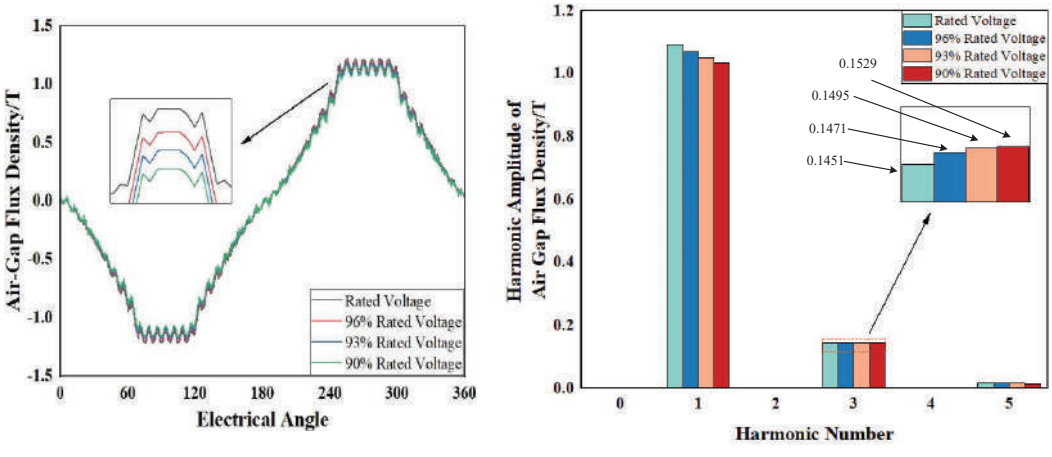

(**a**) (**b**)

Figure 9. (**a**) Fault-free air gap flux density of synchronous condenser under unbalanced grid voltage; (**b**) Harmonic analysis of fault-free air gap flux density of synchronous condenser under unbalanced grid voltage.

Table 4. The values of air gap magnetic flux density at different time instants under 90% rated voltage.

Time/s	Amplitude/T	Fundamental Amplitude/T	Secondary Harmonic Amplitude/T	Third Harmonic Amplitude/T
0.48	1.166	1.034	0.000	0.147
0.485	1.252	1.097	0.000	0.146
0.49	1.191	1.035	0.000	0.147
0.495	1.250	1.097	0.000	0.146
0.5	1.166	1.034	0.000	0.147

- Analysis of Parallel Circulation between Stator Branches

Figure 10 depicts the analysis results of the stator parallel branch current under the condition of unbalanced grid voltage. The theoretical analysis, as indicated by Equations (34) and (35), suggests that the stator parallel branch current remains unaffected by unbalanced grid voltage and maintains a value of 0. However, in the simulation, various factors, such as magnetic saturation and slot effects that occur during the operation of the synchronous condenser, are considered, resulting in a negligible non-zero value for the stator parallel branch current. Although present, the magnitude of this current is minimal and can be disregarded. Thus, during normal operation without faults, the synchronous condenser does not generate any significant stator parallel branch current in unbalanced grid voltage.

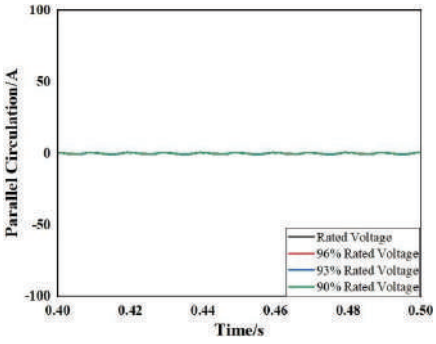

Figure 10. Parallel circulating current of fault-free stator of synchronous condenser under unbalanced grid voltage.

3.2.3. Analysis of Air Gap Magnetic Flux Density and Stator Parallel Circulating Current under Unbalanced Grid Voltage with Excitation Winding Turn-to-Turn Short Circuit

- Analysis of Air Gap Magnetic Flux Density

Figure 11a,b visually represent the air gap magnetic flux density under different degrees of turn-to-turn short circuits in the excitation winding when the grid voltage is unbalanced. Similarly, Figure 12a,b depict the analysis results of air gap magnetic flux density under varying levels of grid voltage imbalance with excitation winding turn-to-turn short circuits. The observations from these figures reveal that unbalanced grid voltage introduces distortions in the air gap magnetic flux density, which are further amplified in the presence of turn-to-turn short circuit faults in the excitation winding. Consequently, there is a significant loss of air gap magnetic flux density. Furthermore, the combined occurrence of faults exacerbates the loss of air gap magnetic flux density compared to a single fault scenario. As the degree of turn-to-turn short circuit in the excitation winding intensifies, even harmonics, particularly the second harmonic, become more prominent in the air gap magnetic flux density. Conversely, grid voltage imbalance primarily affects the fundamental and third harmonic components of the air gap magnetic flux density. The fundamental magnetic flux density decreases while the third harmonic magnetic flux density increases with increasing voltage imbalance. These factors collectively influence the various harmonic components. The simulation results align with the theoretical analysis conducted.

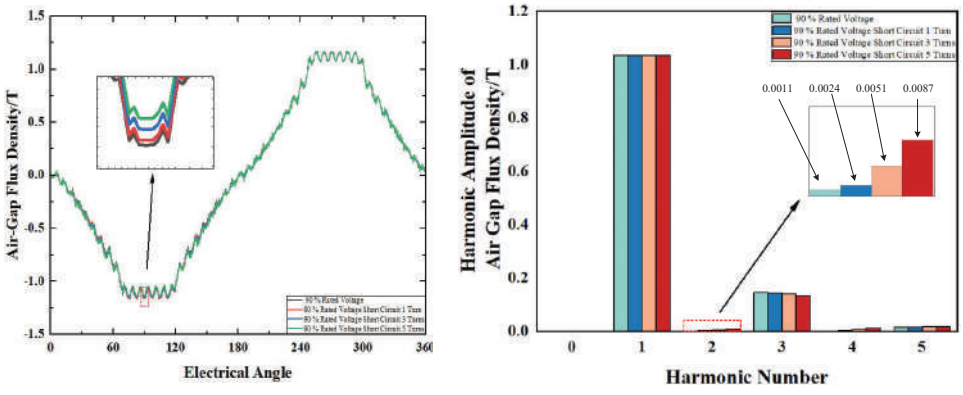

(**a**) (**b**)

Figure 11. (**a**) A total of 90% rated voltage different short circuit turns air gap flux density; (**b**) Air gap flux density harmonic analysis of 90% rated voltage with different short circuit turns.

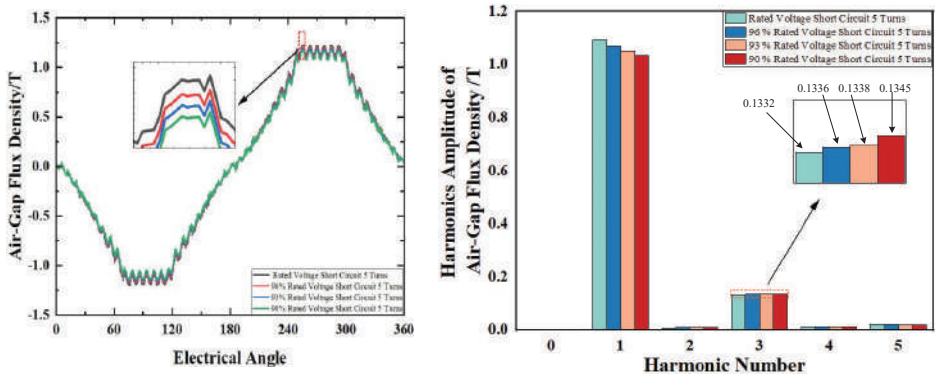

(**a**) (**b**)

Figure 12. (**a**) Air gap flux density of 5-turn short circuit with different voltage balance; (**b**) Harmonic analysis of air gap flux density of 5-turn short circuit with different voltage balance.

- Analysis of Parallel Circulation between Stator Branches

Figure 13a,b display the analysis results of stator parallel currents under different levels of the rotor winding inter-turn short circuits and voltage imbalance in the power grid. Likewise, Figure 14a,b illustrate the analysis results of stator parallel currents under varying levels of the rotor winding inter-turn short circuit and voltage balance in the power grid. Building upon the simulation results and the theoretical analysis discussed earlier, it is evident that voltage imbalance in the power grid does not impact stator parallel currents in the absence of a short circuit fault. However, following the occurrence of the rotor winding inter-turn short circuit, voltage imbalance in the power grid influences the waveform of stator parallel currents. Consequently, in the case of compound faults, the severity of rotor winding inter-turn short circuits and the degree of voltage imbalance in the power grid affect stator parallel currents. As the severity of rotor winding inter-turn short circuits and voltage imbalance in the power grid intensifies, even harmonics, particularly the second and fourth harmonics, become more prominent in the stator parallel currents. Nonetheless, compared to the severity of rotor winding inter-turn short circuits, the influence of voltage imbalance on stator parallel currents is relatively minor and more susceptible to environmental interference during measurement. Therefore, fault diagnosis of the excitation winding inter-turn short circuit should consider multiple fault characteristics to ensure accurate assessment.

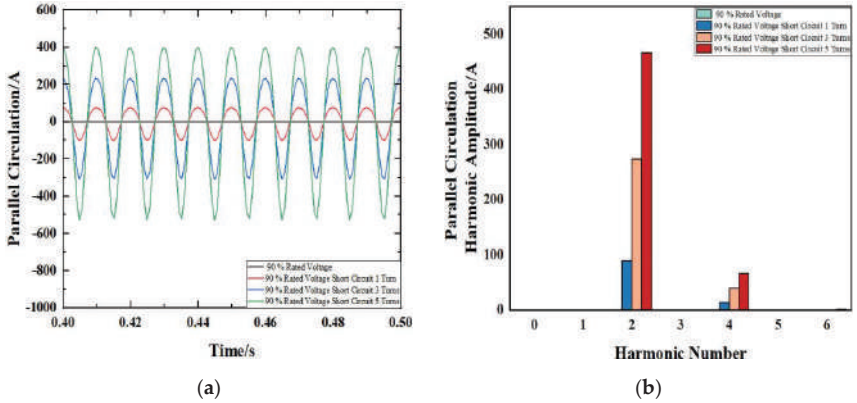

(**a**) (**b**)

Figure 13. (**a**) A total of 90% rated voltage stator parallel circulation with different short circuit turns; (**b**) 90% rated voltage different short circuit turns stator parallel circulation harmonic analysis.

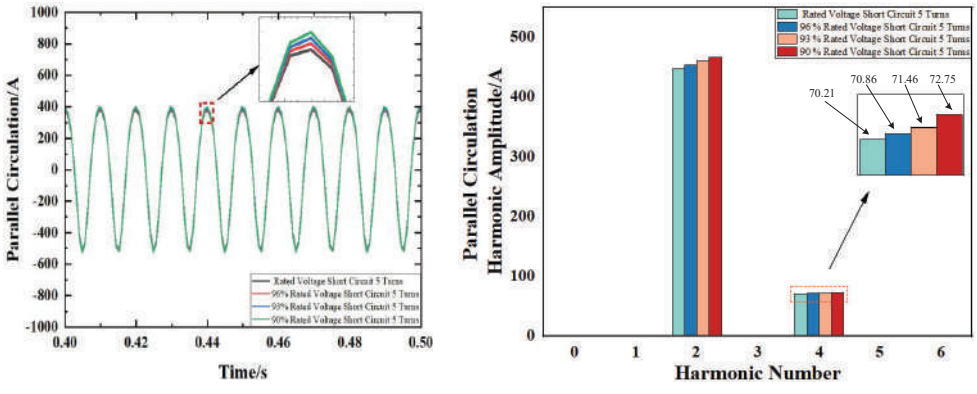

(**a**) (**b**)

Figure 14. (**a**) Five-turn short circuit stator parallel circulation with different voltage balance; (**b**) Harmonic analysis of five-turn short circuit stator parallel circulation with different voltage balance.

4. Conclusions

This paper examines the impact of inter-turn short circuits in the excitation winding and unbalanced grid voltage on the air gap magnetic flux density and circulating current between stator parallel branches in a synchronous condenser. The study presents derived mathematical expressions for these characteristics and validates them through finite element simulation analysis using a TTS-300-2 synchronous condenser as a case study. The simulation results align with the theoretical derivations, leading to the following conclusions:

1. The occurrence of an inter-turn short circuit in the excitation winding distorts the air gap magnetic flux density. This distortion is further amplified by unbalanced grid voltage, resulting in increased losses in the air gap magnetic flux density. When both unbalanced grid voltage and inter-turn short circuit in the excitation winding are present, the loss of air gap magnetic flux density is even more significant compared to the case of a single fault.
2. In the absence of an inter-turn short circuit in the excitation winding, the impact of unbalanced grid voltage on the circulating current between stator parallel branches can be disregarded. However, when compound faults occur, both the degree of unbalanced grid voltage and the severity of the short circuit can result in fluctuations in the circulating current between stator parallel branches, with the severity of the short circuit having a more significant influence on the circulating current.
3. When diagnosing minor faults in a synchronous condenser, relying solely on features such as the even harmonic component of the circulating current may result in inaccurate fault type determination. To enhance fault diagnosis in future research, it is recommended to incorporate electromechanical information fusion, combining mechanical and electrical characteristics, for more reliable results.

By studying the inter-turn short circuit fault in synchronous condensers under unbalanced voltage conditions, this research provides references and guidance for the safe operation of synchronous condensers. It also establishes a foundation for further research on fault diagnosis in synchronous condensers.

Author Contributions: Conceptualization and methodology, J.L. and C.Z.; software, C.Z. and X.H.; writing—original draft preparation, J.L. and C.Z.; writing—review and editing, J.L., C.Z., J.G. and Y.M.; visualization, J.L. and Y.H.; supervision, resources, project administration, J.L. and Y.H.; funding acquisition, J.L. and Y.H. All authors have read and agreed to the published version of the manuscript.

Funding: This study was financially supported by General Projects of National Natural Science Foundation of China, grant number [52177042].

Data Availability Statement: The data could not be shared due to confidentiality.

Conflicts of Interest: The authors declare no conflict of interest.

References

1. Wu, Q.; Song, P.; Shi, Z.; Zhang, L.; Yan, Y.; Yang, Z.; Shao, L.; Qu, T. Development and Testing of a 300-kvar HTS Synchronous Condenser Prototype. *IEEE Trans. Appl. Supercond.* **2021**, *31*, 1–5. [CrossRef]
2. Wang, P.; Liu, X.; Mou, Q.; Gu, W.; Liu, Y. Dynamic Behaviors and Protection Strategy of Synchronous Condenser Integrated Power System Under Non-Full Phase Fault Conditions. *IEEE Access* **2019**, *7*, 104121–104131. [CrossRef]
3. Wei, C.; Li, H.; Wang, X.; Yang, C.; Wang, W.; Cheng, M. Discrimination Method of Interturn Short-Circuit and Resistive Unbalance Faults for Synchronous Condenser. *IEEE Access* **2021**, *9*, 129706–129717. [CrossRef]
4. Zielichowski, M.; Fulczyk, M. Analysis of operating conditions of ground-fault protection schemes for generator stator winding. *IEEE Trans. Energy Convers.* **2003**, *18*, 57–62. [CrossRef]
5. Gaona, C.A.P.; Blázquez, F.; Frías, P.; Redondo, M. A Novel Rotor Ground-Fault-Detection Technique for Synchronous Machines With Static Excitation. *IEEE Trans. Energy Convers.* **2010**, *25*, 965–973. [CrossRef]
6. Streifel, R.; Marks, R.; El-Sharkawi, M.; Kerszenbaum, I. Detection of shorted-turns in the field winding of turbine-generator rotors using novelty detectors-development and field test. *IEEE Trans. Energy Convers.* **1996**, *11*, 312–317. [CrossRef]
7. Gong, X.; Mao, Q.; Wang, C.; Jiang, B.; Sun, H.; Wang, Z. Analysis of abnormal short circuit between turns of generator rotor windings. In Proceedings of the 2020 IEEE 4th Information Technology, Networking, Electronic and Automation Control Conference (ITNEC), Chongqing, China, 12–14 June 2020; pp. 82–86. [CrossRef]
8. Nadarajan, S.; Panda, S.K.; Bhangu, B.; Gupta, A.K. Hybrid Model for Wound-Rotor Synchronous Generator to Detect and Diagnose Turn-to-Turn Short-Circuit Fault in Stator Windings. *IEEE Trans. Ind. Electron.* **2015**, *62*, 1888–1900. [CrossRef]
9. Polishchuk, V.I.; Gnetova, D.A. Diagnostics system improvement of turn-to-turn short circuits of synchronous generator rotor winding. In Proceedings of the 2016 2nd International Conference on Industrial Engineering, Applications and Manufacturing (ICIEAM), Chelyabinsk, Russia, 19–20 May 2016. [CrossRef]
10. Li, J.; Shi, W.; Li, Q. Research on interturn short circuit fault location of rotor winding in synchronous electric machines. In Proceedings of the 2017 20th International Conference on Electrical Machines and Systems (ICEMS), Sydney, Australia, 11–14 August 2017; pp. 1–4. [CrossRef]
11. Meng, Q.; He, Y. Mechanical Response Before and After Rotor Inter-turn Short-circuit Fault on Stator Windings in Synchronous Generator. In Proceedings of the 2018 IEEE Student Conference on Electric Machines and Systems, Huzhou, China, 14–16 December 2018; pp. 1–7. [CrossRef]
12. Xu, M.-X.; He, Y.-L.; Dai, D.-R.; Liu, X.-A.; Zheng, W.-J.; Zhang, W. Effect of Rotor Interturn Short circuit degree and position on Stator Circulating Current inside Parallel Branches in Generators. In Proceedings of the 2021 IEEE 4th Student Conference on Electric Machines and Systems (SCEMS), Huzhou, China, 1–3 December 2021; pp. 1–7. [CrossRef]
13. Xu, G.; Hu, P.; Li, Z.; Zhao, H.; Zhan, Y. Rotor Loss and Temperature Field of Synchronous Condenser Under Single-Phase Short-Circuit Fault Affected by Different Materials of Rotor Slot Wedge. *IEEE Trans. Ind. Appl.* **2022**, *58*, 7171–7180. [CrossRef]
14. Ma, M.; He, P.; Li, Y.; Jiang, M.; Wu, Y. Analysis of the influence of HVDC commutation failure on rotor winding inter-turn short circuit synchronous condenser. *J. Mot. Control* **2021**, *25*, 1–10. [CrossRef]
15. Zhang, Y.; Wei, C.; Lin, Y.; Ma, H.; Chen, Z.; Jiang, M. Rotor fault diagnosis of synchronous condenser based on wavelet model. *Power Eng. Technol.* **2021**, *40*, 179–184. [CrossRef]
16. Chen, Z.; Li, C.; Ma, H.; Zhao, S.; Tang, X. Rotor fault temperature field analysis of large synchronous condenser. *Power Eng. Technol.* **2022**, *41*, 192–198. [CrossRef]
17. Wei, C.; Sun, L.; Wang, W.; Lin, Y.; Tian, W.; Cheng, M. A Fault Diagnosis Strategy for Rotor Windings Inter-turn Short Circuit of Synchronous Condenser. In Proceedings of the 2019 22nd International Conference on Electrical Machines and Systems (ICEMS), Harbin, China, 11–14 August 2019; pp. 1–5. [CrossRef]
18. Novozhilov, A.N.; Akayev, A.M.; Novozhilov, T.A. Currents in the synchronous condenser windings at turn-to-turn fault in the rotor winding. In Proceedings of the 2016 2nd International Conference on Industrial Engineering, Applications and Manufacturing (ICIEAM), Chelyabinsk, Russia, 19–20 May 2016. [CrossRef]
19. Li, J.; Zhang, L.; Shi, W. Fault characteristics of the DFIG rotor inter-turn short circuit considering inherent imbalance and static eccentricity. In Proceedings of the 2015 IEEE Energy Conversion Congress and Exposition (ECCE), Montreal, QC, Canada; 2015; pp. 971–975. [CrossRef]
20. Ye, L. Research on Fault Diagnosis Algorithm of Condenser Based on RBF Neural Network. Master's Thesis, Huazhong University of Science and Technology, Wuhan, China, 2018.
21. Qiu, J. *Dynamics of Electromechanical Analysis*; Science Press: Beijing, China, 1992; pp. 123–199.

energies

MDPI

Article

Microcontroller-Based Embedded System for the Diagnosis of Stator Winding Faults and Unbalanced Supply Voltage of the Induction Motors

Przemyslaw Pietrzak, Piotr Pietrzak and Marcin Wolkiewicz *

Department of Electrical Machines, Drives and Measurements, Wroclaw University of Science and Technology, Wybrzeze Wyspianskiego 27, 50-370 Wroclaw, Poland; przemyslaw.pietrzak@pwr.edu.pl (P.P.); 259942@student.pwr.edu.pl (P.P.)
* Correspondence: marcin.wolkiewicz@pwr.edu.pl

Abstract: Induction motors (IMs) are one of the most widely used motor types in the industry due to their low cost, high reliability, and efficiency. Nevertheless, like other types of AC motors, they are prone to various faults. In this article, a low-cost embedded system based on a microcontroller with the ARM Cortex-M4 core is proposed for the extraction of stator winding faults (interturn short circuits) and an unbalanced supply voltage of the induction motor drive. The voltage induced in the measurement coil by the axial flux was used as a source of diagnostic information. The process of signal measurement, acquisition, and processing using a cost-optimized embedded system (NUCLEO-L476RG), with the potential for industrial deployment, is described in detail. In addition, the analysis of the possibility of distinguishing between interturn short circuits and unbalanced supply voltage was carried out. The effect of motor operating conditions and fault severity on the symptom extraction process was also studied. The results of the experimental research conducted on a 1.5 kW IM confirmed the effectiveness of the developed embedded system in the extraction of these types of faults.

Keywords: induction motor drive; fault diagnosis; stator winding fault; supply voltage unbalance; ARM Cortex; embedded system

Citation: Pietrzak, P.; Pietrzak, P.; Wolkiewicz, M. Microcontroller-Based Embedded System for the Diagnosis of Stator Winding Faults and Unbalanced Supply Voltage of the Induction Motors. *Energies* **2024**, *17*, 387. https://doi.org/10.3390/en17020387

Academic Editors: Moussa Boukhnifer and Larbi Djilali

Received: 14 December 2023
Revised: 10 January 2024
Accepted: 11 January 2024
Published: 12 January 2024

1. Introduction

Induction motors (IMs) are widely used in drive systems due to their low production costs, high reliability, and optimal efficiency. In today's industrial landscape, three-phase IMs dominate and account for over 85% of all electric motor utilization [1]. However, despite the high reliability and durability of IMs, they are prone to various types of faults [2]. The most common faults of IMs include bearings, rotor cages, and stator winding faults. Stator winding faults are highly destructive and account for 36% of the total machine failures for low-voltage machines and 66% for high-voltage machines [3].

Stator winding faults are mainly short circuits caused by damage to the winding insulation due to excessive mechanical, thermal, or electrical stresses. There are different types of short circuits: interturn short circuits (ITSCs), short circuits between the coils in one phase, phase-to-phase short circuits, and phase-to-ground short circuits. Most often, a stator winding fault begins with ITSCs and successively spreads from a single turn to subsequent turns and coils in a very short time, leading to a phase-to-phase or phase-to-ground fault. The rapid propagation of ITSC is caused by the very high current flowing in the shorted circuit. For this reason, early and effective detection of this type of fault is crucial and is still a very important research problem [4].

The efficiency and service life of IMs can also be significantly reduced when operating under unbalanced supply voltage conditions, which is quite common in the industrial field [1]. Such conditions can result from a variety of factors, such as unevenly distributed

single-phase loads, malfunctioning power factor correction equipment in the same power system, and open circuits in the primary distribution system. An unbalanced supply voltage causes the increased heating of the stator winding, higher losses, vibration, and reduced torque output. Most of these negative effects contribute to the shortened lifespan of IMs [5]. Moreover, supply voltage asymmetry can complicate the process of diagnosing stator winding faults, since even a small supply voltage unbalance results in a large current asymmetry, which also occurs due to short circuits [6]. Therefore, detecting and distinguishing between stator winding faults and an unbalanced supply voltage is extremely important to prevent serious failures and increase the reliability and safety of drive systems. It will also contribute to avoiding motor operation with reduced efficiency, which is crucial to reduce energy consumption and care for the environment.

The requirements for the safety and reliability of modern drive systems are increasing every year. This is due in part to the increasing electrification in many industries and the drive to maximize the lifetime of the equipment. Early detection of a fault can also make it possible to plan motor overhauls accordingly, which will translate into lower repair costs, shorter delays, and reduced potential production losses. For this reason, new diagnostic methods are sought that can be used to diagnose faults at a very early stage of their propagation.

Over the years, several methods for diagnosing IM stator failure have been developed [7–11]. These methods are based on various types of diagnostic signals, such as input voltage [12], stator phase current [13], temperature [14], active and reactive power [15], vibration [16], and axial flux [17]. To extract the fault symptoms from these signals, signal processing methods can be used. Among the most popular and highly effective is the spectral analysis of the signal using the Fast Fourier Transform (FFT). Methods that perform the time-frequency analysis, such as the Short-Time Fourier Transform (STFT) or Continuous Wavelet Transform (CWT) [18], are also attractive in the AC motors stator winding fault diagnosis field. Automation of the AC motors stator winding fault detection and classification process in recent years has most often been implemented using a variety of artificial intelligence techniques [19], such as machine learning algorithms [20,21] and deep learning (DL) [22]. When it comes to computerized diagnostic systems, the fastest growing area in recent years is the application of DL, especially convolutional neural networks (CNN). They are not only applied for fault detection and classification [23] but also for predictive maintenance and remaining useful time estimation [24].

Detection of an unbalanced supply voltage is dominated by methods based on voltage and current signals. The combination of the wavelet transform and principal component analysis of the mains current signal for the detection of unbalanced supply voltage, automated with a support vector machine model, is presented in [25]. The diagnosis and discrimination of the ITSC and unbalanced supply voltage fault method, based on the analysis of the ratio of the third harmonic to the fundamental FFT magnitude component of the three-phase stator line current and voltage, is presented in [26]. An effective approach for the detection of the supply voltage unbalance condition in IM drives, based on a data mining process using the amplitude of the second harmonic of the stator current zero crossing instants as a supply voltage unbalance indicator, is presented in [27]. The online detection method of the unbalanced supply voltage condition, by monitoring a pertinent indicator calculated using the voltage symmetrical components, is shown in [28].

Nevertheless, most of the methods proposed in the literature for stator winding and unbalanced supply voltage diagnosis have been described based on the results obtained using high-end data acquisition (DAQ) equipment and software, such as LabVIEW or MATLAB & SIMULINK [12,27,28], the price of which often exceeds the cost of the machine being monitored. For this reason, the real potential of their industrial deployment is diminishing, as there is no detailed description of the possibilities of low-cost hardware implementation. In this article, special attention is paid to analyzing the possibilities and describing how to apply an embedded system based on a low-budget microcontroller

with an ARM Cortex-M core to extract the symptoms of the SI stator winding faults and unbalanced supply voltage.

Embedded systems are used in most modern electronic devices and are a key component of them. An embedded system is a type of system that is designed to perform specific functions, usually in real-time. In recent years, embedded systems that utilize microcontrollers have been the most common. This allows the achievement of a high degree of compactness, responding to increasing demands for the greatest possible miniaturization of devices. The range of applications of embedded systems is very wide, from special-purpose on-board systems, and inverters powering electric motors, to household appliances, HVAC, and many other technical objects [29].

Microcontrollers are small single-chip microcomputers. They are equipped with a variety of peripherals, which include analog-to-digital converters (ADCs), digital-to-analog converters (DACs), comparators, counters, communication interfaces, as well as RAM and Flash memory. In recent years, microcontrollers with the ARM Cortex-M core have been particularly popular. ARM Cortex-M processors are currently one of the best choices for a wide range of applications. In the fourth quarter of 2020, ARM reported a record 4.4 billion chips shipped with Cortex-M processors, confirming their very high popularity [30]. The Cortex M family is a subset of the Cortex family cores, which in turn is a subset of the ARM architecture. Semiconductor manufacturers implement selected versions of the cores, equipping them with peripherals and memory to produce a ready-to-use microcontroller. ARM Cortex-M-based microcontrollers are characterized by high reliability, high performance, and affordability [31]

Currently, there is a noticeable lack of research in the literature that deals with embedded, low-cost implementation of AC motor fault diagnosis methods. In [32], the Arduino board-based system is developed to monitor parameters such as speed, temperature, current, and voltage of the one-phase IM. Authors believe that using these parameters, faults such as over-voltage, over-current, overload, and excessive heating can be detected. In [33], the 8-bit PIC16F877A microcontroller-based system is developed and programmed in C++ language for the detection of under-voltage, over-voltage, over-current, and line-to-ground faults of one-phase IMs. The STM32F4V11VET microcontroller-based fault diagnosis system is proposed in [34] for the detection of the faults of three-phase IMs. This method is based on the stator phase current signals measured using MCR1101-20-5 (ACEINNA, Phoenix, USA) current sensors. It is a promising AI-driven method but requires the current measurement in each of the three phases and it is not strictly defined; the kind of faults the system can detect (broken bearings and misalignment) are mentioned. There are also commercial condition monitoring solutions available on the market that are characterized by a relatively low cost, such as the VB300 G-Force datalogger by EXTECH Instruments, which records a 3-axis shock and vibration and allows the detection of mechanical damage to IMs based on the vibration signal. Nevertheless, it also requires additional PC software. No work has been found that describes a low-cost embedded implementation of an IM stator winding fault and unbalanced supply voltage diagnosis method based on the measurement of the voltage induced by the axial flux.

In this paper, the feasibility of using a low-cost ARM Cortex-M4 core microcontroller (STM32L476RG) to extract the symptoms of ITSCs in IM stator winding and supply voltage unbalance, based on the voltage signal induced in the measuring coil by the axial flux, is discussed. A NUCLEO-L476RG module with a 32-bit STM32L476RG microcontroller (STMicroelectronics, Plan-les-Ouates, Geneva, Switzerland) is used to measure and acquire the diagnostic signal. The method of measuring the diagnostic signal, its acquisitions, the components of the prepared system, and the necessary configuration are presented in detail. Experimental tests were carried out, the results of which confirmed the feasibility of using an embedded system based on a microcontroller with an ARM Cortex-M4 core to extract symptoms of SI stator winding faults and supply voltage unbalance.

The main theoretical and practical contributions of this research are as follows:

(1) An analysis of the possibility of using and the proposal of the concept of an embedded fault diagnosis system based on a low-cost ARM Cortex-M4 core microcontroller to extract the symptoms of IM stator winding faults and unbalanced supply voltage, including the comparison of the results with a high-end solution;
(2) A detailed description of the process of setting up diagnostic signal measurement and acquisition using low-cost microcontrollers, which may serve as a guide for various embedded system applications;
(3) A detailed analysis of the effect of an ITSC in the stator winding and an unbalanced supply voltage of the IM drive on the waveform of the voltage induced in the measuring coil by the axial flux;
(4) A detailed analysis of the effect of an ITSC in the stator winding and an unbalanced supply voltage of the IM drive on the FFT spectrum of the voltage induced in the measuring coil by the axial flux;
(5) An analysis of the possibility of distinguishing between ITSC in the stator winding and an unbalanced supply voltage of the IM drive based on symptoms characteristic of these abnormal conditions;
(6) A proposal for future research and plans to improve and develop the embedded diagnostic system, including reference to current trends related to the Industry 4.0 paradigm.

The rest of the article is organized as follows: Section 2 describes the key parameters of the NUCLEO-L476RG evaluation board, STM32L476RG microcontroller, and motor test bench; Section 3 presents the configuration of the data acquisition system; Then, the results of the ITSC and unbalanced supply voltage symptom extraction based on the voltage inducted by axial flux are presented and discussed. This section also outlines key discoveries and plans for future research; and finally, Section 5 concludes the paper.

2. Experimental Setup

2.1. Characteristics of the Development Board and Microcontroller Used

The development board used in the scope of this research was the NUCLEO-L476RG evaluation board (Figure 1a). It is one of the most popular evaluation boards by STMicroelectronics. The STM32 NUCLEO-L476RG (STMicroelectronics, Plan-les-Ouates, Geneva, Switzerland) is a low-cost and easy-to-use development platform used in flexible prototyping to quickly develop projects based on STM32 microcontrollers. The NUCLEO-L476RG is designed around the 32-bit STM32L476RG microcontroller in a 64-pin LQFP package.

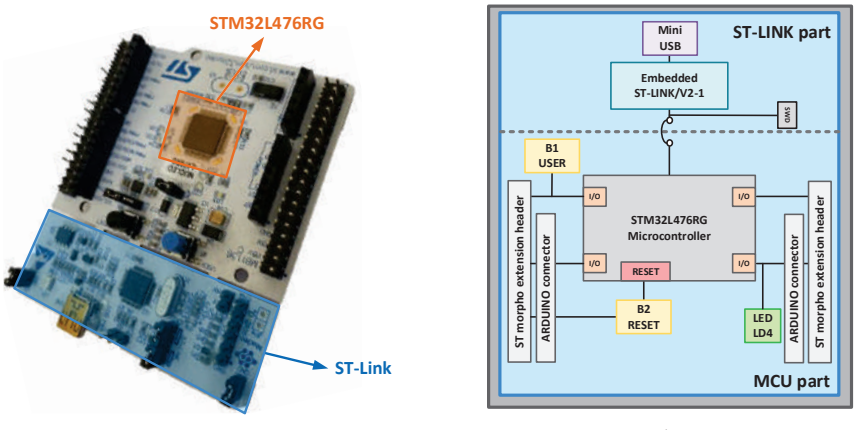

Figure 1. (**a**) Real view and (**b**) simplified hardware block diagram of the NUCLEO-L476RG evaluation board.

The STM32L476RG microcontroller is based on the ARM Cortex-M4 core that operates at a frequency of up to 80 MHz. This microcontroller embeds 1 MB of Flash memory and 128 kB of SRAM memory. The ARM Cortex-M4 core features a single precision Floating Point Unit (FPU) and a Memory Protection Unit (MPU). Its design also features 3 ADC modules and 2 DAC modules with 12-bit resolution. The key parameters of this microcontroller are grouped in Table 1.

Table 1. Key parameters of the STM32L476RG microcontroller.

Parameter	Value
Core	ARM Cortex-M4 (32-bit)
Operating clock frequency	Up to 80 MHz
Flash memory	1 MB
SRAM memory	128 kB
DMA	14-channel
Key communication interfaces	USB OTG, 3× I2C, 5× USART, 3× SPI, CAN
ADC	3 × 12-bit
DAC	2 × 12-bit
Comparators	2× ultra-low power

The NUCLEO-L476RG evaluation board is equipped with ST-Link/V2, which allows flash programming and microcontroller debugging. The power supply of the module is flexible, being possible both via USB and from an external voltage source (3.3 V, 5 V, and 7–12 V). There are also three built-in LEDs on the PCB, which indicate USB communication (LD1), can be programmed by the user (LD2), and indicate the module's power supply (LD3). The ST morpho extension pin headers and ARDUINO connectors are also available on the board for full access to all STM32 inputs and outputs. The simplified hardware block diagram of the board is presented in Figure 1b. A detailed specification of the NUCLEO-L476RG is available on the manufacturer's website [35].

2.2. Motor Test Bench

Experimental tests were carried out on a specially prepared test bench consisting of an IM with a rated power of 1.5 kW (by Indukta) and a DC motor that provided the load torque. The real view of the motor test bench is presented in Figure 2a. The rated parameters of the IM under test are grouped in Table 2. The IM was powered directly from the three-phase grid. The stator winding of the IM under test was wound in such a way that its design allowed for the physical modeling of ITSCs with a certain number of turns. Each phase of the IM under analysis consisted of a coil with 312 turns. During the tests, a maximum of 8 turns were short-circuited, representing 2.6% of all turns in one phase. The schematic diagram of the phase terminals led out to the board of this winding is shown in Figure 2b. The numbers above each piece of winding, visible in Figure 2, are the number of turns that correspond to the taps derived from the winding. The ITSCs were carried out without additional current limiting resistance in the shorted circuit.

The diagnostic signal, the induced voltage in the measurement coil, was measured not only by the NUCLEO-L476RG module described in the previous section but also in parallel for comparison purposes by a high-end DAQ card by National Instruments (DAQ NI PXIe-4492). The DAQ card was placed in an NI PXI 1082 industrial computer. The price of the PXIe-4492 DAQ card was, at the time of article publication, more than 300 times higher (≈USD 8240) compared to the price of the NUCLEO-L476RG board (≈USD 25). Moreover, the PXIe-4492 has an ADC module with a significantly higher resolution (24-bit) compared to the NUCLEO's 12-bit ADC.

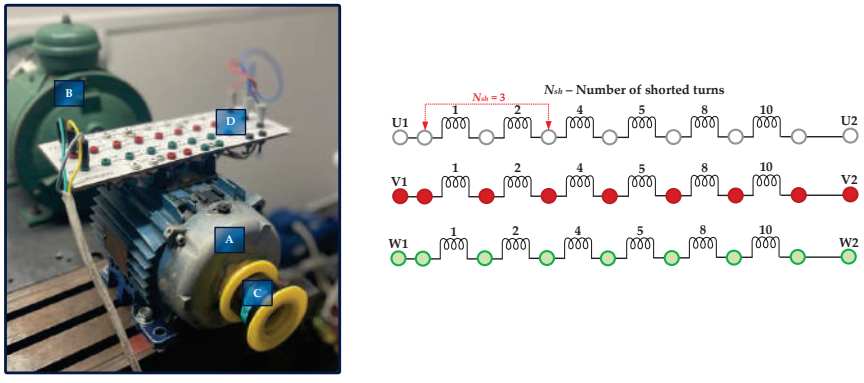

(a) (b)

Figure 2. (**a**) Real view of the motor test bench: A—SI under test, B—DC motor (load), C—measurement coil, and D—terminal board; and (**b**) diagram of the derived stator winding terminals.

Table 2. Rated parameters of the tested IM.

Name of the Parameter	Symbol	Units	
Power	P_N	1500	[W]
Torque	T_N	10.16	[Nm]
Speed	n_N	1410	[rpm]
Stator phase voltage	U_{sN}	230	V
Stator current	I_{sN}	3.5	[A]
Frequency	f_{sN}	50	[Hz]
Pole pairs number	p_p	2	[-]
Number of stator turns	N_{st}	312	[-]

As presented in Figure 2a, the measurement coil was mounted coaxially with the shaft. Proper mounting of the measurement coil is necessary to apply the proposed method in practice. The design of the used coil and its location coaxially with the shaft does not allow the installation of the cooling fan. Nevertheless, if a fan is necessary, the measurement coil can also be placed on the top or the side of the motor housing. In this experiment, a measurement coil with 300 turns and a DNE copper winding wire cross-section equal to 0.35 mm^2 was used.

2.3. Details of the Developed Microcontroller-Based Fault Diagnosis System

Since preliminary tests have shown that the value of the voltage induced in the coil by the axial flux as a result of the ITSC in the IM stator winding is in the order of mV, to obtain the best possible resolution of the measurement, the signal of this voltage was amplified using an ultra-precise INA241A2 amplifier from Texas Instruments (Dallas, TX, USA). This amplifier has a gain of 20 V/V, a maximum gain error of ±0.01%, a maximum voltage offset error of ±10 µV, and a CMRR (Common Mode Rejection Ratio) of 166 dB (typically). The amplifier was powered directly from the NUCLEO-L476RG module with a voltage of 3.3 V.

The input and output pins of the INA241A2 amplifier, a diagram of its internal connections, and the manufacturer's (Texas Instruments) recommended configuration, as well as a simplified schematic diagram and a photo of the whole prepared system, are shown in Figure 3.

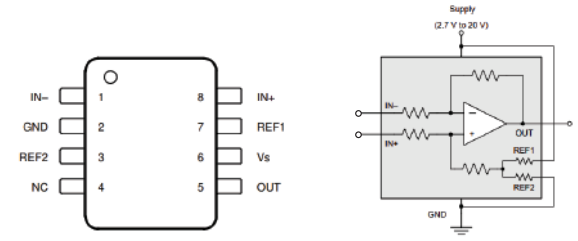

(a) (b)

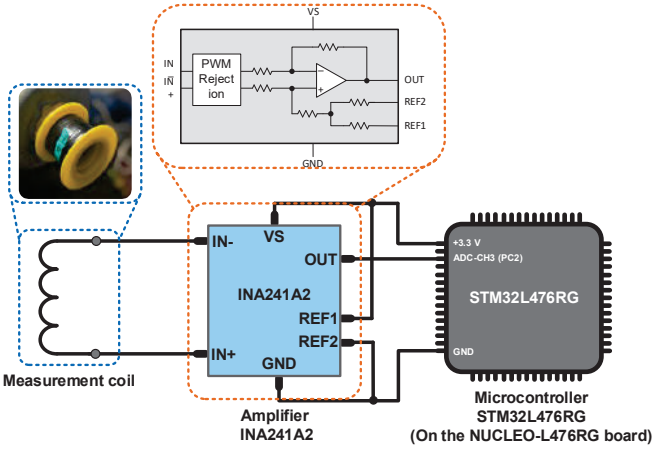

(c)

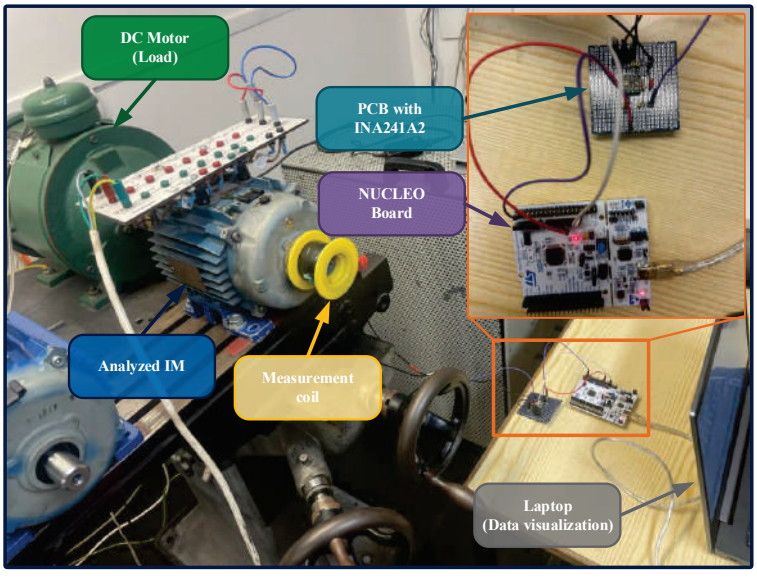

(d)

Figure 3. (**a**) Input and output pins of the INA241A2 amplifier, (**b**) a diagram of its internal connections and the manufacturer's recommended configuration, (**c**) a simplified schematic, and (**d**) a photo of the whole system.

The INA241A amplifier, as shown in Figure 3, is located between the STM32L476RG microcontroller and the measurement coil. The IN− and IN+ inputs to which the measurement coil is connected are characterized by a differential mode operation. The REF1 and REF2 pins are reference pins connected to the amplifier supply voltage and GND. The OUT pin is the output voltage, which is connected to the PC3 pin of the microcontroller, which is programmed to operate in ADC mode; it recognizes the conversion of the analog voltage signal induced in the measuring coil into a digital signal. In future research, it is planned to design a customized PCB, which will contain both the microcontroller and the amplifier on a single board. The laptop shown in the lower right corner was needed only for data visualization purposes. In the final system implementation, all functions could be performed by an embedded system that would indicate the information about the stator winding and supply voltage symmetry condition.

The application responsible for the data acquisition and processing was written using the C programming language. Programming and debugging were performed in the STM32CubeIDE environment. Visualization of the values of variables from the microcontroller's memory during real-time operation was carried out using STMStudio (v3.6.0) software.

3. Configuration and Verification of the Data Acquisition Process

3.1. Configuration of the Measurement and Data Acquisition Process

To enable the effective extraction of the IM stator winding fault symptoms from the diagnostic signal, it is necessary to properly configure the measurement and signal acquisition process that is performed by the microcontroller. The microcontroller's pin configuration was done using the Integrated Development Environment (IDE) developed by STMicroelectronics (STM32CubeIDE). STM32CubeIDE is an advanced programming platform for C/C++ languages with the ability to recognize peripheral configuration, code generation, compilation, and debugging for STM32 microcontrollers.

The key task at the stage of preparing the measurement and acquisition of the diagnostic signal is to correctly configure the microcontroller pin that will be associated with the ADC module, which converts the analog voltage signal induced in the measurement coil into a digital signal. Pin two of port C (PC2) was configured as the input of the ADC1 module (channel 3), operated in a single-ended operation mode.

To set the sampling frequency, f_p, when using the microcontroller-based embedded system, it is necessary to configure the timer accordingly so that it generates a cyclic interrupt every specified time, during which the voltage measurement (sampling) will be performed. Cyclic interruptions are used to trigger actions that need to be called at the appropriate frequency. To determine at what frequency the interrupt-generating timer will count, it is necessary to check the microcontroller's specification to verify which bus provides the clocking to the timer and the clocking frequency. In this project, a 16-bit TIM6 timer was used. It was located on the APB1 bus and clocked at 80 MHz. Obtaining this information allows the TIM6 to be appropriately configured for measurement and signal acquisition.

The TIM6 counts from 0 to the value defined in the AutoReload Register (ARR), then generates an interrupt, and resets the counter register to 0 (after the defined time). The frequency of the interrupt triggering (that is the sampling frequency) f_p can be calculated according to the following equation:

$$f_p = \frac{f_{CLK\_CNT}}{TIM\_ARR + 1'}, \tag{1}$$

where f_{CLK_CNT} is the clock frequency of the bus on which the timer is located, and *TIM_ARR* is the value written in the ARR register.

The f_{CLK_CNT} equals 80 MHz, while 4000 Hz was taken as the desired value of the interrupt trigger frequency (corresponding to the sampling frequency). Hence, the value written in the ARR register is as follows:

$$TIM\_ARR = \frac{f_{CLK\_CNT}}{f_p} - 1 = \frac{80 \cdot 10^6 \text{ Hz}}{4000 \text{ Hz}} - 1 = 19,999. \quad (2)$$

3.2. Verification of the Measurement and Data Acquisition Process

After configuring the peripherals required for the project, it is necessary to verify the correctness of the measurement and signal acquisition before proceeding with the tests. In the first step, it was verified if the TIM6 settings were configured correctly. In the timer interrupt handler function (*HAL_TIM_PeriodElapsedCallback*()), an additional function was added to negate the state of one of the test pins, which was configured as a general-purpose output (GPIO Output). Figure 4 shows the voltage waveform at the output of the test pin recorded using a GW INSTEK MDO-2102A (Montclair, CA, USA) digital oscilloscope. As can be seen, the state change at the output of this pin (state 0 corresponded to ground level, while state 1 corresponded to 3.3 V) occurred every 250 µs. This confirms the correct configuration of TIM6 and corresponds to a frequency of 4 kHz. The interrupt service function will be called to measure (sample) the value measured by the ADC module.

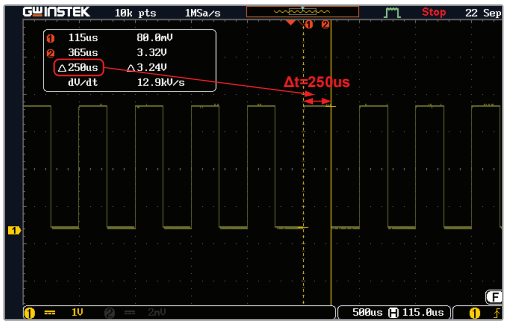

Figure 4. The voltage waveform at the output of the test pin was recorded using a GW INSTEK MDO-2102A digital oscilloscope.

The INA241A2 amplifier (Dallas, TX, USA), which is used in the measurement circuit, not only amplifies the input voltage 20 times but also adds an offset (offset) equal to half the value of its supply voltage. In the case of the supply voltage V_s = 3.3 V, this offset equals 1.65 V. This offset allows the ADC module to measure negative voltages. The output voltage of the INA241A2 amplifier in the absence of input voltage and supply voltage V_s = 3.3 V is shown in Figure 5.

As expected, the value at the output of the amplifier, when there was no input signal connected, was close to 1.65 V. In the next step, the results of signal acquisition recognized by the internal ADC module of the STM32L476RG microcontroller were verified. The waveform of the read-out digital signal after converting the analog voltage signal at the amplifier output by the ADC module (variable *ui16RawADCResult*) is shown in Figure 6a. To convert the raw ADC value to voltage, it is necessary to perform the following calculations [36]:

$$V_{ADC} = \frac{V_{REF+}}{FULL\_SCALE} \cdot ADC\_DATA, \quad (3)$$

where V_{ADC} is the actual voltage measured by the ADC module, V_{REF+} is the reference voltage value of the ADC module equal to 3.3 V, *ADC_DATA* is the digital value converted by the ADC module, and *FULL_SCALE* is the maximum digital value of the ADC output equal to $FULL\_SCALE_{12\text{-}bit}$ = ($2^{12} - 1$) = 4095 for an ADC with 12-bit resolution.

Figure 5. The output voltage of the INA241A2 amplifier in the absence of input voltage (amplifier supply voltage V_s = 3.3 V).

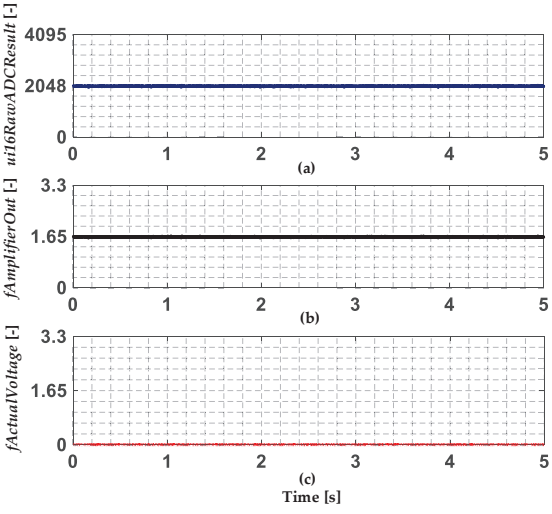

Figure 6. The waveform of (**a**) the measured digital signal after converting the analog voltage signal at the amplifier output by the ADC module (*ui16RawADCResult*), (**b**) the voltage after converting the raw ADC value (*fAmplifierOutput*), and (**c**) the actual amplifier output voltage after offset and gain compensation (*fActualVoltage*).

Figure 6b shows the waveform of the *fAmplifierOut* variable carrying the information about the voltage after converting the raw ADC value according to Equation (3). This value coincides with the waveform recorded using a digital oscilloscope (Figure 5). After taking into account the offset compensation and gain introduced by the amplifier, the waveform of the actual voltage at the output of the amplifier (variable *fActualVoltage*) is shown in Figure 6c. The value was close to 0, confirming that the measurement and acquisition configuration were correct in the absence of input voltage.

The final step in verifying the correct configuration of the ADC module was to measure a sinusoidal voltage signal with an amplitude of 50 mV and a frequency of 50 Hz, generated using the NI myDAQ card and the NI ELVISmx Function Generator environment. The waveform of this signal, recorded using a digital oscilloscope, is shown in Figure 7a, while the measurement at the output of the amplifier by the ADC module of the STM32L476RG microcontroller, after offset and gain compensation ($\times$20), is shown in Figure 7b. The FFT amplitude spectrum is shown in Figure 8. The frequency range of the spectrum includes frequencies from 0 to 2000 Hz, which is due to the adopted sampling frequency of 4000 Hz.

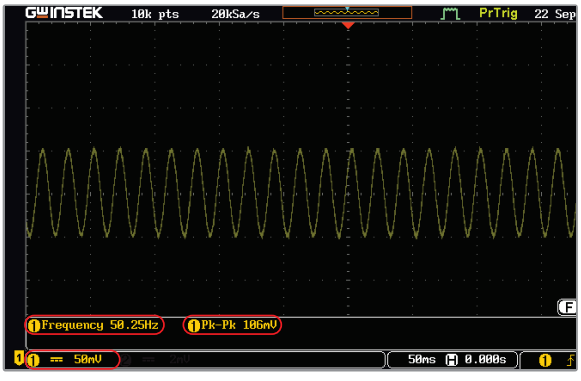

(**a**)

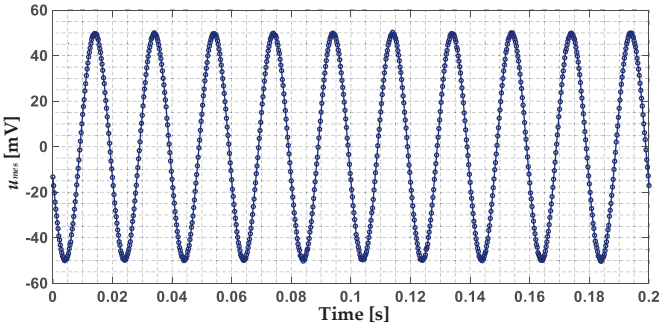

(**b**)

Figure 7. (**a**) The waveform of a sinusoidal voltage signal with an amplitude of 50 mV and a frequency of 50 Hz generated using the NI myDAQ card and the NI ELVISmx Function Generator environment (recorded using a digital oscilloscope), and (**b**) the waveform of the generated signal after conversion and offset compensation measured by the ADC module of the STM32L476RG microcontroller.

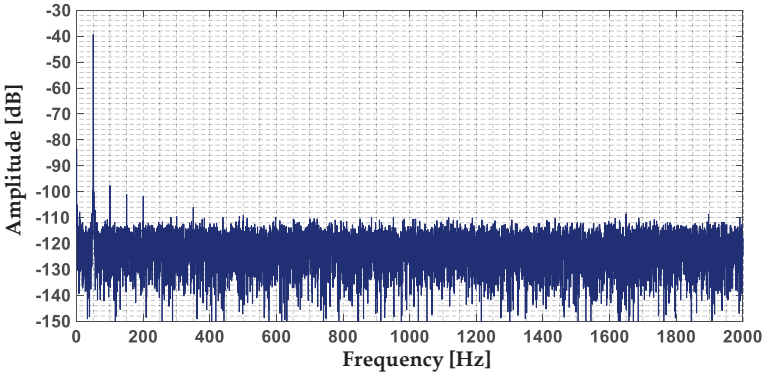

Figure 8. The FFT spectrum of a sinusoidal voltage signal with an amplitude of 50 mV and a frequency of 50 Hz measured by the ADC module of the STM32L476RG microcontroller.

Based on the analysis of the results of the conducted verification of the reliability of the measurement and signal acquisition, it was concluded that the configuration was carried out correctly and the noise level was at a satisfactorily low level of about −125 dB.

4. ITSC and Unbalanced Supply Voltage Symptom Extraction Based on the Voltage Inducted by Axial Flux

Due to the limited accuracy of the technological processing of machine components, IMs are characterized by the presence of certain asymmetries in electrical or magnetic circuits. The effect of these imperfections is the occurrence of leakage fluxes, the value of which will depend on the level of asymmetry of the motor. Since the axial flux finds its source in the currents flowing through the motor windings, faults to the electrical circuits will also be reflected in this signal. In the case of an undamaged motor, the axial flux will have a very low value, close to zero [37]. In the following subsections, the effect of the stator winding faults and unbalanced supply voltage on the waveform of the voltage inducted by the axial flux, as well as on its FFT spectrum, will be analyzed. This will allow the assessment of the possibility of extracting the symptoms of these abnormal motor conditions using a low-cost system.

4.1. Stator Winding Faults (ITSCs)

To verify the validity of the measurement performed with the NUCLEO-L476RG evaluation board, the initial results were compared with those obtained with a high-end NI data acquisition board (DAQ), which has a built-in ADC module with a resolution as high as 24 bits. Figure 9a shows a comparison of the waveform of the induced voltage in the measurement coil by axial flux, u_{mc}, for an unloaded IM with undamaged stator winding (N_{sh} = 0, N_{sh}—number of shorted turns), measured using the NUCLEO-L476RG module and the DAQ NI PXI-4492 card. As expected, based on the analysis of these waveforms, the value of the induced voltage in the absence of a stator winding fault was very low; the signal amplitude was about 4 mV. The results obtained for the DAQ NI PXI-4492 measurement card and the STM32L476RG microcontroller were similar. Figure 9b shows a comparison of the u_{mc} waveform for the same drive system operating conditions but with 8 shorted turns (N_{sh} = 8) in the IM stator winding. As a result of the damage to the stator winding, the value of the amplitude of the voltage induced by the axial flux increased by about 10 times. Again, both the measurement and data acquisition methods yielded similar results, confirming the correctness of the measurement and signal acquisition performed by the developed low-lost system.

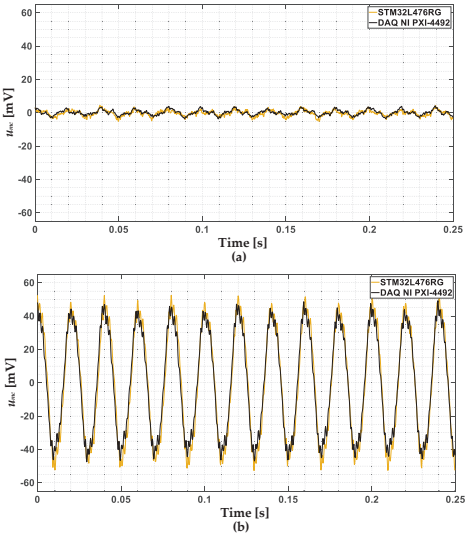

Figure 9. The waveform of the u_{mc} measured using the NUCLEO-L476RG module and DAQ NI PXI-4492 measurement card for an unloaded motor and (**a**) N_{sh} = 0, (**b**) N_{sh} = 8.

The effect of the stator winding fault can also be seen in the FFT spectrum of the induced voltage signal as an increase of the selected characteristic frequency components. These harmonics are described by the following equation [37]:

$$f_{sp} = kf_s \pm n\frac{1-s}{p_b} = kf_s \pm nf_r, \quad (4)$$

where:

f_s—fundamental frequency of the supply voltage;
f_r—rotational frequency;
p_p—number of pole pairs;
s—slip;
n—1, 3, 5, . . ., $2p_p - 1$;
k—consecutive positive integers (1, 2, 3 . . .).

Figure 10 shows the FFT spectra of the u_{mc} measured using the NUCLEO-L476RG module and the DAQ NI PXI-4492 measurement card for an unloaded motor and N_{sh} = 0 (Figure 10a) and N_{sh} = 8 (Figure 10b). Based on the analysis of these figures, it was concluded that the amplitudes of the harmonics seen in these spectra were similar for both methods of measurement and signal acquisition. The spectrum when the signal was measured with the DAQ NI PXI-4492 card had a lower noise level (by about 30 dB). The higher noise level for the NUCLEO-L476RG did not adversely affect the analysis of the harmonic values. The spectra also show selected stator winding fault-specific frequency components, calculated according to Equation (4). By comparing the spectra shown in Figure 10a,b, it is possible to find the largest increase in the harmonic corresponding to the frequency of the supply voltage (f_s = 50 Hz) as a result of the damage. The results confirmed the correctness of the measurement carried out using the NUCLEO-L476RG. Therefore, further detailed analysis will be performed only for the proposed solution based on the embedded system.

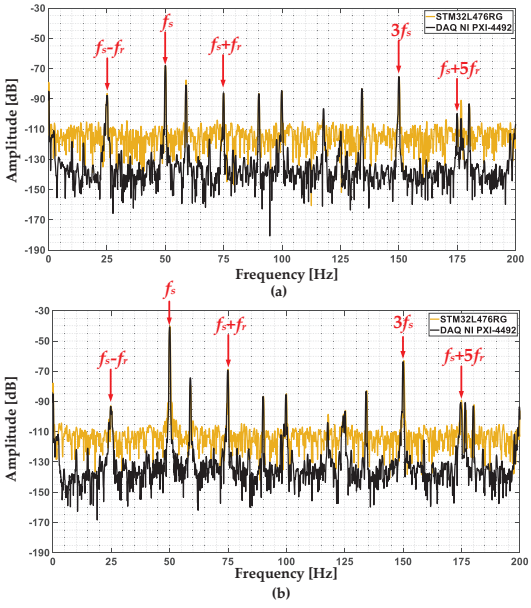

Figure 10. The FFT spectrum of the u_{mc} measured using the NUCLEO-L476RG module and DAQ NI PXI-4492 card for an unloaded motor and (**a**) N_{sh} = 0, (**b**) N_{sh} = 8 ($f_s = f_{sN}$ = 50 Hz, f_r = 24.9 Hz).

Figure 11a shows the waveform of the u_{mc} for the measurement using the NUCLEO-L476RG module, the motor loaded with the rated torque ($T_L = T_N$, T_L—load torque.), and different severities of the stator winding fault ($N_{sh} = 0$, $N_{sh} = 2$, $N_{sh} = 4$, and $N_{sh} = 8$). Based on the analysis of these waveforms, it can be seen that there was a clear trend of increasing u_{mc} amplitude values as the fault deepened. The FFT spectrum for the same operating conditions and degrees of stator winding fault is shown in Figure 11b. Based on the analysis of the amplitudes of characteristic frequencies, it can be concluded that the largest increase in amplitude due to ITSCs was seen for the f_s component. An increase in other harmonics calculated according to Equation (4) can also be observed, especially the $f_s - f_r$, $f_s + f_r$, $f_s + 5f_s$, and $3f_s$ components.

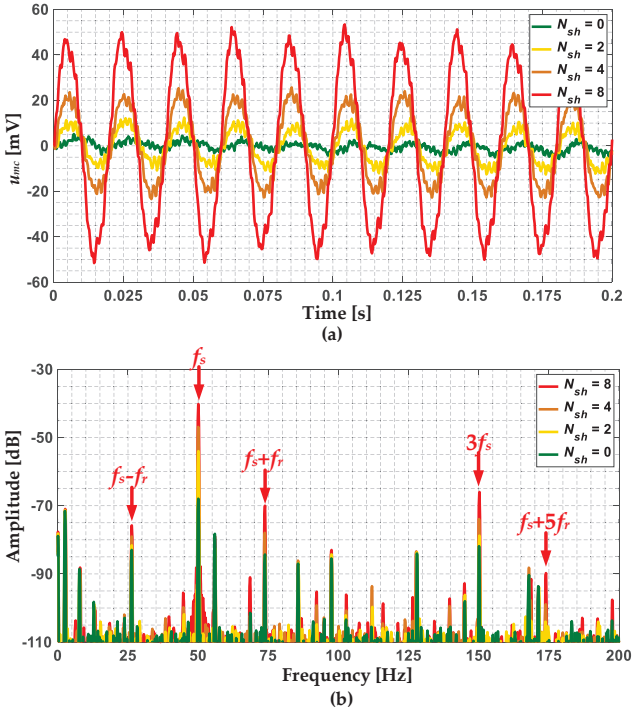

Figure 11. (**a**) The waveform and (**b**) the FFT spectrum of the u_{mc} measured using the NUCLEO-L476RG module, for a motor loaded with rated torque and different severities of the stator winding fault.

The effect of N_{sh} in the IM stator winding and the T_L level on the increase in the amplitudes of the characteristic fault frequencies (f_{ITSC}), $f_s - f_r$, $f_s + f_r$, $f_s + 5f_s$, and $3f_s$, in the FFT spectrum of the u_m, is shown in Figure 12. The increase in the value of the A_{diff} (f_{ITSC}) amplitudes is calculated as the difference between the amplitude value for the undamaged winding and a given number of shorted turns. Based on the analysis of the results shown in Figure 12, it can be concluded that the value of the amplitude of the f_s component increased significantly already with 1 shorted turn in the stator winding. In addition, only a very small effect of the load torque was visible. A similar trend was seen for the $f_s + f_r$ (Figure 12c) and $3f_s$ (Figure 12e) components. Nevertheless, the increases in the amplitudes of these components due to ITSCs were lower compared to the amplitudes of f_s. For the $f_s - f_r$, and $f_s + 5f_s$ frequency components, the increase in amplitudes due to the ITSC did not occur for the entire range of analyzed stator winding conditions and T_L levels. Thus, it can be concluded that monitoring the amplitude of the f_s and optionally

$f_s + f_r$ components can allow the detection of the IM stator winding fault at an early stage of its propagation (N_{sh} = 1).

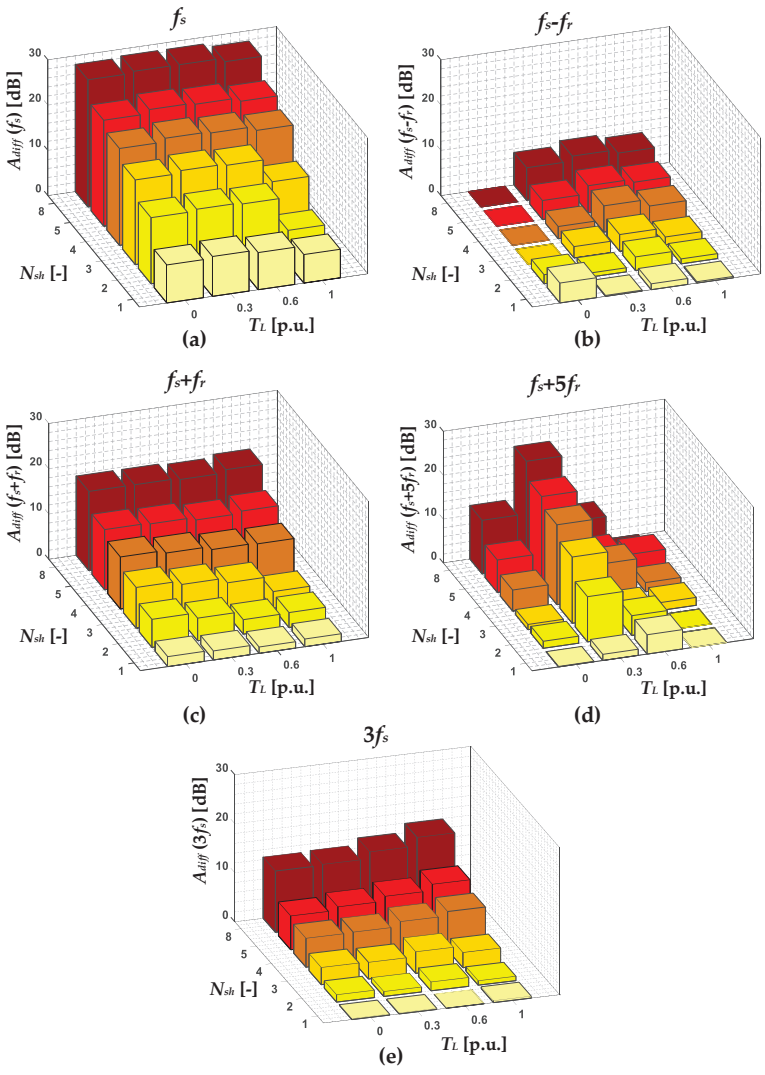

Figure 12. The effect of N_{sh} in the IM stator winding and T_L level on the increase in the amplitude of the selected frequency components: (**a**) f_s, (**b**) $f_s - f_r$, (**c**) $f_s + f_r$, (**d**) $f_s + 5f_r$ and (**e**) $3f_s$ in the FFT spectrum of the u_{mc}.

4.2. Unbalanced Supply Voltage

To introduce a condition of power supply voltage unbalance, each of the phases of the IM under study was supplied by a single-phase autotransformer allowing stepless voltage regulation. The supply voltage value in one of the phases (phase A) was reduced from 230 V to 210 V. The analyzed levels of the supply voltage unbalance are grouped in Table 3. The supply voltage unbalance coefficient, α_{u2}, was calculated as the ratio of the negative sequence supply voltage component to the positive sequence supply voltage component.

Table 3. Analyzed levels of the supply voltage unbalance.

The RMS Value of the Supply Voltage of the Phase C	Supply Voltage Unbalance Coefficient α_{u2}
230 V	0.08%
228 V	0.32%
225 V	0.57%
220 V	1.39%
215 V	2.23%
210 V	2.84%

The waveforms of the voltage induced in the measuring coil by the axial flux for different levels of power supply unbalance are shown in Figure 13. Based on the analysis of these waveforms it can be concluded that the effect of the power supply unbalance on the amplitude of the u_{mc} was significantly less visible compared to the effect of ITSCs. For the analyzed range of supply voltage unbalance levels, the u_{mc} amplitude was close to 5 mV.

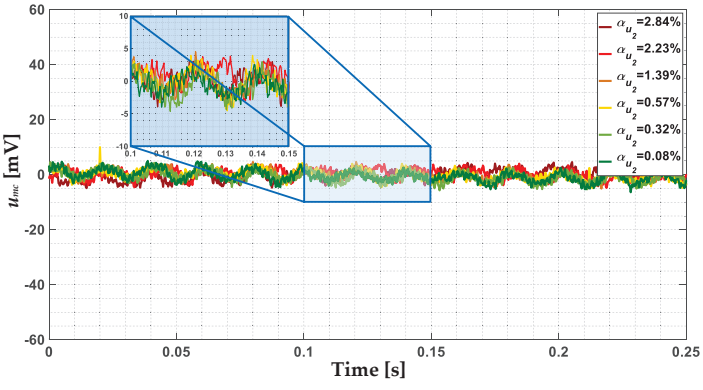

Figure 13. The waveforms of the voltage induced in the measuring coil by the axial flux for different levels of power supply unbalance.

The FFT spectrum of the u_{mc} measured using the NUCLEO-L476RG module for an unloaded motor (Figure 14a), a motor loaded with the rated load torque (Figure 14b), and different power supply unbalance levels is presented in Figure 14. Based on the analysis of these spectra, it can be concluded that there was an increase in the amplitude of the $f_s + 2f_r$ and $3f_s - 2f_r$ frequency components as a result of the supply voltage unbalance.

One of the most important observations is that the frequency components that increased as a result of the ITSC did not change their value due to the unbalanced supply voltage, and the other frequency components ($f_s + 2f_r$ and $3f_s - 2f_r$) appeared. This may allow the distinguishing between these two abnormal conditions (stator winding fault and unbalanced supply voltage). Nevertheless, a more detailed analysis is needed.

The effect of the supply voltage unbalance level and T_L on the increase in the amplitudes of the frequency components that increased the most significantly in the case of the ITSC (f_s and $f_s + f_r$), and the characteristics for supply voltage unbalance (according to Figure 14) ($f_s + 2f_r$, and $3f_s - 2f_r$) are presented in Figure 15. Based on the analysis of these results, it can be concluded that the values of the amplitude of the f_s and $f_s + f_r$ did not increase as a result of the unbalanced supply voltage. The amplitude increase of the $f_s + 2f_r$ component was visible already with an α_{u2} value of 1.39% (the phase voltage RMS value reduced to 220 V). In the case of the $3f_s - 2f_r$ frequency component, the increase as a result of the unbalanced supply voltage was more irregular for different levels of load torque but still visible. Thus, it can be concluded that monitoring the amplitude of the $f_s + 2f_r$, and

optionally $3f_s - 2f_r$ components can allow the detection of the unbalanced supply voltage of the IM drive.

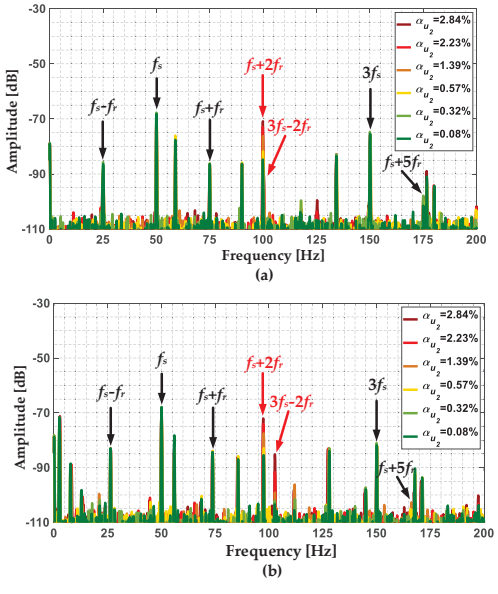

Figure 14. The FFT spectrum of the u_{mc} measured using the NUCLEO-L476RG module, for (**a**) an unloaded motor, and (**b**) a motor loaded with rated load torque, and different power supply unbalance levels.

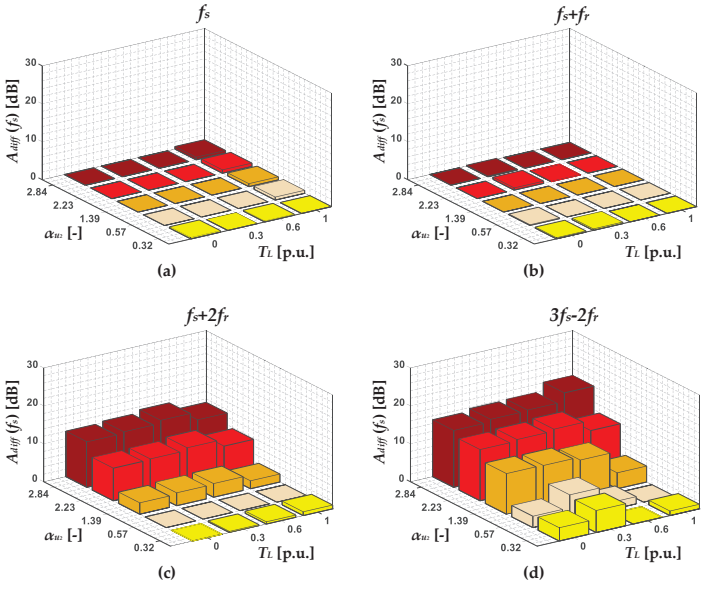

Figure 15. The effect of unbalanced supply voltage level and T_L on the increase in the amplitude of the selected frequency components: (**a**) f_s, (**b**) $f_s + f_r$, (**c**) $f_s + 2f_r$, and (**d**) $3f_s - 2f_r$ in the FFT spectrum of the u_{mc}.

4.3. Influence of the Power Supply Method on the Amplitude Increase of the Selected Harmonics

In the present work, special attention was paid to the IM powered directly from the grid. Nevertheless, the effectiveness of the ITSC symptom extraction was also verified for the IM powered by a Danfoss VLT AutomationDrive FC-302 inverter. The FFT spectra of the u_{mc} measured using the NUCLEO-L476RG module for a motor loaded with rated torque, the different severity of the stator winding fault, and the IM supplied by a Danfoss VLT AutomationDrive FC-302 inverter, for three different values of f_s, are shown in Figure 16. Based on the analysis of the results, it can be concluded that both in the case of the IM powered directly from the grid and a voltage source inverter, there was an increase in the amplitude value of the f_s component as a result of the ITSCs. It confirms the versatility of the proposed solution in terms of the power supply method.

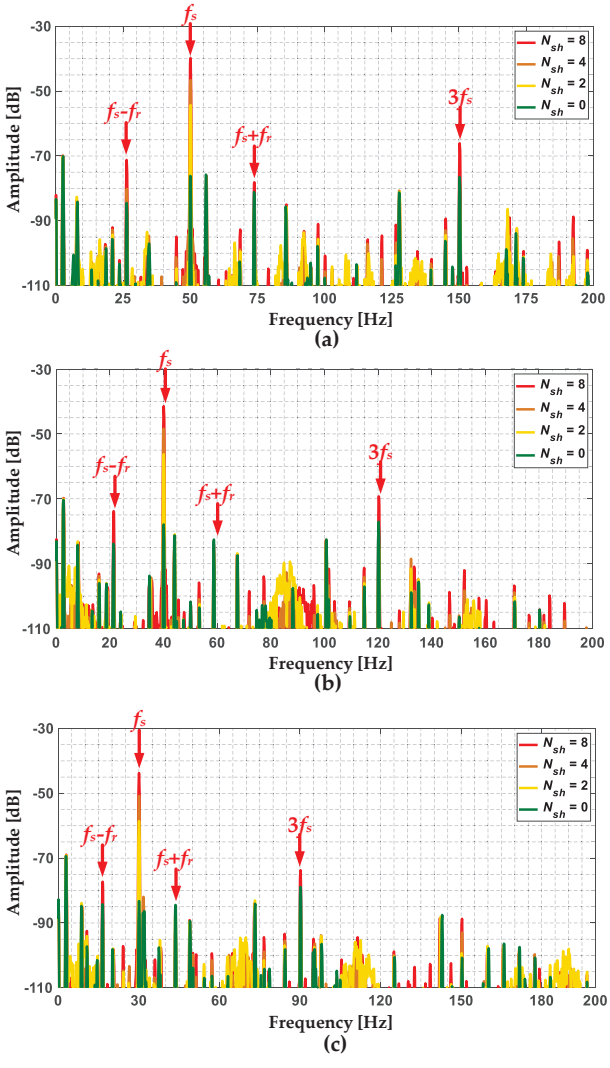

Figure 16. The FFT spectra of the u_{mc} measured using the NUCLEO-L476RG module for a motor loaded with rated torque, different degrees of stator winding fault, and power supply from voltage source inverter, (**a**) f_s = 50 Hz, (**b**) f_s = 40 Hz, and (**c**) f_s = 30 Hz.

4.4. Discussion of the Key Results and Plans for Future Research and Development

Experimental tests made it possible to evaluate the performance of the developed embedded system, analyze the effect of the IM stator winding fault and an unbalanced supply voltage on the voltage induced in the measurement coil by the axial flux, and extract the symptoms that appear in the FFT spectrum of this voltage as a result of these abnormal conditions. The key discoveries are as follows:

- The results of the measurement and signal acquisition process performed using the developed embedded system based on the STM32L476RG microcontroller did not differ from the results obtained using the high-end PXIe-4492 DAQ measurement card by NI;
- The ITSC in the IM stator winding resulted in a significant increase in the amplitude of the u_{mc} regardless of the level of the load torque. The greater the severity of the fault, the greater the increase in amplitude;
- The unbalanced supply voltage of the IM drive did not lead to an increase in the amplitude of the u_{mc};
- The value of the amplitude of the f_s component in the u_{mc} FFT spectrum increased the most as a result of the ITSC already with one shorted turn in the stator winding. The amplitudes of the $f_s + f_r$ and $3f_s$ components also increased, but the increase was smaller compared to f_s;
- The value of the amplitudes of the $f_s + 2f_r$ and $3f_s - 2f_r$ (particularly) components in the u_{mc} FFT spectrum increased the most due to the unbalanced supply voltage;
- The distinguishing between the two abnormal conditions analyzed (stator winding fault and unbalanced supply voltage) were recognized based on the monitoring of the amplitudes of the f_s (characteristic for stator winding fault) and the $3f_s - 2f_r$ (characteristic for unbalanced supply voltage) components;
- The developed method of monitoring the condition of the IM stator winding proved to be effective not only in the case of an IM supplied from the grid but also by the inverter.

Even though the developed system, despite its low cost, already at this stage allows monitoring of the condition of the IM stator winding and the symmetry of the supply voltage, it will be developed in the future and improved with important functions to meet the requirements for modern drive systems that are associated with the Industry 4.0 paradigm. There are many specific areas for future research and development (R&D), including:

- The improvement of the proposed system with the addition of a module that, based on the input vector consisting of statistical information about the voltage signal induced in the measuring coil by the axial flux and the values of harmonic amplitudes, will automatically indicate the state of the stator winding and the symmetry of the supply voltage;
- The integration of the amplifier and microcontroller on a single, specially designed compact PCB that can be mounted at the installer's convenience;
- An extension of the functionality of the developed system to measure other diagnostic signals, such as stator phase currents, and the ability to detect other types of faults, such as broken rotor cage bars, bearing faults, and others;
- An extension of the functionality of the developed system with other mathematical apparatuses that can be used for diagnostic signal processing to extract the symptoms of ITSC and unbalanced supply voltage, such as STFT;
- Adding the function of predicting the possibility of a given failure of the analyzed machine; an extension with the functionality called predictive maintenance;
- The analysis of application possibilities and industry areas where the developed system could be also applied.

From the above points, the first step will be to fully automate the process of monitoring IM stator winding conditions and supply voltage symmetry using AI (machine learning

and deep learning) techniques. A simplified block diagram of the flow of diagnostic information processing from the measurement of the signal on the monitored object to the automation of the process of inferring its condition (including the parts that have already been implemented and future R&D plans) is shown in Figure 17.

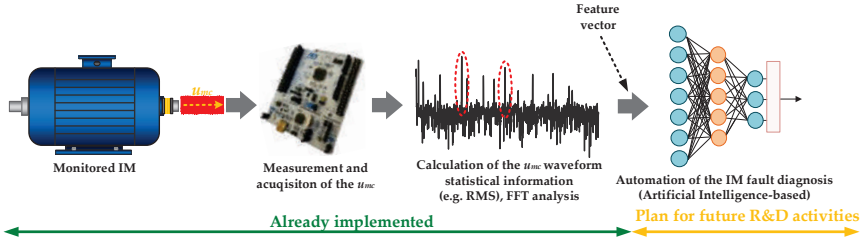

Figure 17. Simplified block diagram of the flow of diagnostic information including the parts that have already been implemented and future R&D plans.

5. Conclusions

The experimental results presented in this paper confirmed the feasibility of using a module based on a low-cost ARM Cortex-M4 core microcontroller to monitor the condition of the IM stator winding based on the voltage induced in the measuring coil by the axial flux. The experimental results also proved that FFT analysis of this signal made it possible to extract symptoms of an incipient ITSC, even with a single shorted turn in the stator winding of IM. The results also showed that it was possible to detect and distinguish from a short circuit an asymmetrical IM supply voltage based on analysis of the amplitudes of selected harmonics in the induced voltage spectrum. This study was carried out over a wide range of operating conditions of the drive system, including the verification of the effect of the power supply method on the increase of individual amplitudes in the analyzed spectrum of the voltage inducted by the axial flux.

The use of the proposed hardware implementation poses several challenges, including those related to the correct configuration of the measurement and acquisition of the diagnostic signal, which is explained in detail and can be helpful in the process of preparing an embedded system for diagnostic purposes for various types of applications. Since the evaluation board used in this work (NUCLEO-L476RG with low-cost STM32L476RG microcontroller) is much cheaper compared to the high-end data acquisition boards used, such as DAQ NI PXI-4492, it has great potential for industrial applications.

Future research will focus on the development and hardware implementation (on a low-cost microcontroller) of an algorithm that will fully automate the process of detecting and classifying an ITSC in the stator winding of an IM, which will use the statistical information of the induced voltage waveform or the amplitude of selected harmonics in the FFT spectrum of this signal. For this purpose, it is planned to use machine learning algorithms whose computational complexity will allow implementation in an embedded system.

Author Contributions: All of the authors contributed equally to the concept of the paper, and proposed the methodology; investigation and formal analyses, P.P. (Przemyslaw Pietrzak), P.P. (Piotr Pietrzak) and M.W.; software and data curation, P.P. (Przemyslaw Pietrzak) and P.P. (Piotr Pietrzak); measurements, P.P. (Przemyslaw Pietrzak), P.P. (Piotr Pietrzak) and M.W.; proposed the paper organization, P.P. (Przemyslaw Pietrzak) and M.W.; validated the obtained results, M.W. All authors have read and agreed to the published version of the manuscript.

Funding: This research received no external funding.

Data Availability Statement: Data are contained within the article.

Conflicts of Interest: The authors declare no conflict of interest.

References

1. Laadjal, K.; Amaral, A.M.R.; Sahraoui, M.; Cardoso, A.J.M. Machine Learning Based Method for Impedance Estimation and Unbalance Supply Voltage Detection in Induction Motors. *Sensors* **2023**, *23*, 7989. [CrossRef] [PubMed]
2. Aguayo-Tapia, S.; Avalos-Almazan, G.; Rangel-Magdaleno, J.D.J.; Ramirez-Cortes, J.M. Physical Variable Measurement Techniques for Fault Detection in Electric Motors. *Energies* **2023**, *16*, 4780. [CrossRef]
3. He, J.; Somogyi, C.; Strandt, A.; Demerdash, N.A.O. Diagnosis of Stator Winding Short-Circuit Faults in an Interior Permanent Magnet Synchronous Machine. In Proceedings of the 2014 IEEE Energy Conversion Congress and Exposition (ECCE), Pittsburg, PA, USA, 15–18 September 2014; pp. 3125–3130.
4. Baruti, K.H.; Li, C.; Erturk, F.; Akin, B. Online Stator Inter-Turn Short Circuit Estimation and Fault Management in Permanent Magnet Motors. *IEEE Trans. Energy Convers.* **2023**, *38*, 1016–1027. [CrossRef]
5. Gonzalez-Cordoba, J.L.; Osornio-Rios, R.A.; Granados-Lieberman, D.; Romero-Troncoso, R.D.J.; Valtierra-Rodriguez, M. Thermal-Impact-Based Protection of Induction Motors Under Voltage Unbalance Conditions. *IEEE Trans. Energy Convers.* **2018**, *33*, 1748–1756. [CrossRef]
6. Lashkari, N.; Poshtan, J.; Azgomi, H.F. Simulative and Experimental Investigation on Stator Winding Turn and Unbalanced Supply Voltage Fault Diagnosis in Induction Motors Using Artificial Neural Networks. *ISA Trans.* **2015**, *59*, 334–342. [CrossRef] [PubMed]
7. Siddique, A.; Yadava, G.S.; Singh, B. A Review of Stator Fault Monitoring Techniques of Induction Motors. *IEEE Trans. Energy Convers.* **2005**, *20*, 106–114. [CrossRef]
8. Niu, G.; Dong, X.; Chen, Y. Motor Fault Diagnostics Based on Current Signatures: A Review. *IEEE Trans. Instrum. Meas.* **2023**, *72*, 1–19. [CrossRef]
9. Riera-Guasp, M.; Antonino-Daviu, J.A.; Capolino, G.-A. Advances in Electrical Machine, Power Electronic, and Drive Condition Monitoring and Fault Detection: State of the Art. *IEEE Trans. Ind. Electron.* **2015**, *62*, 1746–1759. [CrossRef]
10. Garcia-Calva, T.; Morinigo-Sotelo, D.; Fernandez-Cavero, V.; Romero-Troncoso, R. Early Detection of Faults in Induction Motors—A Review. *Energies* **2022**, *15*, 7855. [CrossRef]
11. Gultekin, M.A.; Bazzi, A. Review of Fault Detection and Diagnosis Techniques for AC Motor Drives. *Energies* **2023**, *16*, 5602. [CrossRef]
12. Alloui, A.; Laadjal, K.; Sahraoui, M.; Marques Cardoso, A.J. Online Interturn Short-Circuit Fault Diagnosis in Induction Motors Operating under Unbalanced Supply Voltage and Load Variations, Using the STLSP Technique. *IEEE Trans. Ind. Electron.* **2023**, *70*, 3080–3089. [CrossRef]
13. Cruz, S.M.A.; Cardoso, A.J.M. Stator Winding Fault Diagnosis in Three-Phase Synchronous and Asynchronous Motors, by the Extended Park's Vector Approach. *IEEE Trans. Ind. Appl.* **2001**, *37*, 1227–1233. [CrossRef]
14. Piechocki, M.; Pajchrowski, T.; Kraft, M.; Wolkiewicz, M.; Ewert, P. Unraveling Induction Motor State through Thermal Imaging and Edge Processing: A Step towards Explainable Fault Diagnosis. *Eksploat. Niezawodn. Maint. Reliab.* **2023**, *25*. [CrossRef]
15. Drif, M.; Cardoso, A.J.M. Stator Fault Diagnostics in Squirrel Cage Three-Phase Induction Motor Drives Using the Instantaneous Active and Reactive Power Signature Analyses. *IEEE Trans. Ind. Inf.* **2014**, *10*, 1348–1360. [CrossRef]
16. Kumar, T.C.A.; Singh, G.; Naikan, V.N.A. Sensitivity of Rotor Slot Harmonics Due to Inter-Turn Fault in Induction Motors through Vibration Analysis. In Proceedings of the 2018 International Conference on Power, Instrumentation, Control and Computing (PICC), Thrissur, India, 18–20 January 2018; pp. 1–3.
17. Skowron, M.; Wolkiewicz, M.; Orlowska-Kowalska, T.; Kowalski, C.T. Effectiveness of Selected Neural Network Structures Based on Axial Flux Analysis in Stator and Rotor Winding Incipient Fault Detection of Inverter-Fed Induction Motors. *Energies* **2019**, *12*, 2392. [CrossRef]
18. Pietrzak, P.; Wolkiewicz, M. Fault Diagnosis of PMSM Stator Winding Based on Continuous Wavelet Transform Analysis of Stator Phase Current Signal and Selected Artificial Intelligence Techniques. *Electronics* **2023**, *12*, 1543. [CrossRef]
19. Orlowska-Kowalska, T.; Wolkiewicz, M.; Pietrzak, P.; Skowron, M.; Ewert, P.; Tarchala, G.; Krzysztofiak, M.; Kowalski, C.T. Fault Diagnosis and Fault-Tolerant Control of PMSM Drives–State of the Art and Future Challenges. *IEEE Access* **2022**, *10*, 59979–60024. [CrossRef]
20. Al-Andoli, M.N.; Tan, S.C.; Sim, K.S.; Seera, M.; Lim, C.P. A Parallel Ensemble Learning Model for Fault Detection and Diagnosis of Industrial Machinery. *IEEE Access* **2023**, *11*, 39866–39878. [CrossRef]
21. Ma, J.; Liu, X.; Hu, J.; Fei, J.; Zhao, G.; Zhu, Z. Stator ITSC Fault Diagnosis of EMU Asynchronous Traction Motor Based on ApFFT Time-Shift Phase Difference Spectrum Correction and SVM. *Energies* **2023**, *16*, 5612. [CrossRef]
22. Das, A.K.; Das, S.; Pradhan, A.K.; Chatterjee, B.; Dalai, S. RPCNNet: A Deep Learning Approach to Sense Minor Stator Winding Interturn Fault Severity in Induction Motor under Variable Load Condition. *IEEE Sens. J.* **2023**, *23*, 3965–3972. [CrossRef]
23. Zhou, Y.; Shang, Q.; Guan, C. Three-Phase Asynchronous Motor Fault Diagnosis Using Attention Mechanism and Hybrid CNN-MLP By Multi-Sensor Information. *IEEE Access* **2023**, *11*, 98402–98414. [CrossRef]
24. Guo, J.; Wan, J.-L.; Yang, Y.; Dai, L.; Tang, A.; Huang, B.; Zhang, F.; Li, H. A Deep Feature Learning Method for Remaining Useful Life Prediction of Drilling Pumps. *Energy* **2023**, *282*, 128442. [CrossRef]
25. Sawitri, D.R.; Asfani, D.A.; Purnomo, M.H.; Purnama, I.K.E.; Ashari, M. Early Detection of Unbalance Voltage in Three Phase Induction Motor Based on SVM. In Proceedings of the 2013 9th IEEE International Symposium on Diagnostics for Electric Machines, Power Electronics and Drives (SDEMPED), Valencia, Spain, 27–30 August 2013; pp. 573–578.

26. Refaat, S.S.; Abu-Rub, H.; Saad, M.S.; Aboul-Zahab, E.M.; Iqbal, A. Detection, Diagnoses and Discrimination of Stator Turn to Turn Fault and Unbalanced Supply Voltage Fault for Three Phase Induction Motors. In Proceedings of the 2012 IEEE International Conference on Power and Energy (PECon), Kota Kinabalu, Malaysia, 2–5 December 2012; pp. 910–915.
27. Çakır, A.; Çalış, H.; Küçüksille, E.U. Data Mining Approach for Supply Unbalance Detection in Induction Motor. *Expert Syst. Appl.* **2009**, *36*, 11808–11813. [CrossRef]
28. Laadjal, K.; Sahraoui, M.; Alloui, A.; Cardoso, A.J.M. Three-Phase Induction Motors Online Protection against Unbalanced Supply Voltages. *Machines* **2021**, *9*, 203. [CrossRef]
29. Vassiliev, A.E.; Ivanova, T.Y.; Cabezas Tapia, D.F.; Luong, Q.T. Microcontroller-Based Embedded System Equipment Development for Research and Educational Support. In Proceedings of the 2016 International Conference on Information Management and Technology (ICIMTech), Bandung, Malaysia, 16–18 November 2016; pp. 219–223.
30. Zachary Lasiuk, P.V.J.A. *The Insider's Guide to Arm Cortex-M Development. Leverage Embedded Software Development Tools and Examples to Become an Efficient Cortex-M Developer*; Packt Publishing: Burmingham, UK, 2022.
31. Saha, S.; Tyagi, T.; Gadre, D.V. ARM(R) Microcontroller Based Automatic Power Factor Monitoring and Control System. In Proceedings of the 2013 Texas Instruments India Educators' Conference, Bangalore, India, 4–6 April 2013; pp. 165–170.
32. Waswani, R.; Pawar, A.; Deore, M.; Patel, R. Induction Motor Fault Detection, Protection and Speed Control Using Arduino. In Proceedings of the 2017 International Conference on Innovations in Information, Embedded and Communication Systems (ICIIECS), Coimbatore, India, 17–18 March 2017; pp. 1–5.
33. Sutar, P.P.; Panchade, V.M. Induction Motor Faults Mitigation Using Microcontroller. In Proceedings of the 2017 International Conference on Energy, Communication, Data Analytics and Soft Computing (ICECDS), Chennai, India, 1–2 August 2017; pp. 489–493.
34. Gargiulo, F.; Liccardo, A.; Schiano Lo Moriello, R. A Non-Invasive Method Based on AI and Current Measurements for the Detection of Faults in Three-Phase Motors. *Energies* **2022**, *15*, 4407. [CrossRef]
35. STM32 Nucleo-64 Development Board with STM32L476RG MCU Product Overview. Available online: https://www.st.com/en/evaluation-tools/nucleo-l476rg.html (accessed on 10 December 2023).
36. Reference Manual RM0351: STM32L47xxx, STM32L48xxx, STM32L49xxx and STM32L4Axxx Advanced Arm®-Based 32-Bit MCUs. Available online: https://www.st.com/resource/en/reference_manual/rm0351-stm32l47xxx-stm32l48xxx-stm32l49xxx-and-stm32l4axxx-advanced-armbased-32bit-mcus-stmicroelectronics.pdf (accessed on 10 December 2023).
37. Skowron, M. Application of Deep Learning Neural Networks for the Diagnosis of Electrical Damage to the Induction Motor Using the Axial Flux. *Bull. Pol. Acad. Sci. Tech. Sci.* **2020**, *68*, 1031–1038. [CrossRef]

MDPI
St. Alban-Anlage 66
4052 Basel
Switzerland
www.mdpi.com

Energies Editorial Office
E-mail: energies@mdpi.com
www.mdpi.com/journal/energies

Academic Open
Access Publishing

mdpi.com

ISBN 978-3-7258-1340-7